

VILNIUS UNIVERSITY  
CENTER FOR PHYSICAL SCIENCES AND TECHNOLOGY

Joel Edith Flora

# Investigation of Chitosan-Graphene Oxide Nanocomposites and their Application in Environmental Protection

**DOCTORAL DISSERTATION**

Natural Sciences,  
Chemistry (N 003)

VILNIUS 2024

The dissertation was prepared between 2019 and 2023 at the State Research Institute Centre for Physical Sciences and Technology.

**Academic supervisor – Dr Galina Lujanienė** (SRI Centre for Physical Sciences and Technology, Natural sciences, Chemistry – N 003).

This doctoral dissertation will be defended in a public meeting of the Dissertation Defence Panel:

**Chairman – Dr. Evaldas Maceika** (SRI Centre for Physical Sciences and Technology, Natural Sciences, Physics – N 002).

**Members:**

**Dr. Reda Dzingelevičienė** (Klaipeda University, Natural Sciences, Chemistry – N 003);

**Dr. Arūnas Gudelis** (SRI Centre for Physical Sciences and Technology, Natural Sciences, Physics – N 002);

**Dr. Jixin Qiao** (Danish Technical University, Natural Sciences, Chemistry – N 003);

**Dr. Danguolė Montvydienė** (Nature Research Centre, Natural Sciences, Ecology and Environmental Sciences – N 012).

The dissertation shall be defended at a public meeting of the Dissertation Defence Panel at 1:00 P.M. on 1st October 2024 in meeting room D401 of the SRI Centre for Physical Sciences and Technology.

Address: Sauletekio av. 3, D401, Vilnius, Lithuania.

Tel. +37052649211; e-mail: [office@ftmc.lt](mailto:office@ftmc.lt)

The text of this dissertation can be accessed at the libraries of the SRI Centre for Physical Sciences and Technology and Vilnius University, as well as on the website of Vilnius University: [www.vu.lt/lt/naujienos/ivykiu-kalendorius](http://www.vu.lt/lt/naujienos/ivykiu-kalendorius)

VILNIAUS UNIVERSITETAS  
FIZINIŲ IR TECHNOLOGIJOS MOKSLŲ CENTRAS

Joel Edith Flora

# Chitozano-grafeno oksido nanokompozitų tyrimai ir jų taikymai aplinkosaugoje

**DAKTARO DISERTACIJA**

Gamtos mokslai,  
Chemija (N 003)

VILNIUS 2024

Disertacija rengta 2019–2023 metais Fizinių ir technologijos mokslų centre.

**Mokslinė vadovė – dr. Galina Lujanienė** (VMTI Fizinių ir technologijos mokslų centras, gamtos mokslai, chemija, N 003).

Gynimo taryba:

**Pirmininkas – dr. Evaldas Maceika** (VMTI Fizinių ir technologijos mokslų centras, gamtos mokslai, fizika, N 002).

**Nariai:**

**dr. Reda Dzingelevičienė** (Klaipėdos universitetas, gamtos mokslai, chemija. N 003);

**dr. Danguolė Montvydienė** (Gamtos tyrimų centras, gamtos mokslai, ekologija ir aplinkotyra . N 012);

**dr. Jixin Qiao** (Danijos technikos universitetas, gamtos mokslai, chemija, N 003);

**dr. Arūnas Gudelis** (VMTI Fizinių ir technologijos mokslų centras, gamtos mokslai fizika, N 002).

Disertacija ginama viešame Gynimo tarybos posėdyje 2023 m. spalio mėn. 1 d. 13 val. VMTI Fizinių ir technologijos mokslų centro D401 auditorijoje.

Adresas: Adresas: Saulėtekio al. 3, D401, Vilnius, Lietuva.

Tel. +37052649211; el. paštas [office@ftmc.lt](mailto:office@ftmc.lt)

Disertaciją galima peržiūrėti Fizinių ir technologijos mokslų centro bei Vilniaus universiteto bibliotekose ir VU interneto svetainėje adresu:  
[www.vu.lt/lt/naujienos/ivykiu-kalendorius](http://www.vu.lt/lt/naujienos/ivykiu-kalendorius)

## CONTENTS

INTRODUCTION.....	9
1. LITERATURE REVIEW.....	17
1.1. Food Packaging .....	17
1.1.1. Polymers in food packaging.....	17
1.1.2. Chitosan-graphene oxide nanocomposites in food packaging ...	19
1.1.3. Copper and platinum nanoparticles in Food Packaging.....	22
1.1.4. Migration of nanoparticles to food.....	25
1.2. Nanocomposite for the removal of radionuclides.....	27
1.2.1. Maghemite.....	27
1.2.2. Graphene oxide as an adsorbent.....	28
1.2.3. Chitosan as an adsorbent .....	30
1.2.4. Adaptive neuro-fuzzy inference system .....	31
2. MATERIALS AND METHODS.....	33
2.1. Synthesis of materials for food Packaging .....	33
2.1.1. Preparation of graphene oxide-chitosan-platinum-copper oxides/copper composites and thin film .....	33
2.1.2. Characterization.....	35
2.1.3. UV Visible spectroscopy.....	36
2.1.4. Antimicrobial activity of nanocomposites and thin films .....	36
2.1.5. Degree of Swelling and Moisture content.....	37
2.1.6. Hydrophilicity of Film Surface .....	38
2.1.7. Degradation of Graphene Oxide-Chitosan-Platinum-Copper Oxides/Copper thin films .....	38
2.1.8. Migration of Copper from Graphene Oxide-Chitosan-Platinum- Copper Oxides/Copper thin films.....	39
2.2. Synthesis of Magnetic-Nano Adsorbent.....	39

2.2.1. Preparation of Graphene Oxide-Maghemit Nanoparticles and Graphene Oxide-Maghemit-Chitosan composite .....	39
2.2.2. Characterisation.....	42
2.2.3. Batch Experiments .....	42
2.2.4. Determination of the Point of Zero Charge.....	43
2.2.5. Elimination of Europium, Americium, and Plutonium Ions from Aquatic Environments.....	43
2.2.6. ANFIS development.....	44
<b>3. RESULTS AND DISCUSSION .....</b>	<b>52</b>
3.1. Characterization of composites for food packaging .....	52
3.1.1. XRD.....	52
3.1.2 FTIR .....	53
3.1.3. Ultraviolet shielding efficiency of nanocomposite films .....	55
3.1.4. Antibacterial Study.....	57
3.1.5. Hydrodynamic Properties.....	58
3.1.6. Biodegradability .....	61
3.1.7. Surface Characterisation.....	63
3.1.8. AFM and FE-SEM .....	65
3.1.9. Migration of Copper.....	66
3.2. Characterisation of composites for adsorption studies .....	69
3.2.1. XRD.....	69
3.2.2. Möessbauer Spectroscopy .....	69
3.2.3. FTIR .....	73
3.2.4. Raman Spectroscopy .....	75
3.2.5. TEM.....	76
3.2.6. Adsorption Studies .....	76
3.2.7. Kinetic Studies .....	80
3.2.8 Adsorption Mechanism .....	82
3.2.9. Removal of Eu(III), Pu(IV), and Am(III) from Natural Waters	84
3.2.10. ANFIS .....	85

CONCLUSIONS .....	89
SANTRAUKA.....	90
CURRICULUM VITAE .....	139

## ABBREVIATIONS

ANFIS - Adaptive neuro-fuzzy inference system  
AFM - Atomic Force Microscopy  
ATR - Attenuated Total Reflectance  
CS - Chitosan  
MNP - Metallic nanoparticles  
EDX - Energy Dispersive X-ray Analysis  
GO - Graphene oxide  
NP - Nano Particle  
FE-SEM - Field Emission- scanning electron microscope  
TEM - transmission electron microscope  
XRD - X-ray diffraction  
GO-CS - Graphene Oxide-Chitosan  
GO-CS-Pt - Graphene Oxide-Chitosan-Platinum  
GO-CS-Pt-Cu - Graphene Oxide-Chitosan-Platinum- Copper  
GO-CS-Pt-CuO - Graphene Oxide-Chitosan-Platinum- Copper (II)  
Oxide  
GO-CS-Pt-Cu<sub>2</sub>O - Graphene Oxide-Chitosan-Platinum- Copper(I)  
Oxide  
GO-CS-Pt-Cu<sub>2</sub>O/Cu - Graphene Oxide-Chitosan-Platinum-  
Copper(I)Oxide/Copper  
MGH - Maghemite Nanoparticles  
GO-MGH - Graphene Oxide-Maghemit  
GO-MGH-CS - Graphene Oxide-Maghemit-Chitosan  
WCA - Water Contact Angle  
MVTR - Moisture Vapour Transmission Rate  
WS - Water solubility

## INTRODUCTION

The advent of plastics in the early 20th century has brought about significant transformations in numerous industries owing to their multifaceted characteristics and economic viability. The widespread presence of these plastic entities across various industries, ranging from packaging to healthcare, highlights their significance in present-day societies (Andrade & Neal, 2009). Despite its potential benefits, the widespread adoption of plastics recycling is hindered by several hurdles, including technological barriers and market factors. Identifying and resolving these difficulties offers opportunities to improve the sustainability of plastic use and mitigate its negative environmental impacts (Hopewell et al., 2009). The manufacturing process of plastics requires a substantial amount of energy, resulting in a notable contribution to overall carbon emissions worldwide. This further amplifies concerns regarding climate change (Cabernard et al., 2022; Geyer et al., 2017). Chitosan is a biopolymer that is generally obtained from the shells of crustaceans, such as shrimp and crabs, and occasionally from certain fungi. This substance is a deacetylated derivative of chitin, a naturally occurring polysaccharide, second only to cellulose. Biodegradable materials have attracted attention owing to their wide range of applications in various industries, particularly biomedicine and food packaging (Rinaudo, 2006).

The discovery and characterization of graphene is a remarkable achievement in the field of nanomaterials (Novoselov et al., 2004). Graphene consists of a single layer of carbon atoms arranged in a two-dimensional lattice structure. Graphene oxide (GO) has oxygen-containing functional groups in its oxidized state, which facilitates its dispersion in a range of solvents and increases its potential for subsequent functionalization. Due to its inherent atomic structure, graphene possesses outstanding mechanical properties that distinguish it from other currently known materials (Y. Zhu et al., 2010). It exhibits incredible strength and flexibility at the same time. Furthermore, the chemical adaptability of graphene, i.e., graphene oxide, offers numerous opportunities to incorporate additional molecules (Dreyer et al., 2009), thus expanding its range of applications and tailoring its properties to specific applications. The adaptability underlines the promise of graphene oxide not only as a stand-alone material, but also as a fundamental component for composite materials that exhibit improved properties.

Food packaging: Films made of chitosan (CS) are naturally biodegradable. This property is a response to concerns about the persistence of synthetic plastic packaging materials in the environment (S. Kumar et al., 2020). A notable property of GO that is relevant to the food industry is its exceptional ability to act as a barrier against gasses. This property is of great importance as it can effectively prevent the penetration of oxygen into food packaging, thus prolonging the period during which the food is fit for consumption (X. Huang et al., 2012). GO and CS are combined to produce GO-CS composites. These GO-CS composites are used in food packaging solutions where they shield moisture and gasses. This makes them ideal for food packaging where oxygen ingress and exposure to moisture can affect shelf life (Cabrini et al., 2023; Han Lyn et al., 2019).

Metallic nanoparticles (MNPs) have gained attention in the field of nanotechnology and have attracted the interest of researchers and companies due to their unique properties at the nanoscale (Ganachari et al., 2019). When incorporated into biopolymers such as chitosan, MNPs can significantly improve the properties of the material and can be used in food packaging and coating technologies (Adeyemi & Fawole, 2023). The physicochemical properties of these structures are primarily based on the presence of highly unrestricted surface electrons. As a result, they exhibit special properties, including high surface energy, efficient plasmon excitation and a wide range of intriguing optical properties (Dobrucka & Ankiel, 2019; Kolwas & Derkachova, 2020). In particular, the use of MNPs has enabled the improvement of various properties of food packaging, including mechanical properties, water vapour permeability and antibacterial efficacy (Cano-Sarmiento et al., 2015; dos Santos et al., 2020). This has made it possible to preserve product freshness, extend shelf life and develop safer and more environmentally friendly food packaging solutions. Gold (Au), silver (Ag), titanium dioxide (TiO<sub>2</sub>), zinc oxide (ZnO), copper (Cu), copper oxide (CuO) has been investigated for potential applications in food packaging (Devlieghere et al., 2004; Fernández et al., 2010; R. Hosseini et al., 2017; Mohan et al., 2019; Oun & Rhim, 2017; Pissuwan et al., 2020; Zimoch-Korzycka & Jarmoluk, 2015). The inclusion of metal nanoparticles as fillers in the GO-CS nanocomposite matrix can thus improve antimicrobial properties, water resistance, tensile strength and thermal stability (Apperrot et al., 2009; Dhillon et al., 2014; Kanted et al., 2023; Terzioglu et al., 2020). Copper nanoparticles are known for their antimicrobial activity, thermal conductivity, barrier reinforcement and improved mechanical properties (Grass et al., 2011).

Metallic nanoparticles or ions from packaging can migrate into food or food simulants, which can affect food quality and health. Due to their high surface-to-volume ratio, metal nanoparticles in chitosan can release ions to food simulants (Yang et al., 2019). Understanding migration rates and quantities is critical for compliance with regulatory restrictions for food safety (Bott et al., 2014). Factors influencing migration include the stability of the metal-chitosan bond, the type of food simulant, temperature, pH, and contact time. Studies have shown varying migration rates for different nanoparticles in chitosan films, with factors like pH and contact time influencing the release of nanosilver particles from antimicrobial containers (Bumbudsanpharoke et al., 2019; Echegoyen & Nerín, 2013).

While there is already work on the importance of GO-CS food packaging using silver and zinc oxide as fillers, the potential of using copper (I) oxide/copper nanoparticle or biphasic copper nanoparticles as fillers in the GO-CS matrix has been less explored. The aim of this work is to provide information on the synthesis and characterization of copper (I) oxide/copper nanoparticles and their potential applications as fillers in the food packaging industry, considering factors such as biodegradability and migration of metal ions into food.

**Adsorbents:** In the current phase of nuclear energy expansion and also in the foreseeable future, uranium is and will remain an important primary resource for the generation of reliable electricity with a minimal carbon footprint, especially for base load electricity demand (Kurniawan et al., 2022). The hazardous properties of uranium, including its radioactivity, toxicity to living organisms and long half-life, pose a significant threat to the environment when contaminated wastewater is directly discharged. The long-term environmental impacts of human activities associated with uranium mining and processing, as well as routine discharges from nuclear power plants and accidental releases of contaminated water (such as the events in Pennsylvania in 1979, Chernobyl in 1986 and Fukushima Daiichi in 2011), pose a significant threat to both human populations and organisms (Hirose, 2016; Lv et al., 2021). Over the past decade, extensive studies have been conducted on remediation using a wide range of techniques, including ion exchange, filtration, solvent extraction, reductive precipitation, and adsorption (Foster et al., 2020; Mahmoud et al., 2017; Tang et al., 2020; G. Wu et al., 2020; Xie et al., 2019).

Maghemite is classified as a variant of iron oxide nanoparticles that exhibits inherent magnetic properties. The magnetic properties of maghemite are very advantageous as they facilitate the separation of the adsorbent from the aqueous medium after the adsorption process. After adsorption, the radionuclides can be conveniently separated using an external magnetic field, streamlining the purification process. Moreover, the considerable surface area of the material provides ample space for the adsorption of radionuclides (Afkhami & Norooz-Asl, 2009; Etale et al., 2016). The oxygen-containing functional groups on GO enabled it to bind successfully with various metal ions and radionuclides. The substantial surface area and considerable adsorption capacity of this material make it a compelling option for the removal of radionuclides. In addition, graphene oxide (GO) can form stable dispersions in water, facilitating its interaction with aqueous pollutants (Z.-W. Huang et al., 2019a; Y. Sun et al., 2012).

Chitosan can form chelates with metal ions and radionuclides due to the presence of amino groups. Chitosan exhibits favourable properties in terms of its biocompatibility and biodegradability, making it a promising adsorbent with environmentally beneficial characteristics. The material exhibits enhanced cationic properties in acidic environments, resulting in an increased capacity to adsorb species with negative charges (S. Liu et al., 2021; Lujanienė et al., 2024). In combination, these composites can improve the adsorption capacities of radionuclides (Pujol Pozo et al., 2022).

Machine learning is currently used extensively in adsorption studies. It enables the prediction of adsorption capacity or adsorbent efficiency as a function of various parameters (pH, contact time, initial concentration, etc.), which in turn is important for experimental design, time saving and reagent use (Amiri et al., 2013; Onu et al., 2021a). Prevailing modelling techniques include the response surface approach, artificial neural network, neural general regression network, and adaptive neuro-fuzzy inference system. Among these, ANFIS has shown superior predictive capabilities (Dolatabadi et al., 2018). Adaptive Neuro-Fuzzy Inference System (ANFIS) is a hybrid computational model that combines artificial neural network techniques with fuzzy logic methods. The Adaptive Neuro-Fuzzy Inference System (ANFIS) is an effective method for modelling and analysing complicated systems that exhibit nonlinear behaviour, such as the interaction between adsorbents and adsorbates. ANFIS works as a multi-level network that sets up a collection of fuzzy if-then rules and generates given input-output pairings.

However, no work was found on the application of ANFIS for MGH, GO-MGH, GO-MGH-CS I, GO-MGH-CS II, and GO-MGH-CS III to the adsorption of europium, indicating a potential knowledge gap and a promising area for future investigation.

## THE MAIN AIM AND TASK

The aim of this study was to provide a conceptual framework for the development of environmentally friendly composites and thin films with adjustable biodegradability that could serve to protect water systems and are capable of reducing the environmental burden of toxic waste by replacing plastics with non-toxic natural materials. Contaminants can be extracted and used in closed production processes.

In order to achieve the objectives of the study, the following tasks were formulated:

1. The synthesis of nanoparticles, composites and films and their characterization.
2. Investigation of the mechanism of adsorption of Eu on GO-MGH-CS composites in batch experiments and comparison of the adsorption of Eu with Am and Pu in natural waters.
3. Application of the ANFIS model to predict the adsorption capacity of GO-MGH-CS composites for Eu<sup>+3</sup>.
4. Investigation of the antibacterial effect of GO-CS-Pt/copper/copper oxide composite films intended for use in food packaging on *Escherichia coli*.
5. Investigation of the properties of GO-CS-Pt/copper/copper oxide composite films in terms of UV radiation blocking, hydrophilicity, degree of swelling and solubility.
6. Investigation of the biodegradation of GO-CS-Pt copper/copper oxide composite films in soil and the migration rate of copper by double contact techniques in food simulants.

## NOVELTY

As far as is currently known, thin GO-CS-Pt-Cu<sub>2</sub>O/Cu composite films were synthesized for the first time and used in antimicrobial studies against *E. coli*. In addition, the biodegradability of GO-CS-Pt-copper oxide /copper in soil and the migration rate of copper by the double contact method in food simulants after 10 days were investigated for the first time.

To the best of our knowledge, MGH, GO-MGH, GO-MGH-CS I, GO-MGH-CS II, GO-MGH-CS III were not used for the adsorption of europium as well as for the removal of Eu(III), Pu(IV) and Am(III) from natural waters. In addition, the ANFIS model was applied for the first time to the MGH-Eu(III), GO-MGH-Eu(III), GO-MGH-CS I -Eu(III), GO-MGH-CS II -Eu(III) and GO-MGH-CS III -Eu(III) systems.

## DEFENSE STATEMENTS

1. GO-CS-Pt-Cu<sub>2</sub>O/Cu nanocomposites incorporated into the chitosan matrix (membrane) showed enhanced antibacterial activity against *E. coli.*; while maintaining a lower migration rate of copper ions in simulated food environments.
2. The mechanical properties and biodegradability of the GO-CS-Pt-Cu<sub>2</sub>O/Cu nanocomposite membranes are tunable depending on the concentration of Cu<sub>2</sub>O/Cu nanoparticles making them suitable for various packaging applications.
3. The GO-MGH-CS composite films showed excellent capacity for Eu(III) adsorption in batch studies. The removal efficiency of Eu(III) from water samples of different origins ranged from 74 % to 100 %.
4. The ANFIS model shows robust performance and generalization ability, which enables accurate prediction of the capacity of the GO-MGH-CS composite films for the adsorption of Eu.

## CONTRIBUTION OF THE AUTHOR

The author of the work synthesized composites, planned and conducted experiments. Participated in the analysis and interpretation of the results, designed graphical illustrations, wrote manuscripts, and presented the results at scientific conferences.

## LIST OF PUBLICATIONS

1. **Joel E.F.**, Lujaniene G., (2022) Progress in Graphene Oxide Hybrids for Environmental Applications. Environments 9:153.  
<https://doi.org/10.3390/environments9120153>.

2. Lujanienė G., Novikau R., **Joel E.F.**, et al (2022) Preparation of Graphene Oxide-Maghemite-Chitosan Composites for the Adsorption of Europium Ions from Aqueous Solutions. *Molecules* 27:1–20. <https://doi.org/10.3390/molecules27228035>.
3. **Joel E.F.**, Lujanienė G., Ashok A., Yamaguchi N., Stanionytė S., Grinevičiūtė L., Levinskaitė L., Talaikis M., Preparation and Characterization of Graphene Oxide-Chitosan thin films for food packaging applications. *Scientific reports*, (in press).

## LIST OF CONFERENCES

1. **Edith Flora Joel**, Galina Lujanienė, Sandra Stanionytė, Martynas Skapas, Loreta Leviskaitė ANTI-BACTERIAL PROPERTIES OF THIN FILMS BASED ON GRAPHENE OXIDE-CHITOSAN-COPPER-PLATINUM NANOCOMPOSITES Conference of Doctoral Students and Young Researchers FizTech (FizTech2020), 22 – 23 October 2020, Vilnius, Lithuania, Oral presentation.
2. **Edith Flora Joel**, Galina Lujanienė, Sandra Stanionytė, Martynas Skapas, Loreta Leviskaitė GRAPHENE OXIDE / CHITOSAN / COPPER NANOCOMPOSITES FOR ANTIBACTERIAL STUDIES Open Readings 2021“, 16-19th of March 2021, Vilnius, Lithuania, oral presentation.
3. **Edith Flora Joel**, Galina Lujanienė, Sandra Stanionytė, Martynas Skapas, Loreta Leviskaitė ANTIBACTERIAL PROPERTIES OF THIN FILMS BASED ON GRAPHENE OXIDE CHITOSAN COPPER PLATINUM NANO COMPOSITES. Conference of Doctoral Students and Young Researchers FizTech2021, 20–21<sup>st</sup> October 2021, Vilnius, Lithuania, oral presentation.
4. **Edith Flora Joel**, Galina Lujanienė, Sandra Stanionytė, Martynas Skapas, Loreta Leviskaitė SYNTHESIS AND APPLICATION OF THIN FILMS OF GRAPHENE NANOCOMPOSITE CHITOSAN COPPER PLATINUM FOR ENVIRONMENTAL APPLICATION. Chemistry and chemical technology 2021, Vilnius September 24-25, 2021. Poster presentation.
5. **Edith Flora Joel**, Galina Lujanienė, Sandra Stanionytė, Martynas Skapas, Loreta Leviskaitė TWO-DIMENSIONAL COMPOSITE BASED ON CHITOSAN-GRAPHENE OXIDE ASSESSMENT OF

ANTIMICROBIAL ACTIVITY. Conference of Doctoral Students and Young Researchers FizTech (FizTech2022), 22 – 23 October 2022, Vilnius, Lithuania, Oral presentation.

6. **Edith Flora Joel**, Galina Lujanienė, Sandra Stanionytė, Martynas Skapas, Loreta Leviskaitė ANTIBACTERIAL PERFORMANCE OF HYBRID THIN FILMS DECORATED WITH COPPER AND ITS OXIDES: A MACHINE LEARNING PERSPECTIVE Chemistry and chemical technology 2022, Kaunas, September 24-25, 2022. Oral presentation.
7. Climate Neutrality Forum event, University of Oxford, September 08, 2021 - September 09, 2021.
8. Summer School - YOUNG RESEARCHER FORUM ON SUSTAINABLE BIOMASS AND CLIMATE CHANGE Oct 19th to Oct 22, 2021.
9. Introduction to Sustainable Remediation - Principles and Practices, 20 SEPTEMBER 2022, REMTECH Europe
10. Symposium on Compositional Structures. Tallinn, Dec 13-14, 2021.

## 1. LITERATURE REVIEW

### 1.1. Food Packaging

#### 1.1.1. Polymers in food packaging

Petroleum-derived plastics, also known as synthetic polymers, are widely used in the food industry for packaging purposes, making them a very popular material in this sector. These polymers include polyethylene (PE), polypropylene (PP), low-density polyethylene (LDPE), polyvinyl chloride (PVC), high-density polyethylene (HDPE) and polystyrene (PS) polyethene terephthalate (PET) (Muncke, 2016). Consumer awareness of environmental issues has driven a significant shift towards sustainable practices (Camilleri et al., 2023; Young et al., 2010). Due to its large production volume, short shelf life, non-biodegradable nature and poor handling, plastic has raised concerns around the world. Multi-layered polymers also make recycling difficult (Matthews et al., 2021). Plastic containers are differently permeable to small molecules such as gasses, water vapour, organic vapours and other low molecular weight substances such as flavours and additives in food compared to materials such as glass or metal used for packaging. The transfer of these substances from the external environment to the food is influenced by the barrier properties of the material (Siddiqui et al., 2023; Taylor & Sapozhnikova, 2022).

The choice of different polymers for food packaging depends on the specific properties of the food. In addition, the properties of the packaging material, such as its barrier properties, can be strongly influenced by the production, use and packaging techniques. These processes are related to the internal structure of the polymer, which includes aspects such as the degree of crystallinity, the ratio of crystalline to amorphous phases, the polymer composition, thermal and mechanical processing before and after contact with food, the presence of polar or non-polar chemical groups in the polymer, the degree of cross-linking and the glass transition temperature (Mrkić et al., 2006). In the food industry, the choice of packaging material is important to withstand human handling and protect the integrity of the food. In addition, it should provide effective barrier properties against gasses used in modified atmosphere packaging (MAP) processes, such as oxygen (O<sub>2</sub>), nitrogen (N<sub>2</sub>) and carbon dioxide (CO<sub>2</sub>) (Galotto et al., 2008). These advantages include their ability to degrade naturally, their environmentally friendly properties, their non-toxicity and their ability to work well with biological systems. The

natural biopolymers possess intrinsic properties that help in creating strong cohesive structures and forming thin protective layers (Luckachan & Pillai, 2011). Food packaging materials derived from biopolymers include polysaccharides, proteins, and aliphatic polyesters. These materials are used to preserve the quality of food and extend its shelf life. In addition, biopolymers have antimicrobial properties that protect food from external contamination. These materials are also effective in preventing the degradation of beneficial compounds such as flavor and texture (Chaudhary et al., 2020; Hou et al., 2019).

The biopolymer chitosan and its derivatives belong to a group of biodegradable polysaccharides with numerous beneficial properties for food packaging. Chitosan is safe and well tolerated and shows antibacterial and antifungal properties as well as the ability to bind metals (Aider, 2010; Bakshi et al., 2020). Chitosan, a natural polymer obtained by deacetylation of chitin, is being considered for potential use in food packaging due to its ability to decompose, its antimicrobial effect and its ability to form films. Chitosan-based films have been identified as a potential alternative to conventional food packaging, improving both food quality and shelf life (No et al., 2007; H. Wang et al., 2018). The antimicrobial capabilities of chitosan are beneficial in biodegradable polymers for antimicrobial food packaging and contribute to food preservation and safety (Gumienna & Górná, 2021). In addition, the ability of chitosan to produce cross-linked films improves its suitability for food packaging that provides antimicrobial protection against various microorganisms (Tripathi et al., 2009). For example, chitosan films cross-linked with hydroxycinnamic acids have been shown to be effective in preserving meat products (Yong et al., 2021). The addition of chitosan to cellulose nanocrystals also improved their antimicrobial, thermal, mechanical and barrier properties, making them suitable for food packaging (Díaz-Cruz et al., 2022).

In addition, chitosan has gained much attention for potential applications in the culinary, medicinal and chemical fields due to its exceptional film-forming ability (Siripatrawan & Harte, 2010). Studies have shown that the incorporation of additional active components into chitosan films has intriguing results in terms of their mechanical, barrier and functional properties, also, the inherent composition of the packaged food (such as pH value, fat content and flavourings) can influence the sorption properties of the packaging materials (Grande-Tovar et al., 2018; Hafsa et al., 2016; Z. Li et al., 2019; Pastor et al., 2013; Perdones et al., 2014; Sánchez-González et al., 2010).

The antimicrobial properties make chitosan a suitable choice for the development of active packaging systems that can extend the shelf life of food (Aider, 2010; Musella et al., 2021). Cross-linking chitosan films with carvacrol and pomegranate peel extract can also improve food safety and quality (Yuan et al., 2015). Similarly, the addition of essential oils to chitosan films can enhance antimicrobial properties and improve barrier properties without altering microbial inhibition (Imawan et al., 2022; L. Wang et al., 2011). Although chitosan films have significant potential as a food packaging alternative to conventional petroleum-based packaging, there are still some limitations. Chitosan films exhibit reduced mechanical properties due to disruptions in the formation of a structured crystalline layout within the chitosan scaffold, resulting in impaired intermolecular bonding and flexible segments in the films (L. Sun et al., 2017). In addition, chitosan films have a reputation for being very sensitive to moisture and having poor mechanical properties, which limits their use in various industries, especially in food packaging (Abdullah et al., 2023). Limitations that hinder the use of chitosan films in food packaging include a persistent acetic acid taste, inferior mechanical properties, and insufficient water vapour barrier (J. Xu et al., 2022). In addition, the fragility of chitosan films is highlighted as an obstacle limiting their use in packaging (Shen et al., 2021). The fact that chitosan is insoluble at neutral pH is also cited as an obstacle to its use (Özdemir & Gökmen, 2019). In addition, chitosan films are known for their high moisture absorption and comparatively low mechanical strength compared to conventional plastics, which limits their use in packaging (Khouri et al., 2019). To overcome these limitations, current research is focusing on the development of chitosan-based nanocomposites for food packaging. By incorporating nanofillers and nanoparticles into chitosan films, researchers aim to overcome the limitations associated with mechanical and barrier properties, thereby potentially contributing to the bioplastics segment. For example, chitosan films reinforced with GO showed improved tensile strength and barrier properties (Pal et al., 2021). The addition of graphene oxide and zinc oxide to the chitosan matrix also led to an improvement in the mechanical properties and thermal stability of biocomposite films produced with chitosan (Terzioglu et al., 2020).

#### 1.1.2. Chitosan-graphene oxide nanocomposites in food packaging

Graphene has extraordinary optical, mechanical, electrical and thermal properties that make it a distinctive and unique material. Recently, interest in

graphene-based nanostructures has increased significantly (Priyadarshi & Rhim, 2020). Graphene can be described as a two-dimensional bilayer consisting of carbon particles arranged in a honeycomb lattice (Lingamdinne et al., 2019). The material graphene is biocompatible and exhibits minimal or no cytotoxicity. In addition, its oxidized state has unique attributes and exhibits antibacterial properties in solution and when applied to various surfaces. The antibacterial efficacy of graphene-family composites can be attributed to numerous inherent properties resulting from their geometric and electrical structures. The predominant mechanism believed to be responsible for the antibacterial effect of graphene is oxidative stress (Gurunathan et al., 2012). This phenomenon is characterized by the transport of electrons from graphene to the microbial thin films, disrupting protein activities and lipids through the formation of reactive oxygen species (ROS). In addition, it is possible to enhance the antimicrobial properties of the graphene family through the covalent bonding of molecules and the deposition of metal ions on its surface. The graphene-based nanocomposites have the potential to contain various nanoparticles such as metal ions/oxides/sulphides (e.g., manganese disulfide, cadmium sulphide), titanium dioxide, zinc oxide, copper oxide, polymers, and antibiotics among other constituents (A. A. P. Khan et al., 2017). The use of nanotechnology in conjunction with the graphene family and its composites is a promising approach to combat microbial agents in various contexts. Graphene oxide (GO) and reduced graphene oxide (rGO) are other graphene structures that are currently being investigated for their diverse applications in various fields, including sensors, energy storage, water purification, optoelectronics, and related disciplines (Y. Zhu et al., 2010). Therefore, it is important to understand the difference between graphene oxide and reduced graphene oxide.

The carbon to oxygen ratio of GO often shows values below 3:1 and close to 2:1. In the last decade, numerous research works have been conducted to investigate the environmental applications of GO–metal hybrids. The synthesis route plays an important role in determining the surface chemistry, lateral size and crystalline structure of the hybrids. Similarly, the synthesis methods can affect both the distribution of pore sizes and the interlayer spacing (Ioniță et al., 2017; A. A. P. Khan et al., 2017; Lim et al., 2018). In addition, the combination of graphene oxide/reduced graphene oxide (GO/rGO) with nanostructures composed of metals or metal oxides showed synergistic properties (Bijesh et al., 2022). The current use of graphene derivatives, especially graphene-based nanomaterials, in the context of biopolymer-based composites for food packaging applications (Rossa et al.,

2022). The incorporation of graphene derivatives represents a valuable improvement of bio-based formulations and leads to remarkable advances in various aspects such as physicochemical, mechanical, barrier and functional properties. These improvements include desirable properties such as antioxidant activity and electrical conductivity (Barra et al., 2019). In addition, the evaluation of the toxicity and biocompatibility of graphene oxide is of great importance when considering its potential use in food packaging (Dinescu et al., 2014). The potential impact of graphene oxide on human health and the environment needs to be fully investigated, notwithstanding its promising applications in food packaging (Alves et al., 2022; Rossa et al., 2022; Yilmaz Dogan et al., 2022). Another form of graphene, carbon nanoparticles, have also demonstrated their effectiveness in removing micropollutants and harmful microorganisms from wastewater in a number of technological processes (Aftab et al., 2022; Nupearachchi et al., 2017). The incorporation of graphene oxide into chitosan films has been investigated to improve the performance of chitosan composite films for food packaging applications. For example, GO dispersed in chitosan film matrices showed improved mechanical properties (X. Yang et al., 2010). Although chitosan alone exhibited antimicrobial effects, chitosan-GO films also showed enhanced antimicrobial properties (X. Wang et al., 2010). The incorporation of GO into chitosan films also improves their mechanical and microbial inhibition properties (Jia et al., 2022).

Although the mechanical properties of chitosan are improved when graphene oxide is added as a filler, the low mechanical strength and loss of structural integrity of chitosan films remain a problem that limits their applications. And the uniform dispersion of graphene materials in the polymer matrix is an important challenge before the realization of high-performance graphene-based nanocomposites. This is another problem that may arise in the large-scale production of CS-GO nanocomposite films (X. Yang et al., 2010). In addition to the problems associated with commercial production, it is also important to consider potential environmental issues associated with the disposal of CS-GO nanocomposite films. Concerns regarding the potential release of nanoparticles into the environment and the environmental impact of the use of nanomaterials in food packaging are raised by this practice.

### 1.1.3. Copper and platinum nanoparticles in Food Packaging

Copper nanoparticles (NPs) are widely used as catalysts, optical components, antibacterial and antifungal agents, and conductive agents due to their special physicochemical and biological properties (Anyaogu et al., 2008; Keihan et al., 2017; Nasrollahzadeh et al., 2019; Sinha et al., 2022). The efficacy of copper nanoparticles in combating various foodborne pathogens such as *Escherichia coli*, *Listeria monocytogenes* and *Salmonella enterica* has been demonstrated (Osaili et al., 2019; Raffi et al., 2010; Sharma et al., 2017). Cu nanoparticles have been reported to inhibit bacteria by interacting with amino and carboxyl groups on the cell walls of Gram-positive bacteria (Ebrahimiasl & Rajabpour, 2015). Studies have shown that copper nanoparticles (CuNPs) have the ability to effectively integrate into polymeric matrices and exert their biotechnological effects. This can be attributed to their remarkable surface-to-volume ratio, reactivity and suitable release properties. There are several probable pathways through which copper exhibits bactericidal properties. Three main factors contribute to the deleterious effects of copper on cells. First, excessive amounts of copper lead to oxidative stress in cells. Secondly, the osmotic pressure is altered, causing important nutrients such as magnesium to escape from the cells. And finally, copper can bind non-specifically to proteins and impair their standard functionality (Espírito Santo et al., 2011).

In general, CuO exhibits a wide range of properties and is applicable in many fields, making it a promising candidate for a variety of disciplines, including the field of biodegradable food packaging (Košiček et al., 2022; Lupan et al., 2016; Mesgari et al., 2022a). The catalytic properties of CuO have been investigated in connection with selective CO oxidation (Gamarra et al., 2007). The antibacterial properties of CuO nanoparticles have been investigated and suggest their potential application in the development of biodegradable food packaging (Borkow et al., 2010). Oxidation of copper surfaces can form carrierless monolayers of CuO that are only one atom thick. These monolayers exhibit different properties and have promising potential for numerous applications. In particular, the potential toxicity of CuO nanoparticles has been investigated in terms of their interactions with living cells and organisms (Brewer, 2010; K. Yin et al., 2016). The integration of CuO nanoparticles into biopolymer films represents a viable approach for the development of an active packaging system that effectively prevents the proliferation of bacteria, viruses and fungi (Khashan et al., 2016). The incorporation of CuO nanoparticles into packaging films can improve their

mechanical properties, water resistance and surface hydrophobicity (Roy & Rhim, 2019). It has also been found that the incorporation of CuO nanoparticles into films leads to an improvement in their ability to block UV radiation. This improvement protects packaged food from degradation due to exposure to light. CuO nanoparticles are promising as biodegradable food packaging materials as they have better antibacterial properties and higher performance.

Cuprous oxide ( $\text{Cu}_2\text{O}$ ) is a notable metal oxide semiconductor of the p-type, possessing a straight bandgap of 2.2 eV. This characteristic renders it a promising candidate for the conversion of solar energy. The current findings indicate that  $\text{Cu}_2\text{O}$  demonstrates stability as a catalyst for water splitting under visible light conditions, namely at 600 nm (Hara et al., 1998; Ikeda et al., 1998). Copper oxide ( $\text{Cu}_2\text{O}$ ) has demonstrated potential in biodegradable food packaging owing to its antibacterial qualities and ability to improve the shelf life of packed food goods. The optical, electrical, and catalytic characteristics of  $\text{Cu}_2\text{O}$  have also been previously examined (Yan et al., 2021a). Furthermore, the utilization of  $\text{Cu}_2\text{O}$  nanoparticles has been the subject of investigation with regard to their potential application in the process of photocatalytic degradation of organic pollutants, as evidenced (Gaim et al., 2019).  $\text{Cu}_2\text{O}$  possesses antibacterial capabilities, rendering it a viable contender for the development of active food packaging solutions aimed at preserving the quality and safety of food products (L. Zhu et al., 2020). However, additional research is needed to thoroughly understand the impacts of  $\text{Cu}_2\text{O}$  in biodegradable food packaging and its possible interplay with food and the surrounding ecosystem.

The structure and chemical nature of the bacterial cell wall influence the antibacterial activity of copper nanocomposites and determine the sensitivity or tolerance of bacteria to certain drugs (Madigan et al., 2018). Gram-negative bacteria pose a greater threat to antimicrobial drugs because of their barrier properties, due to their strong cell walls. Based on their degree of oxidation, copper nanoparticles (Cu NPs) exhibit a variety of antibacterial properties (Hans et al., 2015). Cu NPs have better electron transport and uptake capacity than copper oxide nanoparticles (CuO NPs), which explains why they exhibit greater antibacterial activity (Akhavan & Ghaderi, 2010). Upon direct contact, both Cu NPs and  $\text{Cu}_2\text{O}$  NPs show strong bactericidal abilities (Hans et al., 2013). However, CuO NPs show a greater ability to induce reactive oxygen species (ROS) production, possibly due to their involvement in Haber-Weiss and Fenton-type reactions (Padmavathi et al., 2020).

Platinum nanoparticles have different properties, including the surface effect, the volume effect, the quantum size effect, and the macroscopic quantum tunnel effect. These nanoparticles can be prepared by various techniques to obtain materials with different physical and chemical properties (Choi et al., 2017; M.-Q. Wang et al., 2008). Platinum nanoparticles are widely used in biosensors for the detection of food toxins such as ethanol *salmonella*, *natamycin* and *E. coli* (Bharathan et al., 2019; Dehghani et al., 2021; Ozdokur et al., 2016; Yousefi et al., 2018).

The use of polymers in the development of nanocomposites with antimicrobial properties for food packaging not only serves as a carrier for nanoparticles, but also has the potential to increase the antibacterial efficacy of the nanocomposites. This behavior is mainly due to three phenomena:

1. the nanocomposite exhibits improved antibacterial properties compared to the individual components, which is due to the synergistic interaction between the polymer and the copper nanoparticles (Bogdanović et al., 2015).
2. The nanocomposite showed prolonged antibacterial activity due to the ability of the polymer to release ions over a longer period (Bikiaris & Triantafyllidis, 2013).
3. The degree of antimicrobial activity is influenced by the increased surface area resulting from the effective dispersion of Cu nanoparticles within the polymer matrix. Currently, there is limited research on chitosan-copper nanocomposites for food packaging and coatings (Nouri et al., 2018a; Saharan et al., 2015).

The combination of two or more metal and metal oxide nanoparticles has been found to have higher antimicrobial activity compared to individual metal nanoparticles such as Zn/Fe oxides against *S. aureus* and *E. coli* (Gordon et al., 2011). Zn/Mg oxides against *E. coli* and *B. subtilis* (Vidic et al., 2013) TiO<sub>2</sub>/Ag against *S. aureus* (Zawadzka et al., 2016); Zn-doped CuO against *E. coli* and *S. aureus* (Malka et al., 2013) and Cu-doped TiO<sub>2</sub> against Mycobacterium smegmatis and Shewanella oneidensis (B. Wu et al., 2010). Also, bimetallic nanocomposites have several benefits for food packaging, one of which is a reduction in the possibility of migration (Biswas et al., 2019; Tiimob et al., 2017; Vishnuvarthan & Rajeswari, 2019). High barrier performance improved mechanical and thermal qualities, and increased stability and shelf life of food goods are all provided by these nanocomposites such as (Cu<sub>2</sub>O-Ag)@TA (Z. Yang et al., 2019), Cu|Cu<sub>2</sub>O-NPs (Jaramillo et al., 2019).

#### 1.1.4. Migration of nanoparticles to food

The determination of human exposure to nanomaterials is based on the results of migration tests, while the estimation of acceptable exposure limits is based on animal studies (Cushen et al., 2012). The European Commission (EC) has formulated regulations and requirements describing the specific conditions that require migration testing (EFSA Scientific Committee et al., 2019). The selection of food simulants recommended for testing the interaction between the packaging and the type of food includes water, acetic acid (3 % v/v), ethanol (10 % v/v and 50 % v/v) and vegetable oil.

The investigation of foods has been hindered by a lack of analytical tools for the advancement of instruments and techniques. Further investigation will be necessary in this domain. The identification, measurement, and distribution analysis of nanoparticles hold significant importance, necessitating the utilization of non-invasive and unrestricted methodologies. In this methodology, a substrate coated with nanoparticles serves as a reference material. This substrate is integrated with analytical and imaging systems that focus on screening techniques such as mass spectroscopy for determining the composition of the test material (Song et al., 2011), dynamic light scattering (DLS) for analysing the particle size distribution, positron emission tomography for radio-tracing purposes, spectroscopy for assessing NP size, and optical emission spectrometry for trace level elemental analysis (Bott et al., 2014; Shamhari et al., 2018). These systems are employed to monitor and collect adequate data. In another approach for assessing the presence of harmful substances in food, a sensor-based system employing nanoparticles in solution or nanostructured surfaces is utilized. The aforementioned characterization system is capable of detecting variations in the electronic states of the adsorbate (chemical signal enhancement) as well as alterations in the roughness of the metal (electromagnetic signal enhancement). The primary mechanism employed in this procedure involves the chemisorption of the analysis onto the surface of the biosensor's nanoparticles. Copper oxide nanoparticles have been widely recognized for their antibacterial properties. Methylcellulose films combined with gelatine-stabilized CuO NPs were found to demonstrate just 0.12 µg/mg of Cu migration; this can be further decreased by refrigerating the food products at 0–4 °C. It's interesting to note that the created nanopackaging prevented the formation of different microbiological pollutants, delaying the deterioration of tomatoes and strawberries on days four and seven (Gvozdenko et al., 2022). Also, Cheese was shielded from microbiological pollutants and 4.21 log CFU/g of coliforms after one month of refrigeration thanks to low-density

polyethylene (LDPE) coated with nano CuO (Beigmohammadi et al., 2016). However, it is important to note that the release of copper ions embedded in a polymer matrix into food can result in leaching, which may accelerate the degradation of food and potentially introduce toxicity concerns (Cushen et al., 2012; Hannon et al., 2016; R. Hosseini et al., 2017).

Therefore, Nouri et al., (2018) observed that the incorporation of MMT in conjunction with exchangeable cations that carry a positive charge, such as  $\text{Na}^+$  or  $\text{Ca}^{2+}$ , has the potential to inhibit the release of copper ions. However, it is important to note that the extent and speed of this migration process might differ based on several factors such as the specific packaging material employed, the nature of the food or beverage being packaged, and the specific conditions under which the packaging is utilized. The migration of copper from a food packaging coating composed of silver and copper nanoparticles, as well as polystyrene-polyethylene oxide block copolymer, beyond the regulatory limits when exposed to an acidic food simulant. However, the computed margin of exposure indicated that the usage of this coating would be considered safe in a hypothetical scenario (Hannon et al., 2016). The release of copper from copper metal foil and commercial copperware into food simulants was observed to be influenced by temperature and pH (Koontz et al., 2020). The study also suggests that there are some measures that may be implemented to minimize the release of copper from food contact surfaces into meals and beverages. Canned food products available in the Indian market were found to have quantities of aluminium, iron, manganese, silicon, and tin that exceeded the acceptable limits set by the FAO/WHO Codex Alimentarius Commission (Parkar & Rakesh, 2014).

The primary focus on the migration of nanoparticles into foodstuff is around the determination of the maximal level of migration. Migration is defined as the collective movement of particles possessing low molecular weight. Both overall and migration tests have limitations that vary depending on the food being tested. These limitations are established by regulatory bodies such as the European Food Safety Authority (EFSA) and the Food and Drug Administration (FDA). As per the European Food Safety Authority (EFSA), a migration test refers to the process of assessing the transfer of packaging constituents into food or food simulants. Food stimulators include ethanol at a concentration of 10 % v/v, acetic acid at a concentration of 3 % v/v, and ethanol at a concentration of 50 % v/v, among others. Despite the existence of multiple studies on the measurement of migrating silver, clay, and titanium nanoparticles in food, there is a scarcity of research on copper

nanoparticles ( Liu et al., 2016). Therefore, further investigations should be conducted to address this gap.

## 1.2. Nanocomposite for the removal of radionuclides

### 1.2.1. Maghemite

The magnetic iron oxide nanoparticle known as maghemite ( $\gamma$ -Fe<sub>2</sub>O<sub>3</sub>) has aroused great interest in the scientific community due to its special properties and potential uses (Baaziz et al., 2014). The compound has been synthesized using various techniques and its physicochemical properties, stability and potential use in biological contexts have been extensively studied (Laurent et al., 2008). The reproducible adjustment of the size and content of maghemite nanoparticles allows precise control of their properties. The mineral magnetite, chemically represented as Fe<sub>3</sub>O<sub>4</sub>, is known for its ferromagnetism. The magnetic behaviour of maghemite nanoparticles is influenced by oxidation defects, surface spin canting and volume spin canting. Maghemite ( $\gamma$ -Fe<sub>2</sub>O<sub>3</sub>) has been extensively studied for its adsorption properties towards various substances (Fig. 1). For example, maghemite nanoparticles have shown fast adsorption kinetics for selenium (IV) due to their high surface-to-volume ratio. Maghemite is used in various applications, especially in the adsorption of radionuclides (Afkhami & Norooz-Asl, 2009; Etale et al., 2016; Petcharoen & Sirivat, 2012; Yadav et al., 2020a). Maghemite has been shown to be effective in the adsorption of As (V), Cr (VI), Cu (II) and Ni (II) (Tuutijärvi et al., 2009). The adsorption of arsenic species such as arsenite and arsenate on maghemite was studied using extended X-ray absorption fine structure (XAFS) spectroscopy, which provided insights into the nature of the adsorption complexes (Morin et al., 2008). Maghemite nanoparticles were also synthesized and used to enhance the removal of Sb (III) (W. Zhao et al., 2021).

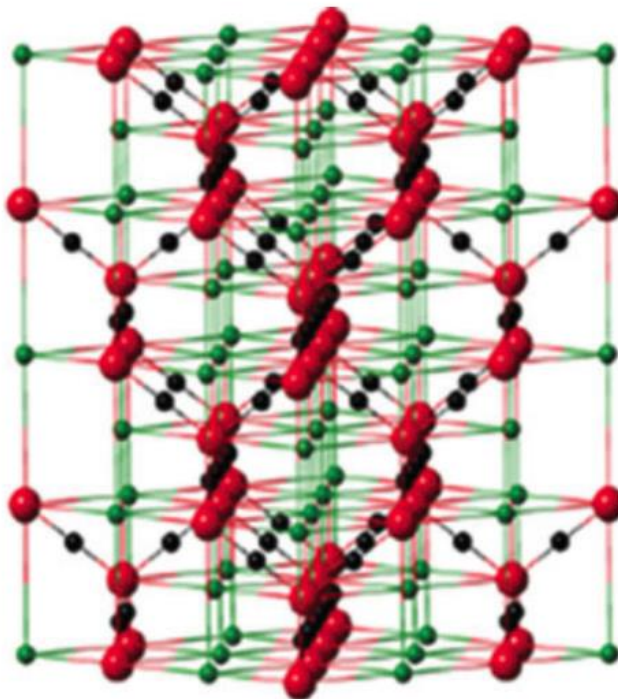


**Fig. 1.** Crystal structure of Maghemite cube (Chokkareddy et al., 2018).

#### 1.2.2. Graphene oxide as an adsorbent

Graphene oxide (GO) is a layered carbon-based material with a significant oxygen content that has a greater adsorption capacity and higher dispersion in aqueous environments compared to graphene. Despite extensive studies on the adsorption of radionuclides with graphene oxide-based sorbents, the exact mechanism of interaction between sorbents and radionuclides is still unclear (Huang et al., 2019; Mohanty et al., 2022; Y. Sun et al., 2012). Kuzenkova et al., (2020) provided a comprehensive elucidation of the adsorption and interaction mechanisms of Am (III)/Eu (III), Cs (I) and U (VI) on defective graphene oxide. Graphene oxide was synthesized using different synthetic methods, namely the Hummer, Brodie and Tour methods, referred to as HGO, BGO and TGO, respectively. Based on the results of the adsorption experiments, it was shown that the interaction between Am (III)/Eu (III) and U (VI) occurs via carboxyl functional groups. In addition, the application of density functional theory (DFT) calculations

together with extended X-ray absorption fine structure (EXAFS) and high-energy resolution fluorescence detection X-ray absorption near-edge structure (HERFD-XANES) studies provided evidence suggesting that the radionuclides predominantly occupy free defect sites within the GO layers. Another study by Boulanger et al., (2020) supports the findings of Kuzenkova et al., (2020). This study proposes the use of highly defective graphene oxide (dGO) for the effective sorption of uranium (VI) and americium (III). The dGO material exhibited a peak adsorption capacity of  $Q_{\max} = 2250 \text{ mmol/g}$  at a pH of 5.1. This phenomenon can be attributed to the interaction between uranyl cations and carboxyl groups located within the defects in the GO structure. The process of thermal expansion was accompanied by oxidation, which was favoured by the use of ammonium persulfate and nitric acid. In contrast to dGO, the U (VI) adsorption capacity of 3D GO was lower ( $1950 \mu\text{mol/g}$ ). The described phenomenon was attributed to the collapse of the pores during the oxidation process, which was then followed by thermal expansion. Therefore, it might be more appropriate to consider a mild oxidation of the material that does not affect its porous structure. Alternatively, treatment of the material prior to thermal expansion might be a more reasonable approach.

The use of Magnetite GO nanocomposites has been employed in the aforementioned procedure for the purpose of eliminating detrimental pollutants, including radionuclides (Lujanienė et al., 2016, 2017; Minitha et al., 2018). The utilisation of nanocomposites based on graphene oxide has proven to be highly efficient in the process of adsorbing several heavy metals, including lead (Pb), cobalt (Co), nickel (Ni), and uranium (U). The utilisation of nanoscale iron supported on reduced zero-valent graphene oxide has been employed for the purpose of adsorbing radioactive U (VI) (Wu et al., 2013). Nanocomposites based on graphene oxide (GO) are often preferred for the purpose of attaching organic molecules due to their significant surface area and high reactivity. GO demonstrates substantial  $\pi$ - $\pi$  stacking interactions with a benzene ring, rendering it a highly suitable contender for eliminating organic molecules from polluted water sources. Nevertheless, it is worth noting that ion exchange and chemical reduction processes can have significant implications in this context. The utilisation of GO has been found to be beneficial in the extraction of various radioisotopes, including Th (IV), Pu (IV), Am (III), Eu (III), U (VI), Sr (II), Tc (VII), and Np (V), from a simulated nuclear waste solution (Romanchuk et al., 2013).

The adsorption capacity of manganese oxide ( $\text{MnO}_2$ ) is considerable, making it an effective means of removing heavy metal ions and Th (IV) ions from wastewater. This effectiveness can be attributed to its affordability, large

surface area, moderate oxidation properties and stability in acidic environments. Xiu et al. (2019) utilized oxygen functional groups on graphene oxide nanoribbons (GONRs) as anchoring sites for a composite material composed of manganese dioxide ( $\text{MnO}_2$ ). This composite material, referred to as  $\text{MnO}_2$ -GONRs, was used to remove Th (IV). At a pH of 3, an upper limit of adsorption capacity was determined to be 166.11 mg. From a thermodynamic point of view, this particular process shows a spontaneous endothermic behaviour. A separate study showed that graphene oxide effectively eliminates the selection of highly hazardous and long-lived artificial radionuclides from contaminated water, including solutions with acidic properties and pH values below 2.0 (Kuzenkova et al., 2020). In a recent study, an investigation was carried out on the sorption behaviour of  $^{152+154}\text{Eu}$  within a composite material consisting of graphene oxide. The adsorption capacity exhibited a significant increase of up to 99 % as the pH increased from 1.5-5.5. The M-GO nanocomposites were synthesized using a coprecipitation technique to remove Sr (II) and Cs (I) ions (El-Shazly et al., 2022).

### 1.2.3. Chitosan as an adsorbent

According to the findings of Cadogan et al. (2014) there was a significant increase in the adsorption of europium ions on chitosan when the pH level increased from 2 to 3. At a pH value of 3, the adsorption process was stable, with an observed adsorption capacity of approximately 25 mg/g. The observed correlation between an increase in pH and an increase in adsorption capacity can be attributed to the augmentation of deprotonated adsorption sites. The augmentation of the adsorbent mass from 10 to 100 mg resulted in an enhancement of the adsorption efficiency, with values rising from 7.21 % to 98.1 %. However, this increase in mass led to a reduction in the adsorption capacity. Within the specified contact time range of 5–120 min, the adsorbent achieved equilibrium at the 60-minute mark, exhibiting a maximum adsorption capacity of 24.9 mg/g. The adsorption behaviour of europium on chitosan can be described by the pseudo-second-order kinetic model. The adsorption capacity of chitosan had a linear relationship with the initial concentration of Eu (III), as seen by an increase from 23 to 142 mg/g when the concentration was increased from 10 to 100 mg/L. In addition, it can be observed that the Langmuir model provides a more accurate fit to the experimental data compared to the Freundlich and Temkin models. The maximum adsorption capacity was determined to be 114.9 mg/g through

calculation. Zhang et al. (2020) showed in a pH effect test that the adsorption capacity of magnetic cyanoethyl chitosan beads towards cobalt ions slightly increases in the pH range of 5–8, as the adsorbent becomes more negatively charged with increasing pH. An increase in adsorption capacity of the adsorbent also occurs when the initial concentration of cobalt is increased in the range of 10–600 mg/L, while the adsorbent reaches saturation at 600 mg/L and the adsorption capacity at this initial concentration is ~17 mg/g. These data were fitted using the Langmuir, Freundlich, and Temkin models, with the Langmuir model fitting the data better. The calculated value for the maximum adsorption capacity was 17.92 mg/g. Kinetic studies showed that equilibrium on the adsorbent was reached in 120 min, and the pseudo-second-order kinetic model fit the obtained data well. Thermodynamic studies have shown that the adsorption process is endothermic and spontaneous. The authors also found that the adsorption of the adsorbate on the adsorbent occurs by chemisorption, where the –CN and –NH<sub>2</sub> groups are responsible for the adsorption of cobalt, with the –CN groups of the adsorbent occupying a dominant position. Previously studies showed the adsorption of radionuclides with chitosan like nanostructured chitosan/molecular sieve-4A (Goyal et al., 2020), chitosan modified with metal hexacyanoferrates (Zhuang et al., 2022), magnetic graphene oxide/chitosan (Zhuang & Wang, 2019). Although studies have been carried out on adsorption of caesium ions, cobalt ions, Pb ions, the adsorption of Eu (III) with Graphene Oxide-Maghemite-Chitosan for the first time.

#### 1.2.4. Adaptive neuro-fuzzy inference system

The adaptive fuzzy inference system (ANFIS) has gained significant popularity and is widely used across several domains for modelling and prediction activities. Although there is a lack of specialized literature on utilizing ANFIS for modelling radionuclides, we can rely on the broader capabilities and applications of ANFIS to explore its possible applicability in this particular domain. The Adaptive Neuro-Fuzzy Inference System is a computational model that integrates the learning capabilities of neural networks with the interpretability of fuzzy logic. architecture of the ANFIS comprises a collection of fuzzy if-then rules, which are acquired and refined through the utilization of a hybrid learning algorithm. This combination enables ANFIS to handle complicated relationships effectively and make predictions using inputs that are uncertain or imprecise (Jang, 1993). This approach has been successfully applied in various fields, including climate

change impact modelling (Nabipour et al., 2020), runoff estimation (Nath et al., 2019), control systems (Sahoo et al., 2020), and forecasting (Dariane & Azimi, 2016). In the realm of radionuclide modelling, the utilization of an ANFIS presents an opportunity to construct predictive models pertaining to radionuclide behaviour. These models can encompass various aspects, including the transport and dispersion of radionuclides in the environment. An ANFIS is capable of effectively addressing the nonlinearity and uncertainty present in input data, a prevalent characteristic within environmental systems (Agbaogun et al., 2021).

The training of ANFIS is primarily conducted on approximately 70 % of the datasets, while the remaining 30 % is allocated for testing purposes. The outcomes obtained from the testing phase serve as an unbiased evaluation of the network's ability to generalize. It is important to acknowledge that the data undergoes random selection before being inputted into the network. Additionally, in certain instances, the data is normalized within the range of 0 to 1. This normalization process aims to minimize the impact of factors with higher magnitudes on the ANFIS. The objective is to facilitate error-free analysis of the system. By employing ANFIS models trained using pertinent input variables, such as environmental characteristics and radionuclide attributes, it is possible to forecast the behaviour and destiny of radionuclides in diverse circumstances (Amiri et al., 2013; Banza & Rutto, 2023). Moreover, an Adaptive Neuro-Fuzzy Inference System can be effectively employed for data-driven modelling pertaining to the adsorption or movement of radionuclides within porous media. By conducting training on ANFIS models using either experimental or simulated data, it is possible to construct predictive models capable of estimating the adsorption capacity or migratory behavior of radionuclides under varying geological or environmental circumstances. The evaluation of an Adaptive Neuro-Fuzzy Inference System network's performance involves assessing the agreement between the experimental data and the predicted data using various statistical measures. These measures include the correlation coefficient, determination coefficient, mean squared error, sum of squared errors, average relative error, mean absolute error, sum of absolute error, absolute average deviation, and root mean square values (Agbaogun et al., 2021; Souza et al., 2018).

## 2. MATERIALS AND METHODS

### 2.1. Synthesis of materials for food Packaging

#### 2.1.1. Preparation of graphene oxide-chitosan-platinum-copper oxides/copper composites and thin film

Graphene Oxide: To make GO, a modified Hummers' method was used to oxidize expanded graphite. The process involved adding 4.0 g of graphite (<20  $\mu\text{m}$  synthetic, Sigma-Aldrich) flakes and 3.0 g of  $\text{NaNO}_3$  (Absolute, Merck) to 300 mL of concentrated  $\text{H}_2\text{SO}_4$  while stirring vigorously in an ice-water bath. Then, 2 h later, 18.0 g  $\text{KMnO}_4$  was added to the mixture slowly throughout 18 h. The suspension was constantly stirred for 48 h. Next, 560 mL of 5.0 wt. %  $\text{H}_2\text{SO}_4$  was added to the suspension while it was being mixed hard at 981  $^{\circ}\text{C}$  for approximately 2 h. After the temperature of the suspension dropped to 60  $^{\circ}\text{C}$ , 24 mL of  $\text{H}_2\text{O}_2$  (30 wt. %) was added to remove the extra  $\text{KMnO}_4$ , and the suspension was stirred constantly at room temperature for 2 h. Finally, the colour of the mixture changed from dark brown to yellow. After 60 min of centrifugation at 20,000 rpm/min, the solid phase was broken up with a strong stir and an ultrasonic water bath. The solution was then cleaned with Milli-Q (Milli-Q Synthesis A10) water until the pH was close to that of Milli-Q water.

Graphene oxide-chitosan-platinum (GO-CS-Pt): Briefly, 125 mg of chitosan (average molecular weight: 190–310 kDa,  $\leq 75\%$  deacetylation; Sigma-Aldrich) was mixed with 37.5 mg of  $\text{KMnO}_4$ , 0.75 mL  $\text{H}_2\text{SO}_4$  and incubated for 3 h at a fixed temperature of 37  $^{\circ}\text{C}$ . The resulting mixture was then incubated for a duration of 3 hours, maintaining a constant temperature of 37  $^{\circ}\text{C}$ . Following this, a suspension of synthesised graphene oxide (0.5 mL at a concentration of 30 mg/mL) was thoroughly combined with processed CS (0.5 mL), resulting in the development of a precipitate known as Graphene Oxide-Chitosan (GO-CS). Initially, 20 mg of the GO-CS molecule was dispersed in 40 mL of deionized water through ultrasonication. Subsequently, the GO-CS colloidal dispersion was subjected to ultrasonic conditions, during which 50 mL of a sodium hydroxide ( $\text{NaOH}$ ) solution with a concentration of 1 mol  $\text{L}^{-1}$  and 1.2 mL of a  $\text{H}_2\text{PtCl}_6$  solution with a concentration of 38.68 mmol  $\text{L}^{-1}$  (mM) were introduced. The mixture was then mixed for 30 min at ambient temperature. Subsequently,  $\text{NaBH}_4$  solution was introduced incrementally by magnetic stirring. The reaction was conducted for an

extended period at ambient temperature, and the anticipated outcomes were obtained by centrifugation. The samples were subsequently subjected to drying at 45 °C for 6 h. The outcome of this process was a powdered substance referred to as the (GO-CS-Pt) nanocomposite.

Copper and copper II oxide (Cu and CuO) : In a round-bottom flask, 20 g of CuSO<sub>4</sub>·5H<sub>2</sub>O was added and dissolved in distilled water under magnetic stirring for 10 min at 60 °C. The solution was then adjusted to a pH of approximately 9 by gradually adding sodium hydroxide (0.625 M), causing the solution to change colour to a dark blue colloidal. Next, a 20-milliliter solution containing 40 mg of L-ascorbic acid was added dropwise, and the reaction mixture was allowed to react for 30 min while maintaining constant stirring at 60 °C. The NPs were then recovered by centrifugation at 15,000 rpm and 25 °C, purified after washing twice with distilled water and ethanol, and finally dried at 60 °C for 2 h. The NPs was obtained in red and labelled as Cu. Similarly, CuO nanoparticles were synthesized without L-ascorbic acid as a reducing agent.

Copper (I) oxide (Cu<sub>2</sub>O): In a round-bottomed flask, 20 g of CuSO<sub>4</sub>·5H<sub>2</sub>O was added and dissolved in distilled water under magnetic stirring for 10 min at 60 °C. Subsequently, the pH of the solution was adjusted to approximately 9 by the gradual addition of sodium hydroxide (0.625 M), and the solution colour changed to dark blue. Then, ascorbic acid (0.9 g) and NaOH (0.4 g) were dissolved in 100 ml of deionized water, and the resulting solution was added to the previous solution. Finally, an aqueous solution (50 ml) of NaBH<sub>4</sub> (0.4 g) was prepared and mixed with the solution under constant stirring. As a result, an aqueous dark red solution was obtained. The nanoparticles were recovered by centrifugation at 15,000 rpm and 25 °C, purified after washing twice with distilled water and ethanol, and finally dried at 60 °C for 2 h. The resulting dark red nanoparticles were labelled as Cu<sub>2</sub>O.

Copper (I) oxide/Copper (Cu<sub>2</sub>O/Cu): A dark blue colloidal solution of CuSO<sub>4</sub>·5H<sub>2</sub>O at 0.625 M was added until a pH of 9 was obtained at 60 °C for 10 min., and ascorbic acid (0.9 g) and NaOH (0.4 g) were dissolved in 100 ml of deionized water. The resulting solution was added to the previous solution at 90 °C, and the reaction mixture was allowed to react for 10 min while being constantly stirred at 90 °C. The reaction mixture was placed in an ice bath and allowed to cool completely. A dark red precipitate was obtained. The nanoparticles were recovered by centrifugation at 15,000 rpm and 25 °C, purified after washing twice with distilled water and ethanol, and finally dried

at 60 °C for 2 h. The resulting nanoparticles were labelled as Cu<sub>2</sub>O/Cu and were brownish black in colour.

Preparation of graphene oxide-chitosan-platinum/copper oxide/copper nanocomposite: GO-CS-Pt based nanocomposites were prepared using a simple solvent evaporation method. In this process, 5 ml of 1.5 % v/v acetic acid was mixed with 20 mg of Cu, CuO, Cu<sub>2</sub>O, and Cu<sub>2</sub>O/Cu NPs individually.

Preparation of graphene oxide-chitosan-platinum/copper oxide/copper nanocomposite thin films: Drop-casting process was utilized for the preparation of chitosan films, including GO-CS-Pt/ CopperOxide /Copper/ nanocomposites. In this process, 5 ml of 1.5 % v/v acetic acid was mixed with 20 mg of Cu, CuO, Cu<sub>2</sub>O, and Cu<sub>2</sub>O/Cu NPs individually, dried and named as Chitosan-Graphene Oxide-Platinum-Copper (GO-CS-Pt-Cu), Chitosan-Graphene Oxide-Platinum-Copper(II)Oxide (GO-CS-Pt-CuO), Graphene Oxide-Platinum-Copper(I)Oxide (GO-CS-Pt-Cu<sub>2</sub>O), Chitosan-Graphene Oxide-Platinum-Copper(I)Oxide/Copper (GO-CS-Pt-Cu<sub>2</sub>O/Cu) nanocomposites.

To make a thin film, 20 mg of the copper nanocomposite powder was mixed with 0.6 mg of chitosan solution in 100 ml of H<sub>2</sub>O. The mixture was then placed on a silica glass plate and left to dry overnight. For comparison, a clean chitosan film was prepared by following the steps above. The nanocomposite films that were fabricated were GO-CS-Pt-Cu, GO-CS-Pt-CuO, GO-CS-Pt-Cu<sub>2</sub>O, and GO-CS-Pt-Cu<sub>2</sub>O/Cu, in that order. Before determining what, the dried films were like, they were pulled off the plate and dried in a vacuum oven at 35 °C for 48 h.

### 2.1.2. Characterization

The GO-CS-Pt-Cu, GO-CS-Pt-CuO, GO-CS-Pt-Cu<sub>2</sub>O, and GO-CS-Pt-Cu<sub>2</sub>O/Cu nanocomposites were characterized by X-ray diffraction analyses performed using a SmartLab X-ray diffractometer (Rigaku, Japan) and a D8 Advance X-ray diffractometer (Bruker AXS, Germany) equipped with an X-ray tube with 9- and 2.4-kW rotating Cu anode.

The GO-CS-Pt-Cu, GO-CS-Pt-CuO, GO-CS-Pt-Cu<sub>2</sub>O, and GO-CS-Pt-Cu<sub>2</sub>O/Cu nanocomposite films were characterized. The Fourier transform infrared (FTIR) spectra were recorded with a Vertex 70v vacuum spectrometer with a 2 cm<sup>-1</sup> spectral resolution using a KBr pellet for sample preparation,

Ultraviolet Spectroscopy Photon RT (Essent Optics, Belarus). All the synthesized with different concentrations of Cu<sub>2</sub>O/Cu, namely GO-CS-Pt-Cu<sub>2</sub>O/Cu(0.5), GO-CS-Pt-Cu<sub>2</sub>O/Cu(1), GO-CS-Pt-Cu<sub>2</sub>O/Cu(1.5), GO-CS-Pt-Cu<sub>2</sub>O/Cu(2) nanocomposite films were characterized by Atomic Force Microscopy (Veeco Inc., Edina, MN, USA), and EDX( 7100 also has a JEOL 129 eV resolution silicon drift detector (SDD) for X-ray energy dispersive spectroscopy (EDS) microanalysis. Field electric scanning electron microscopy (FE-SEM) (Jeol JSM7100F). Contact Angle Measurements of the thin films (Transferette® S, volume 0.5–10 µL, Brand GmbH). The migration of Copper Ions from the hybrid composite thin films was studied by ICP OES (Optima 7000 DV, Perkin Elmer, quantitative analysis).

Statistical analysis of the collected data was performed using Duncan's multiple range and ANOVA tests to determine statistically significant results (P < 0.05) and to present the results as mean±standard deviation. Statistical analyses were performed using GraphPad Prism software.

#### 2.1.3. UV visible spectroscopy

The transmittance of GO-CS-Pt-Cu<sub>2</sub>O/Cu(0.5), GO-CS-Pt-Cu<sub>2</sub>O/Cu(1), GO-CS-Pt-Cu<sub>2</sub>O/Cu(1.5), GO-CS-Pt-Cu<sub>2</sub>O/Cu(2) films was assessed using a UV-VIS spectrophotometer Photon RT (Essent Optics, Belarus), and the absorbance was measured at a wavelength of 600 nm, and the mean was computed of the five measurements for each sample. The film transparency was calculated by Eq. (1):

$$\text{Transparency} = \frac{A_{600}}{T} \quad (1)$$

Where A<sub>600</sub> is the absorbance of the film at 600 nm; T is the thickness of the film (mm)

#### 2.1.4. Antimicrobial activity of nanocomposites and thin films

This study aimed to examine the antibacterial properties of chitosan and its derivatives against *Escherichia coli* (*E. coli*) using both film contact methods. The culture of *E. coli* ATCC 25922, which was incubated for 24 h, was diluted in a sterile physiological solution and adjusted to a standardized turbidity of 108 colony-forming units per millilitre (CFU/mL) using a spectrophotometer set at a wavelength of 600 nm. The 100 µl suspension was evenly dispersed

over Petri plates containing Mueller-Hinton agar. GO-CS-Pt-Cu, GO-CS-Pt-CuO, GO-CS-Pt-Cu<sub>2</sub>O, and GO-CS-Pt-Cu<sub>2</sub>O/Cu with GO-Cs-Pt composites were subjected to testing against *E.coli*. In comparison, GO-CS-Pt-Cu<sub>2</sub>O/Cu showed highest inhibition compared to other composites. Then the synthesized GO-CS-Pt-Cu<sub>2</sub>O/Cu composites were synthesized into increasing weight % concentration of GO-CS-Pt-Cu<sub>2</sub>O/Cu(0.5), GO-CS-Pt-Cu<sub>2</sub>O/Cu(1), GO-CS-Pt-Cu<sub>2</sub>O/Cu(1.5), GO-CS-Pt-Cu<sub>2</sub>O/Cu(2) and GO-Cs-Pt (as control) films were precisely cut into squares of 10 × 10 mm, equivalent to an area of 100 µg. These cut materials were then carefully positioned on plates colonized with the desired microorganisms, ensuring direct contact with the agar. Subsequently, the plates were placed in an incubator at 35 °C and left undisturbed for 24 h. A suspension of composites was prepared using a phosphate buffer solution with a pH of 7.2 ± 0.1. The agar medium was prepared and inoculated with *E. coli*. A sterile metal drill was used to create a well with a diameter of 8 mm in agar medium. Subsequently, an 80 µl sample designated for activity testing was introduced into the designated well, and the resulting clear zone that emerged following a 24-hour incubation period was noted. The clear zone of inhibition surrounding the film squares and wells was quantified using a calliper with a precision of 0.02 mm. The acquired data were assessed, and the standard deviation was computed.

#### 2.1.5. Degree of swelling and moisture content

The composite materials with increasing weight percentage(wt %) of Cu<sub>2</sub>O/Cu (0.5, 1, 1.5, 2) were prepared and shaped into rectangular specimens of 2 × 2 cm<sup>2</sup>. These specimens were then carefully weighed using an analytical scale to determine their starting weight, denoted as M<sub>1</sub>. Subsequently, the specimens underwent a drying process at a temperature of 70 °C within an oven for a duration of 24 h. Following this, the initial dry mass (M<sub>2</sub>) was subjected to analysis using gravimetric methods. Subsequently, the samples were dissolved in a solution of 30 mL of distilled water and allowed to incubate for 24 hours at a temperature of 25 °C. Subsequently, the specimens were subjected to a superficial drying process utilizing filter paper, followed by the determination of their weight (M<sub>3</sub>). The leftover film samples underwent a drying process at a temperature of 70 °C for a duration of 24 h within an oven. Subsequently, the final mass of the samples after complete drying was measured and recorded as M<sub>4</sub> (10, 20, 30, 40, and 50 days). The calculation of water absorption in the films was performed by Water Content (%) Eq. (2), Solubility (%) Eq. (3), Swelling Degree (%) Eq. (4):

$$WaterContent(\%) = \frac{(M_1 - M_2)}{M_1} \times 100 \quad (2)$$

$$Solubility (\%) = \frac{(M_4 - M_2)}{M_2} \times 100 \quad (3)$$

$$SwellingDegree(\%) = \frac{(M_3 - M_2)}{M_2} \times 100 \quad (4)$$

#### 2.1.6. Hydrophilicity of film surface

The surface wettability of the synthesized GO-CS-Pt-Cu<sub>2</sub>O/Cu(0.5), GO-CS-Pt-Cu<sub>2</sub>O/Cu(1), GO-CS-Pt-Cu<sub>2</sub>O/Cu(1.5), GO-CS-Pt-Cu<sub>2</sub>O/Cu(2) and GO-Cs-Pt (as control) films was assessed using a contact angle meter. A film sample, measuring 2 × 2 cm<sup>2</sup>, was affixed to a sample holder. A micro syringe was used to dispense 2 mL of distilled water onto the film surface. A digital camera was then used to capture an image of the water drop, and the contact angle between the film surface and water was calculated using a pre-installed software. Contact angle was determined by calculating the mean standard deviation of five replicate measurements of a single sample. The degree of hydrophilicity of the films was assessed by contact angle measurements using a drop shape analysis system. Deionized water, with a volume of 2 litres, was used to determine the contact angles of all films. The data reported in this study represent the median values, with a sample size of three (n = 5).

#### 2.1.7. Degradation of graphene oxide-chitosan-platinum-copper oxides/copper thin films

The GO-CS-Pt-Cu<sub>2</sub>O/Cu(0.5), GO-CS-Pt-Cu<sub>2</sub>O/Cu(1), GO-CS-Pt-Cu<sub>2</sub>O/Cu(1.5), GO-CS-Pt-Cu<sub>2</sub>O/Cu(2) and GO-Cs-Pt (as control) films samples were prepared to the specified dimensions of 8 × 8 cm<sup>2</sup> and subjected to drying at 50 °C in a vacuum oven for 6 h. The samples were then weighed to determine their initial dry weights (W<sub>i</sub>) before being buried in a bed of fresh soil. The experiments were conducted under ambient conditions. Intermittent application of water was observed, whereby it was sprayed over the soil. The weights of the buried samples were promptly measured at 10, 20, 30, 40, and

50 days. The calculation of weight loss was performed utilizing the subsequent Eq. (5):

$$\text{Biodegradation (\%)} = \frac{(W_i - W_f)}{W_i} \times 100\% \quad (5)$$

Where  $W_i$  and  $W_f$  are the initial and final dry weights of the films, respectively.

#### 2.1.8. Migration of copper from graphene oxide-chitosan-platinum-copper oxides/copper thin films s

The migration of nano Copper from GO-CS-Pt-Cu<sub>2</sub>O/Cu(0.5), GO-CS-Pt-Cu<sub>2</sub>O/Cu(1), GO-CS-Pt-Cu<sub>2</sub>O/Cu(1.5), GO-CS-Pt-Cu<sub>2</sub>O/Cu(2) thin films were studied by full immersion (double contact method), in three food simulants: Ethanol (EtOH): 100 mL of 10 % (v/v) and Acetic Acid: 100 mL of 3 % (v/v) at 32 °C for 10 days, was identified by ICP OES. Migration tests were conducted by European Plastics Regulation (EU) 10/2011. The above mentioned films were divided into smaller segments of 3 cm × 3 cm. In the migration experiment, a single piece was chosen randomly, and its weight was measured before being placed inside a glass vial with a capacity of 50 mL. To conduct the migration test at 32 °C, a 15 mL solution of acetic acid food stimulant with a concentration of 3 % (w/w) was added to the vial. The migration of Cu from the composite film to a 3 % acetic acid, water and 10 % EtOH was investigated using the methodology outlined by Inductively Coupled Plasma Optical Emission Spectrometry (ICP-OES).

### 2.2. Synthesis of magnetic-nano adsorbent

#### 2.2.1. Preparation of Graphene Oxide-Maghemite Nanoparticles and Graphene Oxide-Maghemite-Chitosan composite

Maghemite (MGH): To prepare maghemite (MGH) NPs, a mixture of FeCl<sub>2</sub> and FeCl<sub>3</sub> with a molar ratio of 1.1:2 was prepared and then treated with freshly prepared NaOH solution. The resulting black mixture was agitated for several minutes before dilution with water. To create a slurry, the mixture was rinsed multiple times with water and acidified to a pH of 2. It was then washed again before being hydrothermally aged in an ultrasonic bath at 80 °C for

30 min. Subsequently, the suspension was dialysed against 0.001 mol/L HCl and refrigerated at 4 °C.

Graphene oxide – chitosan composite: The GO-CS composite was synthesized by blending graphene oxide and chitosan solutions. Subsequently, a solution containing 3 g of chitosan was dissolved in 100 mL of 1 % acetic acid solution. Additionally, a dispersion consisting of 0.5 grammes of graphene oxide (GO) was prepared by sonication in 100 mL of Milli-Q water at room temperature. Subsequently, the two solutions were combined and sonicated for 10 min to obtain a uniform and consistent solution. Subsequently, the graphene oxide-carbon support (GO-CS) was subjected to precipitation by means of a 1 M sodium hydroxide (NaOH) solution in ethanol. Subsequently, the composite material was subjected to multiple washes with C<sub>2</sub>H<sub>5</sub>OH (Absolute, Merck, Rahway, NJ, USA), C<sub>2</sub>H<sub>3</sub>N, and Milli-Q water until a neutral pH was achieved. Prior to conducting adsorption studies, the graphene oxide-carbon structure (GO-CS) underwent a drying process at a temperature of 50 °C for a duration of 24 hours.

Graphene oxide – maghemite composite (GO-MGH): GO-MGH composites were fabricated by employing aqueous solutions containing MGH-NPs and graphene oxide. The suspensions underwent sonication for 30 s, followed by rapid blending in a 1:1 ratio of graphene oxide (GO) to multi-layer graphene hydrogel (MGH), resulting in a final MGH concentration of 5 g/L. The suspension obtained as a result, with a pH range of 5-6, was stored in a refrigerated environment to facilitate ongoing synthesis.

Graphene oxide – maghemite-chitosan composite(GO-MGH-CS): The synthesis was conducted using hydrothermally aged MGH-NPs to produce glutaraldehyde-cross-linked GO-MGH-CS I, with a weight ratio of 2.5:2.5:1 for GO:MGH:CS. Concentrated solutions of FeCl<sub>2</sub> and FeCl<sub>3</sub> were utilized in a molar ratio of 1.1:2 for the synthesis of MGH-NPs. Following the addition of freshly made sodium hydroxide (NaOH) solution, the dark mixture underwent agitation for several minutes and was subsequently diluted with water. To prepare a slurry, the combination underwent a series of rinsing steps using water, followed by acidification to achieve a pH of 2, and then underwent another round of washing. Following hydrothermal ageing in an ultrasonic bath at 80 °C for 30 min, the resulting suspension was subjected to dialysis against a solution of 0.001 mol/L hydrochloric acid (HCl). The suspension was refrigerated at 4 °C. The preparation of GO-MGH composites involved the utilisation of aqueous suspensions containing MGH-NPs and graphene oxide. The suspensions underwent sonication for 30 seconds, after

which they were promptly combined in a 1:1 ratio with a final concentration of MGH at 5 grammes per litre. The suspension obtained, with a pH range of around 5 to 6, was thereafter stored in a refrigerated environment for subsequent synthesis. The GO-MGH suspension was combined with a chitosan (CS) solution acquired from (Sigma Aldrich, Taufkirchen, Germany). The CS solution was prepared by dissolving 50 mg of chitosan in 25 mL of a 2 % (v/v) acetic acid solution. The ratio of GO-MGH to CS used in the mixture was 2:1. Subsequently, a volume of 2 mL of a 2 % glutaraldehyde solution was introduced into the mixture, followed by the adjustment of the pH to a range of 9 to 10 using a 1 mol/L sodium hydroxide (NaOH) solution. The resultant mixture was maintained at a temperature of 60 °C for 2 hours while being subjected to mechanical agitation. The composite material was subjected to magnetic separation, followed by a water wash to achieve a neutral pH. Subsequently, the material was subjected to three rounds of mixing with 100 % ethanol. Subsequently, the resultant GO-MGH-CS I composite was subjected to a drying process at a temperature of 50 °C for 16 hours under a vacuum environment.

The MGH-NPs were synthesized by introducing 25 % NH<sub>4</sub>OH to a solution containing FeCl<sub>2</sub> and FeCl<sub>3</sub> in a molar ratio of 1.5:2. The synthesis was conducted at 40 °C with continuous stirring. This process was carried out to produce GO-MGH-CS II, with a weight ratio of GO:MGH: CS of 2.5:2.5:1. The mixture was maintained within a pH range of 9-10 and subjected to vigorous agitation at 60 °C for 1 h, after which it was allowed to cool to ambient temperature. The precipitate was separated using a magnet and then subjected to numerous rinses with water. The MGH-NPs were dispersed in water before their gradual addition into an aqueous solution of graphene oxide (GO) with a concentration of 1 mg/mL. The combination underwent mechanical agitation at a temperature of 60 °C for 1 h. Subsequently, the GO-MGH composite was subjected to magnetization and rinsed three times with water.

To prepare the GO-MGH-CS II composite, a chitosan (CS) solution containing 50 mg of chitosan dissolved in 25 mL of a 2 % (v/v) acetic acid solution was added to the GO-MGH composite suspension. The pH of the mixture was modified to a range of 9-10 using a 1 mol/L NaOH solution, followed by agitation for 2 h at a temperature of 60 °C. The GO-MGH-CS II composite was obtained using a magnet, subjected to three rinses with 100 % ethanol, and subsequently washed with water until it reached pH 7. The obtained composite was subjected to vacuum drying overnight at a

temperature of 50 °C. The GO-MGH-CS III composite material was synthesized using the same procedure as that for the GO-MGH-CS II composite, maintaining a weight ratio of 1:1:1 for GO, MGH, and CS.

### 2.2.2. Characterisation

The composites that were prepared underwent characterization using various analytical instruments. X-ray diffraction analyses were conducted using a D8 X-ray diffractometer (Bruker AXS, Bremen, Germany). Fourier-transform infrared spectrometry was performed using a Vertex 70v vacuum spectrometer (Bruker Inc., Bremen, Germany) with a spectral resolution of 2 cm<sup>-1</sup>, and a KBr pellet was used for sample preparation. Raman spectra were recorded using a RAM II system (Bruker Inc., Bremen, Germany) in a 180° backscattering configuration, with a 1064 nm laser. The morphology and particle size of the produced composites were analyzed using a Tecnai G2 F20 X-TWIN transmission electron microscope (TEM) manufactured by FEI (Eindhoven, Netherlands). The TEM had a resolution ranging from 0.25 to 0.102 nm. The Mössbauer spectra were acquired at ambient temperature using a <sup>57</sup>Co (Rh) source and a Mössbauer spectrometer manufactured by Wissenschaftliche Elektronik GmbH in Starnberg, Germany. The spectra were examined using the Normos Dist program.

### 2.2.3. Batch Experiments

With an initial Eu (III) (Note: In adsorption investigations, they are employed as substitutes for the trivalent actinides) concentration of 0.01-200 mg/L, an adsorbent dosage of 1 g/L (ratio 1:1000 g/mL), a temperature of 25 °C, and a pH range of 2 to 8, adsorption tests were conducted. Using a WTW inoLab Multi Level 1 m (Weilheim, Germany) and a WTW pH electrode SenTix 41 (Weilheim, Germany) calibrated with DIN 19266 standard buffers, initial pH values were determined. <sup>152</sup>Eu was used to trace the EuCl<sub>3</sub> solution. The agitation speed was determined to be 100, 200, and 300 rpm for 5 and 24 h. The measured q<sub>e</sub> values were within the permitted margin of error. As a result, 200 rpm was used in all studies. After the required amount of time, the adsorbent was either magnetized or centrifuged at 20,000 × g for 15 min to separate it. Three sets of adsorption trials were conducted in a batch manner. Using HPGe detectors (GEM40P4-76, efficiency 42 %, resolution 1.9 keV/1.33 MeV; and the coaxial well GWL-

120-15-LB-AWT detector, resolution 2.25 keV/1.33 MeV), the amounts of Eu activity were determined by gamma spectrometry.

Eq. (6) and (7) were used to compute the adsorption capacity and removal efficiency of the GO-MGH, GO-CS, and GO-MGH-CS (I, II, III) composites, respectively:

$$q_e = \frac{(C_0 - C_e)}{m} \times V \quad (6)$$

$$R_e = \frac{(C_0 - C_e)}{C_0} \times 100\% \quad (7)$$

where  $q_e$  (mg/g) is the amount of Eu (III) adsorbed at equilibrium,  $R_e$  (%) is the removal efficiency,  $C_0$  (mg/L) is the initial concentration of Eu (III),  $C_e$  (mg/L) is the equilibrium concentration of Eu (III),  $V$  (L) is the working volume, and  $m$  (g) is the weight of the adsorbent.

#### 2.2.4. Determination of the point of zero charge

The pH at the point of zero charge was calculated using the pH drift method. Test solutions of GO-MGH-CS (I, II, and III) composites (0.05-0.1 g) were equilibrated with 50 mL of 0.01-0.1 mol/L  $\text{NaNO}_3$  under argon flow and at a temperature of  $25.0 \pm 0.1$  °C. Ten and thirty minutes after the titrant was added, the measured levels were taken. Between readings of 10 and 30 minutes, the observed voltage drifted by less than 2 mV.

#### 2.2.5. Elimination of europium, americium, and plutonium ions from aquatic environments

The GO-CS, GO-MGH, and GO-MGH-CS (I, II, III) composites were subjected to testing to evaluate their effectiveness in adsorbing Eu from natural waters. The pH of the water samples used in the testing was maintained at a consistent level of 7.8, whereas the salinity levels varied within the range of 0 to 7 psu. The study involved the analysis of water samples collected from three specific locations: the Baltic Sea ( $55^{\circ}44'53''$ – $21^{\circ}02'05''$ ), the Danes River ( $55^{\circ}42'40''$ – $21^{\circ}08'10''$ ), and the Klaipeda Strait ( $55^{\circ}43'49''$ – $21^{\circ}04'34''$ ). These samples were subjected to tracing using the radioactive isotope  $^{152}\text{Eu}$ .

The adsorbents were introduced into dialysis tubes containing a cellulose membrane with a molecular weight cut-off of 14 kDa. These tubes were then immersed in the water samples and subjected to continuous stirring for seven days. After seven days, the dialysis tubes were extracted from their respective containers. Subsequently, the water samples were subjected to gamma spectrometry to determine the levels of Eu activity.

To evaluate the appropriateness of the synthesized composites for the purpose of pre-concentrating actinides from seawater, 1-liter samples of seawater were employed. A combination of Pu (IV) and Am (III) was introduced into the water samples, consisting of isotopes  $^{238}\text{Pu}$ ,  $^{239}\text{Pu}$ ,  $^{240}\text{Pu}$ ,  $^{241}\text{Pu}$ , and  $^{241}\text{Am}$ . Subsequently, the composite materials were introduced into the mixture, which was subjected to a 1 h mixing process followed by an overnight incubation period. The composite materials were obtained using a magnet or centrifugation. Alpha spectrometry was employed to measure the Am and Pu isotopes subsequent to radiochemical separation, which was carried out using TEVA and TRU columns manufactured by Eichrom Industries. Isotopes  $^{242}\text{Pu}$  and  $^{243}\text{Am}$  were employed as tracers during the separation process.

#### 2.2.6. ANFIS development

The ANFIS architecture was implemented in MATLAB R2021, utilizing the Gaussian membership function (Gaussesmf2) in conjunction with subtractive clustering. A range of influence of 0.5, squash factor of 1.25, acceptance rate of 0.5, and rejection rate of 0.15 were set as the subtractive clustering parameters. In our study, 15 datasets were utilized for training purposes, specifically GO-MGH, GO-CS, GO-MGH-CS I, GO-MGH-CS II, and GO-MGH-CS III. Additionally, six datasets were allocated for testing, and another six datasets were designated for validation. (Table 1) shows the parameters used for ANFIS training. In order to mitigate the impact of larger-scale effects on the ANFIS architecture, the data underwent normalization Eq. (8) using before being inputted into the network. Subsequently, the network was trained with zero error tolerance and a total of 100 training cycles (epochs), each consisting of 100 iterations.

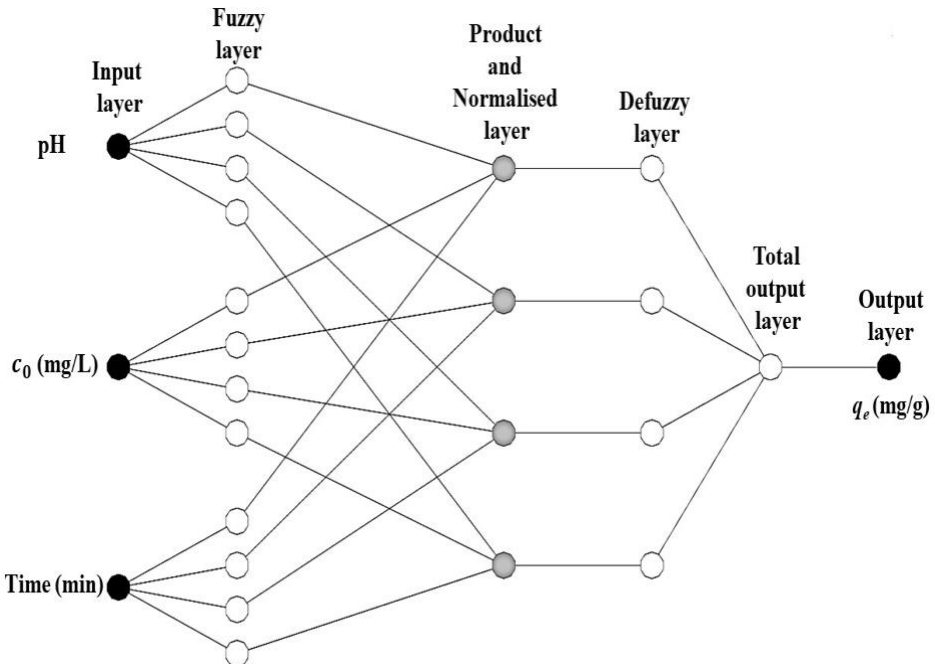


**Fig. 2** .The architecture of the Adaptive Neuro-Fuzzy Inference System used in this study.

The architecture of the Adaptive Neuro-Fuzzy Inference System has six levels (Fig. 2 ). The initial layer pertains to the input data, encompassing variables such as pH, ion concentration, and contact time. The second layer exhibits fuzzy characteristics. The third layer consists of a product and a normalized layer, which incorporates four rules for GO-MGH and GO-MGH-CS (I, II) and two rules for GO-CS. Additionally, the GO-MGH-CS III layer has five rules. The components encompassed within this framework span from the fourth to the sixth layer, namely defuzzification, total output, and output adsorption capacity. The evaluation of the network's performance was conducted by assessing the agreement between the normalized experimental and predicted data using three metrics: the mean squared error (MSE), the average relative error (ARE), and the sum of squared errors (SSE). These metrics were computed using Eq. (9), (10), and (11), respectively.

$$\hat{U}_{norm} = \frac{\bar{U} - \hat{U}_{min}}{\hat{U}_{max} - \hat{U}_{min}} \quad (8)$$

$$MSE = \frac{1}{N} \sum_{i=1}^N (\check{I}_i - \bar{I}_i)^2 \quad (9)$$

$$ARE = \frac{100}{N} \sum_{i=1}^N \left| \frac{\check{I}_i - \bar{I}_i}{\bar{I}_i} \right| \% \quad (10)$$

$$SSE = \sqrt{\frac{\sum_{i=1}^N (\check{I}_i - \bar{I}_i)^2}{N}} \quad (11)$$

Where  $\check{U}_{norm}$  represents the normalized value,  $\check{U}_{max}$  and  $\check{U}_{min}$  denote the minimum and maximum values, respectively. The variable  $\bar{U}$  represents a vector consisting of many values. The variable  $N$  represents the quantity of data points obtained through experimentation. The variable “ $\check{I}_i$ ” represents the expected output, while the variable “ $\bar{I}_i$ ” represents the experimental output.

**Table 1:** Parameters for ANFIS training

GO-MGH				
pH	$C_i$ (mg/L)	t (min)	$Q_e$ (mg/g) Exp	$Q_e$ (mg/g) Pred
2	5	1440	0.016593	0.0166
3	5	1440	0.026514	0.0173
4	5	1440	0.053613	0.0357
5	5	1440	0.059265	0.0589
6	5	1440	0.085271	0.0807
7	5	1440	0.092524	0.0926
8	5	1440	0.081405	0.0814
5	5	10	0.011982	0.0120
5	5	20	0.027691	0.0200
5	5	30	0.040068	0.0281
5	5	60	0.052184	0.0522
5	5	120	0.053489	0.1003
5	5	240	0.054794	0.1966
5	5	1440	0.059265	0.0589
5	0.01	1440	0.000000	0.0005
5	0.05	1440	0.000769	0.0010

5	0.1	1440	0.001731	0.0017
5	0.2	1440	0.003307	0.0030
5	0.3	1440	0.005177	0.0044
5	0.5	1440	0.008218	0.0070
5	1	1440	0.013085	0.0134
5	2.5	1440	0.031415	0.0318
5	5	1440	0.059265	0.0589
5	10	1440	0.112896	0.1007
5	50	1440	0.403731	0.4037
5	100	1440	0.673014	0.6730
5	200	1440	1.000000	1.0000

GO-CS				
pH	Ci (mg/L)	t (min)	Qe (mg/g) Exp	Qe (mg/g) Pred
2	5	1440	0.020383	0.0197
3	5	1440	0.026138	0.0298
4	5	1440	0.056294	0.0398
5	5	1440	0.066610	0.0499
6	5	1440	0.069315	0.0600
7	5	1440	0.080246	0.0700
8	5	1440	0.080726	0.0801
5	5	10	0.034627	0.0349
5	5	20	0.041083	0.0390
5	5	30	0.051551	0.0432
5	5	60	0.055848	0.0556
5	5	120	0.062557	0.0804
5	5	240	0.065123	0.1300
5	5	1440	0.066610	0.0499

5	0.01	1440	0.000000	0.0143
5	0.05	1440	0.000741	0.0146
5	0.1	1440	0.001667	0.0149
5	0.2	1440	0.003519	0.0157
5	0.3	1440	0.005091	0.0164
5	0.5	1440	0.008740	0.0178
5	1	1440	0.013873	0.0214
5	2.5	1440	0.034020	0.0321
5	5	1440	0.066610	0.0499
5	10	1440	0.126354	0.0856
5	50	1440	0.416559	0.3710
5	100	1440	0.703649	0.7277
5	200	1440	1.000000	1.0002

GO-Mg-Cs I				
pH	C <sub>i</sub> (mg/L)	t (min)	Q <sub>e</sub> (mg/g) Exp	Q <sub>e</sub> (mg/g) Pred
2	5	1440	0.021975	0.0220
3	5	1440	0.029983	-0.0358
4	5	1440	0.104037	0.0631
5	5	1440	0.110142	0.1096
6	5	1440	0.119769	0.0952
7	5	1440	0.171320	0.1713
8	5	1440	0.171152	0.1712
5	5	10	0.051882	0.0519
5	5	20	0.069583	0.0622
5	5	30	0.070748	0.0725
5	5	60	0.103515	0.1035

5	5	120	0.105761	0.1653
5	5	240	0.107942	0.2890
5	5	1440	0.110142	0.1096
5	0.01	1440	0.000000	0.0003
5	0.05	1440	0.001357	0.0012
5	0.1	1440	0.002713	0.0024
5	0.2	1440	0.005049	0.0047
5	0.3	1440	0.007682	0.0069
5	0.5	1440	0.010553	0.0115
5	1	1440	0.022772	0.0228
5	2.5	1440	0.056334	0.0562
5	5	1440	0.110142	0.1096
5	10	1440	0.208474	0.2060
5	50	1440	0.479792	0.4793
5	100	1440	0.719888	0.7203
5	200	1440	1.000000	0.9999

GO-Mg-Cs II				
pH	Ci (mg/L)	t (min)	Qe (mg/g) Exp	Qe (mg/g) Pred
2	5	1440	0.012245	0.0122
3	5	1440	0.019741	0.0221
4	5	1440	0.036533	0.0320
5	5	1440	0.041716	0.0418
6	5	1440	0.042198	0.0482
7	5	1440	0.04418	0.0442
8	5	1440	0.039937	0.0399
5	5	10	0.022962	0.0230

5	5	20	0.025063	0.0264
5	5	30	0.025079	0.0299
5	5	60	0.040246	0.0402
5	5	120	0.041689	0.0609
5	5	240	0.041712	0.1024
5	5	1440	0.041716	0.0418
5	0.01	1440	0	0.0002
5	0.05	1440	0.000379	0.0005
5	0.1	1440	0.000838	0.0010
5	0.2	1440	0.001732	0.0018
5	0.3	1440	0.002613	0.0026
5	0.5	1440	0.004319	0.0043
5	1	1440	0.008598	0.0085
5	2.5	1440	0.021419	0.0210
5	5	1440	0.041716	0.0418
5	10	1440	0.079256	0.0830
5	50	1440	0.354306	0.3543
5	100	1440	0.631032	0.6310
5	200	1440	1	1.0000

GO-Mg-Cs III				
pH	Ci (mg/L)	t (min)	Qe (mg/g) Exp	Qe (mg/g) Pred
2	5	1440	0.01229	0.0123
3	5	1440	0.022869	0.0514
4	5	1440	0.032075	0.0716
5	5	1440	0.037027	0.0370
6	5	1440	0.037391	0.0300
7	5	1440	0.038618	0.0386
8	5	1440	0.037148	0.0371
5	5	10	0.011118	0.0111
5	5	20	0.024338	0.0149
5	5	30	0.019943	0.0186
5	5	60	0.029928	0.0299
5	5	120	0.033518	0.0524
5	5	240	0.035525	0.0975
5	5	1440	0.037026	0.0370
5	0.5	1440	0	0.0000
5	1	1440	0.004045	0.0039
5	2.5	1440	0.016915	0.0161
5	5	1440	0.037026	0.0370
5	10	1440	0.072013	0.0720
5	50	1440	0.339967	0.0773
5	100	1440	0.60595	0.6268
5	200	1440	1	1.0000

### 3. RESULTS AND DISCUSSION

#### 3.1. Characterization of composites for food packaging

##### 3.1.1. XRD

The XRD pattern of the GO-CS-Pt composite showed diffraction peaks at  $2\theta = 10.6^\circ$ ,  $26.2^\circ$ ,  $26.45^\circ$ , and  $40.3^\circ$ , corresponding to the characteristic peaks of GO, chitosan, and platinum, respectively (S. M. Hosseini et al., 2022; A. S. K. Kumar & Jiang, 2016; L. Liu et al., 2012; Rao et al., 2016; Rong et al., 2007). The diffracted peaks of the (111) and (200) planes at  $2\theta = 36.26^\circ$  and  $43.26^\circ$  in the GO-CS-Pt-Cu composite are assigned to the Cu monoclinic structure (Emiru & Ayele, 2017; Figiela et al., 2018; S. B. Khan et al., 2019). The diffracted peak (111) at  $2\theta = 42.1^\circ$  indicates the presence of Pt (Qiu et al., 2011). The crystallite size of GO in this composite is 3.5 nm, while the crystallite size of Cu and Pt is 25.1 nm and 3.6 nm, respectively. The diffracted peaks of the (111), (-111), (202), (111), and (202) planes of the GO-CS-Pt-CuO composite correspond to CuO at  $2\theta = 35.32^\circ$ ,  $38.66^\circ$ ,  $48.56^\circ$ , and The XRD patterns of the synthesized composites are shown in Fig. 3. The XRD analysis diffraction patterns of the GO nanostructures revealed is observed by a characteristic peak at  $10.2^\circ$  indicating the plane (001) at  $2\theta = 10.2^\circ$ . The broad rise at  $2\theta = 38^\circ$  suggests that the typical layered structure of graphene oxide has been changed after the addition of  $43.27^\circ$ , respectively (Abdolsattari et al., 2022). The average crystallite size of the CuO nanoparticles was 11.9 nm. The XRD diffractogram of the GO-CS-Pt-Cu<sub>2</sub>O film shows that the (110), (111), (200), and (220) peaks at  $2\theta =$  correspond to Cu<sub>2</sub>O positioned at  $29.38^\circ$ ,  $36.48^\circ$ ,  $42.44^\circ$ , and  $61.44^\circ$ , respectively, correspond to Cu<sub>2</sub>O (Figiel et al., 2018; Kalubowila et al., 2021). The calculated crystal size of Cu<sub>2</sub>O was 16.9 nm. The XRD diffraction spectrum of the GO-CS-Pt-Cu<sub>2</sub>O/Cu composite reveals that the diffraction peaks of the (110), (111) plane and (111) planes were assigned to Cu<sub>2</sub>O at  $2\theta = 29.36^\circ$ ,  $36.54^\circ$  and the peak of the (020) plane was assigned to Cu at  $2\theta =$  positioned at  $50.36^\circ$ . The peaks around  $35.1^\circ$ ,  $38.6^\circ$ , and  $49.0^\circ$  could be attributed to the (111), (111), and (020) planes, respectively, which are assigned to the phase of copper oxide nanoparticles (JCPDS File Card No. 05e661)(Kalubowila et al., 2021; A. Khan et al., 2016).

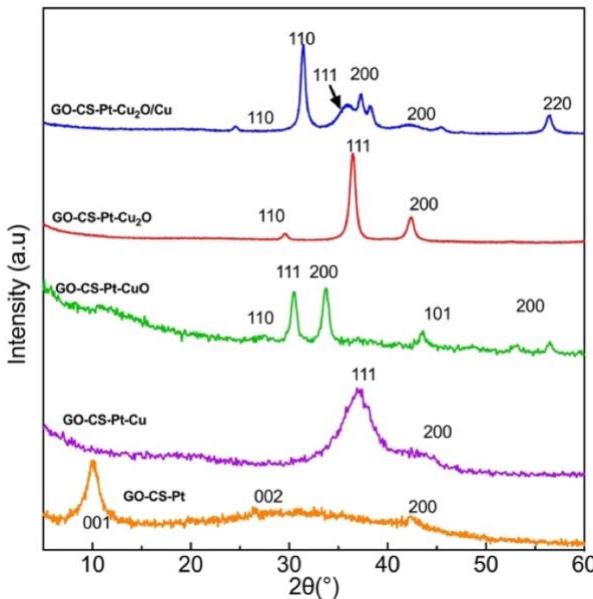


**Fig. 3.** XRD pattern of GO-CS-Pt-Cu, GO-CS-Pt-CuO, GO-CS-Pt-Cu<sub>2</sub>O, and GO-CS-Pt-Cu<sub>2</sub>O/Cu and GO-CS-Pt Composites.

### 3.1.2 FTIR

Blended films of GO-CS-Pt-Cu, GO-CS-Pt-CuO, GO-CS-Pt-Cu<sub>2</sub>O, GO-CS-Pt-Cu<sub>2</sub>O/Cu with Chitosan were developed to combine the film-forming properties of chitosan, superior barrier properties of graphene oxide, and antibacterial properties of copper. The FTIR spectra of the graphene oxide-chitosan-platinum (GO-CS-Pt) composites exhibited characteristic absorption peaks at 3448, and 1051 cm<sup>-1</sup>, corresponding to  $-\text{NH}_2$ , and C=O stretching vibrations of chitosan (X. Yang et al., 2010; P. T. Yin et al., 2015), whereas bands at 1594 cm<sup>-1</sup> represents graphene oxide (Zuo et al., 2013). The stretching between 3411 and 3248 cm<sup>-1</sup> shows a homogeneous stretching between 3411 and 3248 cm<sup>-1</sup> shows a homogeneous stretching between GO and CS (S. Kumar & Koh, 2014). Also, the peaks at 1636, 1534, 1383, and 1107 cm<sup>-1</sup> were attributed to Amide I band, Amide II band, bending vibration of the amino group, and C–O–C stretching of chitosan (Bai et al., 2016; Sharififard et al., 2013; Yan et al., 2021b). The GO-CS-Pt-Cu composite displayed additional peaks at 618 cm<sup>-1</sup>, 1328 cm<sup>-1</sup>, 1623 cm<sup>-1</sup>, 1450 cm<sup>-1</sup>, 1072 cm<sup>-1</sup> which were associated with the presence of single-bonded carbon with halogen stretching vibrations and C=C stretching vibrations, for asymmetric stretching COO, N-H bending and C-H bond

stretching respectively (Betancourt-Galindo et al., 2014; Das et al., 2020; Emadi et al., 2017).

The GO-CS-Pt-CuO exhibited distinct absorption bands at  $506\text{ cm}^{-1}$ ,  $1041\text{ cm}^{-1}$ , and  $1118\text{ cm}^{-1}$ , which were assigned to the vibrational bending mode of Cu-O, C-O stretching, and C-N stretching of the quaternary ammonium group of graphene oxide, respectively. The GO-CS-Pt-CuO composite, additionally displayed absorption bands at  $1416\text{ cm}^{-1}$  and  $1558\text{ cm}^{-1}$ , which were ascribed to O-H bending and N-O stretching bands, respectively. Furthermore, bands at  $474\text{ cm}^{-1}$  and  $545\text{ cm}^{-1}$  were assigned to the vibrational bending mode of Cu-O (Jayaramudu et al., 2019; Zhong et al., 2017). The FTIR spectra of GO-CS-Pt-Cu<sub>2</sub>O, showed peaks between  $1450\text{ cm}^{-1}$  and  $1300\text{ cm}^{-1}$  due to C-H bending vibrations,  $1070\text{ cm}^{-1}$  due to C-N stretching vibration, the characteristic peaks of Cu<sub>2</sub>O at  $720\text{ cm}^{-1}$ ,  $618\text{ cm}^{-1}$  are also observed (Guo et al., 2019). Moreover, additional weak absorption bands at  $3123\text{ cm}^{-1}$ ,  $3268\text{ cm}^{-1}$ ,  $3478\text{ cm}^{-1}$ , and  $3572\text{ cm}^{-1}$ , which could be attributed to C-H stretching vibrations. Also, in the GO-CS-Pt-Cu<sub>2</sub>O/Cu composite, an absorption peak at  $1719\text{ cm}^{-1}$  was detected, indicating the C=O stretching of the COOH group (Santos-Cruz et al., 2017) and peaks at  $1656\text{ cm}^{-1}$ ,  $1452\text{ cm}^{-1}$  and  $1398\text{ cm}^{-1}$  are attributed to C=C stretching, C=C aromatic ring stretching and C-OH stretching vibrations (Mohamed, 2020). It is noteworthy that the absorption below  $1000\text{ cm}^{-1}$  resulting from interatomic vibrations is typically exhibited by metal oxides. Additionally, a peak at  $1622\text{ cm}^{-1}$  was observed consistently across all composite films, reflecting the characteristic C=C stretching vibration (Sutradhar et al., 2014).

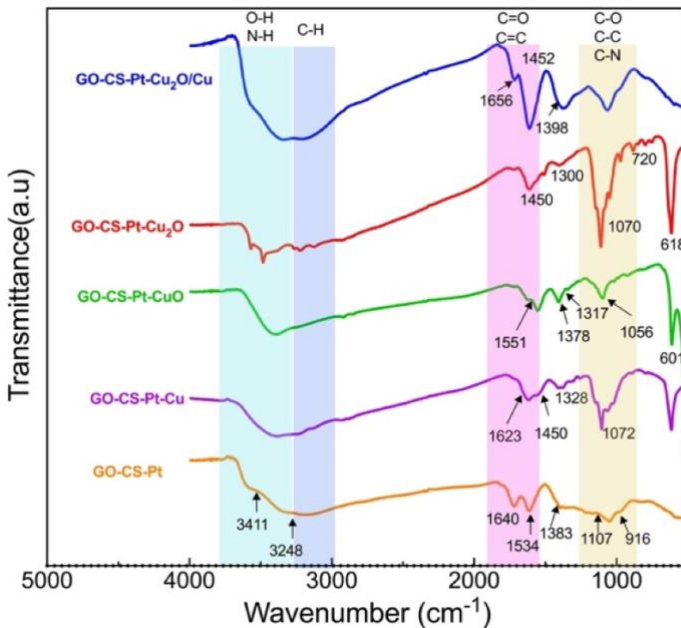


**Fig. 4.** FTIR pattern of. GO-CS-Pt-Cu, GO-CS-Pt-CuO, GO-CS-Pt-Cu<sub>2</sub>O, and GO-CS-Pt-Cu<sub>2</sub>O/Cu and GO-CS-Pt nanocomposite films.

### 3.1.3. Ultraviolet shielding efficiency of nanocomposite films

Food packaging materials must retain their transparency if this is a desirable property to ensure the good appearance of the packaged food, which may affect consumer acceptance of the product. Ultraviolet (UV) light is one of the most common oxidation triggers that can lead to oxidation of lipids in food systems. Therefore, it is important for food manufacturers to develop methods to improve the barrier properties of food films against UV light. The optical transmittance (%) of the prepared GO-CS-Pt-Cu, GO-CS-Pt-CuO, GO-CS-Pt-Cu<sub>2</sub>O, and GO-CS-Pt-Cu<sub>2</sub>O/Cu films were measured at the preferred wavelength (200–600 nm) and the results are displayed in Fig. 5. The light transmittance of all the synthesized films from UVC (200–280) nm is under 1 %, indicating that the ultraviolet at the wavelength of 200 to 280 nm can hardly penetrate through all synthesized films. GO-CS-Pt-Cu<sub>2</sub>O/Cu displayed the lowest UV light transmission among the studied nanocomposite films. The films exhibited a notable decrease in percent transmittance for both UV and visible lights following the involvement of copper and copper oxide

nanoparticles on to the thin films. The transmittance (%) of UV and visible light was measured using a spectrophotometer and given in Table 2. The presence of Cu nanoparticles led to a significant reduction in UV transmittance, which dropped to 37.5 %, while visible light was still transmitted. This demonstrates the promising ability of Cu nanoparticles to provide moderate UV protection. Nevertheless, the presence of CuO nanoparticles led to a remarkable improvement in visible light transmittance with a measured transmittance of 64.7 %. This indicates that the nanoparticles not only absorb UV light but also scatter light. On the other hand, Cu<sub>2</sub>O showed effective UV protection with a transmission rate of 47.4 %, with even higher visible light transmittance.

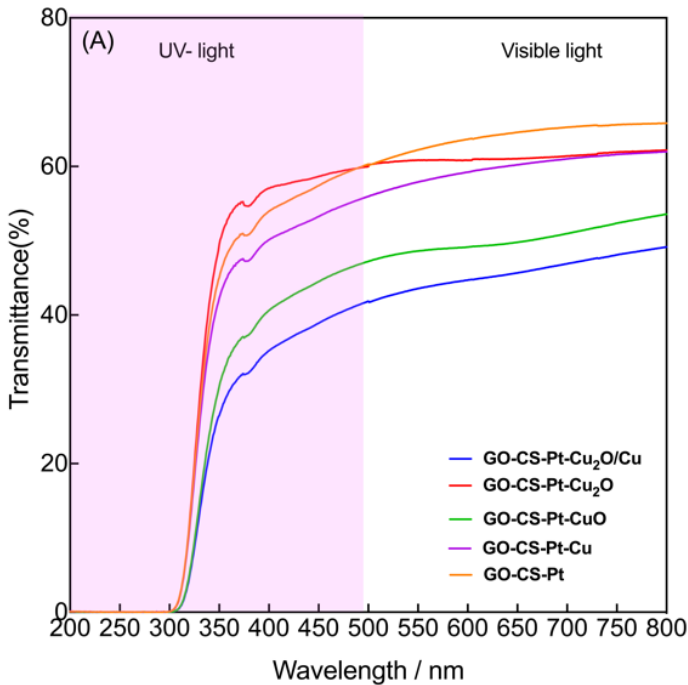


**Fig. 5.** UV-vis transmission spectra of GO-CS-Pt-Cu, GO-CS-Pt-CuO, GO-CS-Pt-Cu<sub>2</sub>O, and GO-CS-Pt-Cu<sub>2</sub>O/Cu.

The GO-CS-Pt-Cu film exhibited an exceptionally low UV transmittance of 32.4 %, due to the synergistic interactions between Cu<sub>2</sub>O and Cu nanoparticles. This synergy provides high protection against UV-B radiation while still allowing a considerable amount of visible.

**Table 2.** Transmittance Percentage of the GO-CS-Pt-Cu, GO-CS-Pt-CuO, GO-CS-Pt-Cu<sub>2</sub>O, and GO-CS-Pt-Cu<sub>2</sub>O/Cu.

Thin films	Transmission at 380 (%)	Transmission at 660 (%)
GO-Cs-Pt	54.8 ± 1.6	61.1± 1.8
GO-Cs-Pt-Cu	37.5 ± 1.3	49.9 ± 1.7
GO-Cs-Pt-CuO	50.9 ± 2.2	64.7± 2.4
GO-Cs-Pt-Cu <sub>2</sub> O	47.4 ± 2.6	61.0 ± 2.8
GO-Cs-Pt-Cu <sub>2</sub> O/Cu	32.4 ± 2.1	45.9 ±2.3

### 3.1.4. Antibacterial Study

Copper-based nanofillers in food packaging suppress the growth of pathogens, as antimicrobial tests have shown. This is attributed to their strong and far-reaching antibacterial properties. The use of nanofillers in the packaging matrix successfully prevented the growth of microorganisms in both packaged and freshly sliced food samples. The study investigated the bactericidal properties of chitosan films, copper particles and GO particles on Gram-negative *Escherichia coli* bacteria, taking into account their antibacterial properties. The antimicrobial behaviour of synthesized GO-CS-Pt(control), Cu, CuO, Cu<sub>2</sub>O, Cu<sub>2</sub>O/Cu nanoparticles and GO-CS-Pt-Cu, GO-CS-Pt-CuO, GO-CS-Pt-Cu<sub>2</sub>O, and GO-CS-Pt-Cu<sub>2</sub>O/Cu nanocomposites thin films against *E.coli* are reported in the results presented in Fig.6. (A) and Fig.6.(B). The inhibitory effect of the nanoparticles was evaluated by measuring the size of the inhibition zone formed after 48 hours at a temperature of 37 °C. The entire experiment was conducted within the confines of the incubation chamber. Fig. 6 (A) shows the antimicrobial activity against *E. coli*. Bacteria, with inhibition zone (mm) values of 5, 4, 6, 4, and 1 mm for Cu, CuO, Cu<sub>2</sub>O, Cu<sub>2</sub>O/Cu, and GO-Cs-Pt nanoparticles, respectively. Fig.6. (B) shows the antimicrobial activity of nanocomposite thin films against *E. coli*. Bacteria with the inhibition zone (mm) values of 1.0 mm for GO-CS-Pt-Cu, 2 mm for GO-CS-Pt-CuO, 9 mm for GO-CS-Pt-Cu<sub>2</sub>O and 11.3 mm for GO-CS-Pt-Cu<sub>2</sub>O/Cu. These results suggest that nanocomposite films with Cu<sub>2</sub>O/Cu nanoparticles show efficient antibacterial activity against *E. coli*.

CuO NPs can produce more ROS than Cu<sub>2</sub>O NPs as they can generate ROS through Haber-Weiss and Fenton processes, whereas Cu<sub>2</sub>O NPs can only generate ROS through Fenton reactions. In terms of the possible mode of action for CuO, the electron transfer between the negatively charged bacteria and the copper NPs is one of the effective mechanisms that cause the bacterial membrane rupturing and exerting antibacterial activity. Whereas the antibacterial action of GO-CS-Pt-Copper may be ascribed to the liberation of Cu<sup>1+</sup> and Cu<sup>0</sup> ions into the bacterial medium, subsequently engaging with the bacterial genome and proteins, resulting in the inhibition of reactive oxygen species release, eventually resulting in bacterial extinction (Gopinath et al., 2024; Ren et al., 2009; W. Zhang et al., 2023). In contrast, the GO-CS-Pt-Cu<sub>2</sub>O/Cu thin films with Cu<sub>2</sub>O/Cu showed higher value of inhibition, while other hybrid films with different oxidation states of copper also showed antibacterial activity. Considering this, we synthesized GO-CS-Pt-Cu<sub>2</sub>O/Cu nanocomposite-based chitosan thin films, with increasing weight % (W/W) concentrations of (0.5, 1, 1.5, 2) Cu<sub>2</sub>O/Cu into chitosan matrix to determine the most favourable concentration for use in food packaging.

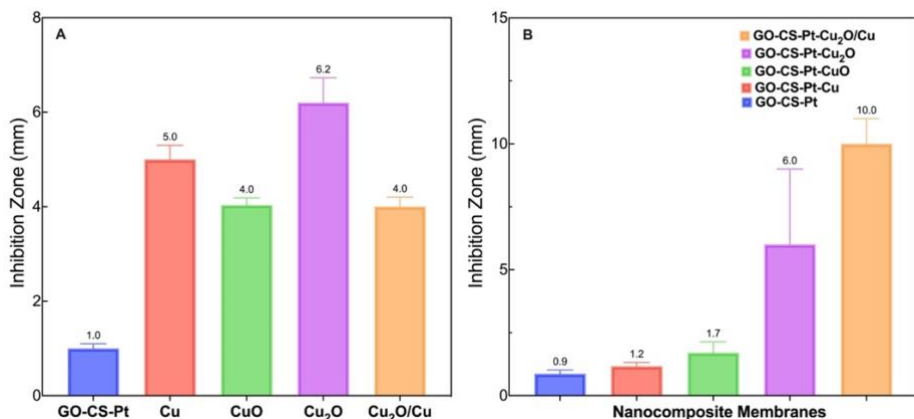


**Fig. 6.** Antibacterial activity of investigated composites and films (A) GO-CS-Pt(control), Cu, CuO, Cu<sub>2</sub>O, Cu<sub>2</sub>O/Cu nanoparticles (B) GO-CS-Pt-Cu, GO-CS-Pt-CuO, GO-CS-Pt-Cu<sub>2</sub>O, and GO-CS-Pt-Cu<sub>2</sub>O/Cu nanocomposite films.

### 3.1.5. Hydrodynamic properties

The water resistance characteristics of GO-CS-Pt-Cu<sub>2</sub>O/Cu(0.5), GO-CS-Pt-Cu<sub>2</sub>O/Cu(1), GO-CS-Pt-Cu<sub>2</sub>O/Cu(1.5), GO-CS-Pt-Cu<sub>2</sub>O/Cu(2) Composite-based chitosan thin films are crucial for preserving food. Therefore, the water solubility (WS) and the ability of the film samples not to

dissolve were evaluated in the solubility and swelling tests. The water solubility of the films is directly related to their ability to dissolve naturally and serves as a measure of their resistance to water.

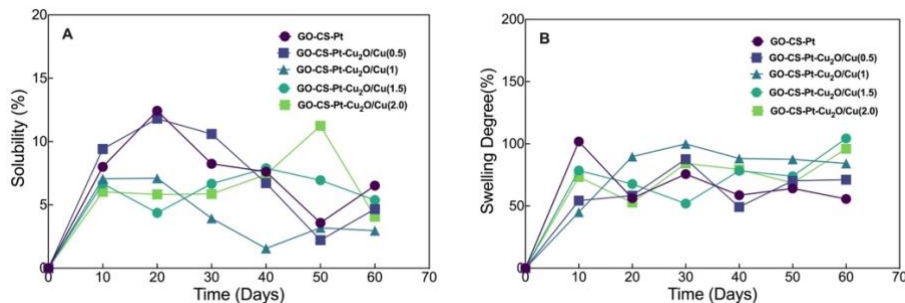


**Fig. 7.**(A) Solubility and (B) Swelling degree of the GO-CS-Pt-Cu<sub>2</sub>O/Cu(0.5), GO-CS-Pt-Cu<sub>2</sub>O/Cu(1), GO-CS-Pt-Cu<sub>2</sub>O/Cu(1.5), GO-CS-Pt-Cu<sub>2</sub>O/Cu(2). The values are represented as a mean  $\pm$  standard deviation.

Films with a high-water solubility are not suitable for food packaging, as they must have both a high-water resistance and a high moisture content. The water solubility (WS) parameter measures the degree to which a film sample resists water. An increased or optimal solubility of films can promote degradation, while a lower solubility is advantageous for storage (Zheng et al., 2014).

Over a period of 60 days, the GO-CS-Pt thin films showed the highest solubility, which decreased from 8 % to 6.5 % from day 10. While the solubility of all other thin films increased after 10 days, the solubility of the GO-CS-Pt-Cu<sub>2</sub>O/Cu (1) thin films decreased over time, reaching a lower solubility of 2.96 %. The GO-CS-Pt-Cu<sub>2</sub>O/Cu (0.5), GO-CS-Pt-Cu<sub>2</sub>O/Cu (1.5) and GO-CS-Pt-Cu<sub>2</sub>O/Cu (2) thin films showed solubilities of 4.6 %, 5.3 % and 4 %, respectively, after 60 days, as shown in Fig. 7 (A).

The degree of swelling of the food packaging material can affect the permeability to gasses such as oxygen and carbon dioxide as well as the water vapour permeability (MVTR). If the packaging material swells significantly, there is a possibility that its permeability to moisture increases, which can cause the food in the packaging to spoil or rot (Suppakul et al., 2003). Research suggests that the incorporation of graphene oxide can reduce the degree of swelling of chitosan films (Kim et al., 2020). The reduction in the degree of swelling of the chitosan-based film after crosslinking has also been

documented (Liang et al., 2019). Shariatinia & Fazli, (2015) found out that addition of  $\text{Fe}_3\text{O}_4$  nanoparticles onto the chitosan-starch matrix films decreased the swelling of the thin film in acidic media. The swelling characteristics have a significant impact on the permeability to oxygen, carbon dioxide and water vapour (MVTR), which are key factors for the packaging material. Fig. 7(B) shows that the swelling property measured over a period of 60 days ranged from 79.0 % to 96.3 %. It was observed that the swelling property decreased with increasing concentration of  $\text{Cu}_2\text{O}/\text{Cu}$  (Susilowati et al., 2019). This may be due to copper nanoparticles contributing to the binding of water molecules. The formation of coordination bonds between the functional groups of chitosan and GO-CS-Pt- $\text{Cu}_2\text{O}/\text{Cu}$  NPs resulted in a decrease in the swelling ratio capacity of the nanocomposite films.

The evaluation of surface wettability is a critical attribute of composite films, especially in the context of their use in food packaging. Vasi et al., (2022) conducted a study that demonstrated the ability to alter the wettability of PET thin films through multiple treatment methods. This finding holds potential implications for the interactions between packaging materials and food. Measurements of the water contact angle are crucial for assessing the properties of food packaging materials. They provide information on whether the surface is hydrophilic or hydrophobic, with hydrophilic surfaces preventing the condensation of water and thus minimizing the potential for food contamination.

Fig. 8 shows that the hydrophobicity of the thin films decreases with increasing concentration of nanoparticles. The GO-CS-Pt thin film exhibited the highest hydrophobicity ( $87.3^\circ$ ) compared to the other composites, indicating that the concentration of  $\text{Cu}_2\text{O}/\text{Cu}$  increases with increasing film thickness, resulting in lower hydrophobicity. The hydrophobicity of the GO-CS-Pt- $\text{Cu}_2\text{O}/\text{Cu}(1)$  thin film was only slightly reduced to  $74.85^\circ$  when higher concentrations of nanoparticles were present in the chitosan matrix. The incorporation of graphene oxide increases the degree of crosslinking of the chitosan films and their interaction with water. The improved surface roughness of the chitosan matrix can be attributed to the incorporation of the nanocomposite. Moreover, the addition of AgNPs and activated nanocarbon increased the hydrophilicity of the chitosan films. On the other hand, Alghuwainem et al. (2022) observed that chitosan films with nanoparticles can exhibit altered surface roughness and different hydrophilic properties, which can affect the contact angle of the thin films.

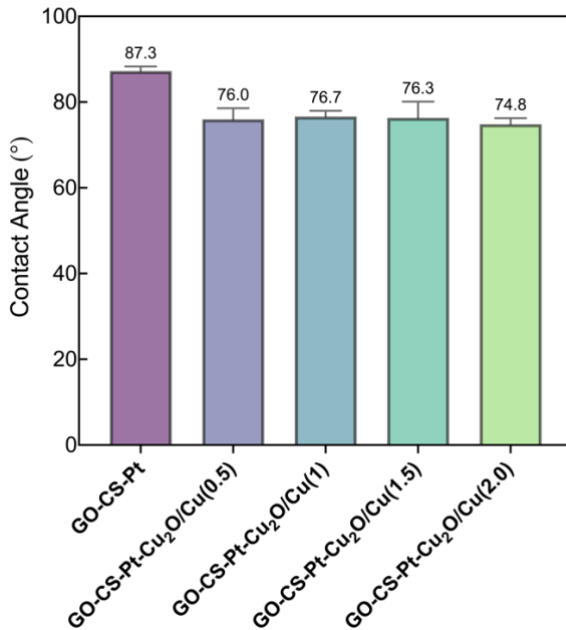


**Fig. 8.** Contact angle measurements of the GO-CS-Pt-Cu<sub>2</sub>O/Cu(0.5), GO-CS-Pt-Cu<sub>2</sub>O/Cu(1), GO-CS-Pt-Cu<sub>2</sub>O/Cu(1.5), GO-CS-Pt-Cu<sub>2</sub>O/Cu(2) composites in chitosan thin films .

In addition, the surface energy of nanoparticles influences the contact angle, whereby nanoparticles with higher surface energy have a greater affinity for liquids and reduce the contact angle. The introduction of nanoparticles can alter the surface chemistry of the substrate and influence the intermolecular interactions between the liquid and solid surfaces, which can lead to a reduction in the contact angle

### 3.1.6. Degradability in soil

Polymeric materials change their structure, morphology and properties considerably due to numerous environmental influences such as microorganisms, humidity, temperature, pH value of the surrounding medium (e.g., soil) and other influencing elements. The incorporation of fillers into the film can control biodegradability and improve durability by promoting the development of a dense structure and/or exhibiting antibacterial properties. Biodegradation in the soil can occur by two main mechanisms: either by photodegradation or by the microbial activity present in the soil. The subsequent phase comprises enzymatic and other excreted degradation

processes that lead to weight loss and decomposition of the film sample. The biodegradability of the tested film was determined by analyzing the changes in its weight and surface microstructure. In one study, the biodegradation of chitosan-coated phosphorylated starch films in a soil environment was investigated. The results showed that chitosan-coated phosphorylated films exhibited a high degree of degradation, with near destruction occurring within three months (Merino & A. Alvarez, 2019). The biodegradation of chitosan-based biopolymer films supplemented with the polyphenol extract of *Quercus* was tested in different soil types (Oberlinter et al., 2021). The results showed that the chitosan films dissolved in all tested soil samples within less than three days. The hydrophilic property of chitosan-graphene oxide nanocomposites has the potential to play an important role in soil degradation. The hydrophilic properties of chitosan-graphene oxide nanocomposites can also improve their interaction with soil particles, allowing better dispersion and diffusion of the nanocomposite material within the soil matrix. It was also suggested that swelling and accelerated film biodegradation could result from water diffusing into the polymer matrix.

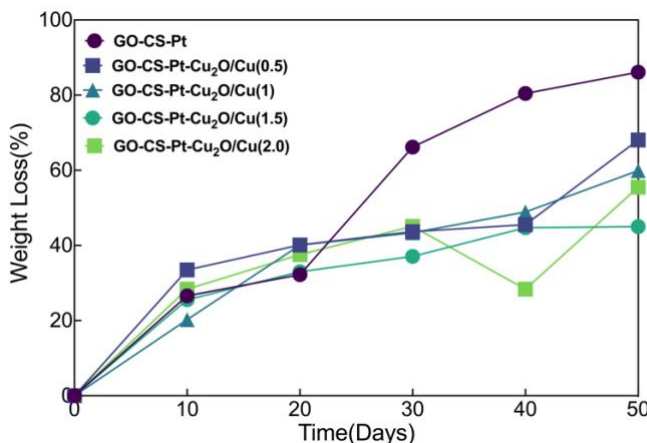


**Fig. 9.** The GO-CS-Pt-Cu<sub>2</sub>O/Cu (0.5), GO-CS-Pt-Cu<sub>2</sub>O/Cu(1), GO-CS-Pt-Cu<sub>2</sub>O/Cu(1.5), GO-CS-Pt-Cu<sub>2</sub>O/Cu(2) composites in chitosan thin films for 50 days

The degradation behaviour of chitosan thin films in the soil can be influenced by the incorporation of metal. Thin metal films, such as those consisting of copper, are used in numerous applications due to their special properties. However, the interface between thin metal films and soil can cause corrosion and decay over a long period of time (H. Zhang et al., 2001). The

soil was maintained at ambient temperature, a moisture content of 45 % and a pH of 6. The GO-CS-Pt composite film exhibited the highest biodegradability of 86.12 %, as shown in Fig. 9., which may be due to the antimicrobial activity of the soil. Pure chitosan films, on the other hand, are completely degraded, as previously reported (Oberlintner et al., 2021; Vasile et al., 2018). The biodegradability of the GO-CS-Pt control composite film was the highest at 86.12 %. This could be attributed to the antibacterial properties of the soil. The GO-CS-Pt-Cu<sub>2</sub>O/Cu(1.5) films exhibited the highest degree of biodegradability. As the concentration of Cu<sub>2</sub>O/Cu in the composite increased, the percentage weight loss decreased in the following order: 68.07 %, 59.9 %, 55.55 % and 45.0 % for Cu<sub>2</sub>O/Cu (0.5), Cu<sub>2</sub>O/Cu (1), Cu<sub>2</sub>O/Cu (1.5) and Cu<sub>2</sub>O/Cu (2), respectively. This result was in accordance with (Ilyas et al., 2018) This phenomenon can be attributed to the enhanced intermolecular interaction, which is favoured by the increasing concentration of nanofillers. The present research results indicate that sufficient dispersibility of the nanofillers in the matrix has the potential to improve the biodegradability of the material and thus represents a promising element for improved durability (Cheng & Grest, 2016; Hwang et al., 2012; Tabassum et al., 2023).

### 3.1.7. Surface characterisation

The energy dispersive X-ray analysis of GO-CS-Pt-Cu<sub>2</sub>O/Cu(0.5), GO-CS-Pt-Cu<sub>2</sub>O/Cu(1), GO-CS-Pt-Cu<sub>2</sub>O/Cu(1.5), GO-CS-Pt-Cu<sub>2</sub>O/Cu(2) showed an optical absorption band peak at approximately 0.8-1.0 keV. The results (Fig. 10. (a-d)) show the typical absorption of metallic Cu<sub>2</sub>O nanocrystallites. The percentage mass fraction of Cu in the EDX thin films increases with increasing Cu<sub>2</sub>O weight concentration (w/w) in the synthesized thin films. The elemental mapping study performed on the Cu<sub>2</sub>O nanoparticles showed a significant dispersion of metallic Cu<sub>2</sub>O within the scanning electron microscopy image of the copper nanoparticles present in the films. All the element mapping images (Fig. 11.(A-D)) show the presence of copper in the thin films, although not very bright, indicating that the copper nanoparticles are present inside the thin films and not on the outer surface.

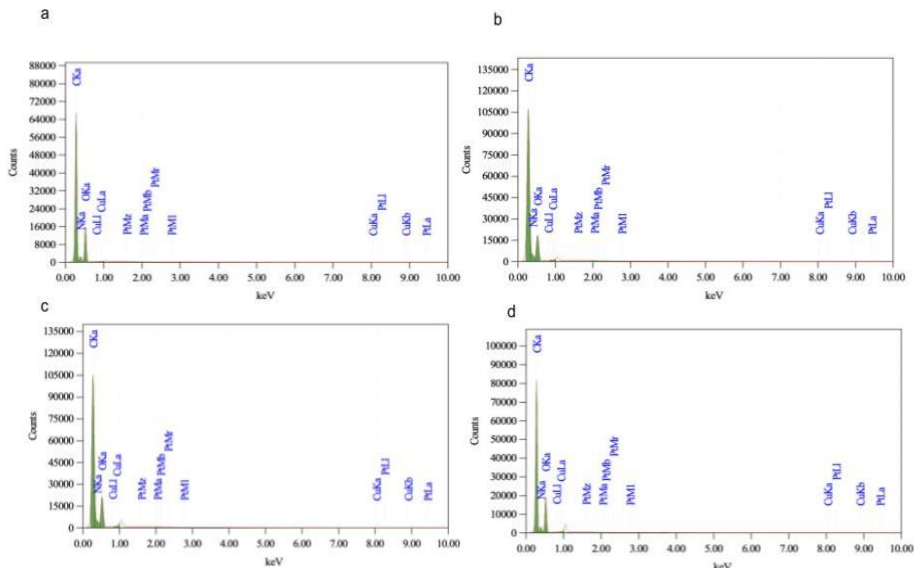


**Fig. 10.** EDX Spectra of films with increasing concentration of Cu<sub>2</sub>O/Cu, (a) GO-CS-Pt-Cu<sub>2</sub>O/Cu(0.5), (b) GO-CS-Pt-Cu<sub>2</sub>O/Cu(1), (c) GO-CS-Pt-Cu<sub>2</sub>O/Cu(1.5),(d) GO-CS-Pt-Cu<sub>2</sub>O/Cu(2).

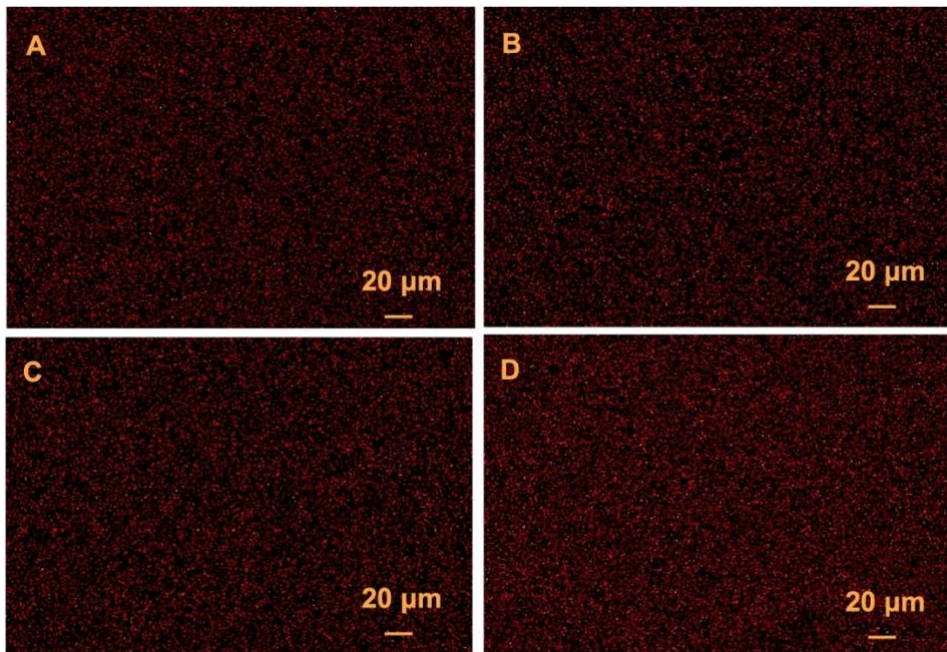


**Fig. 11.** Elemental Mapping with the presence of Copper in (a) GO-CS-Pt-Cu<sub>2</sub>O/Cu(0.5), (b) GO-CS-Pt-Cu<sub>2</sub>O/Cu(1), (c) GO-CS-Pt-Cu<sub>2</sub>O/Cu(1.5),(d) GO-CS-Pt-Cu<sub>2</sub>O/Cu(2) nano-composite thin films.

### 3.1.8. AFM and FE-SEM

GO-CS-Pt-Cu<sub>2</sub>O/Cu(0.5), GO-CS-Pt-Cu<sub>2</sub>O/Cu(1), GO-CS-Pt-Cu<sub>2</sub>O/Cu(1.5), GO-CS-Pt-Cu<sub>2</sub>O/Cu(2) films were subsequently examined by atomic force microscopy (AFM) in order to determine the dimensions of the GO-CS-Pt-Cu<sub>2</sub>O/Cu nanoparticles and the morphology of the resulting nanocomposite thin film. AFM microscopy illustrates the integration of GO-CS-Pt-Cu<sub>2</sub>O/Cu into the chitosan layer, which exhibits a spherical morphology as shown in Fig. 12. (A-D). Furthermore, AFM analysis revealed that the particles exhibited no signs of agglomeration within the Chitosan matrix. While the field electron scanning electron microscopy (FE-SEM) images (Fig. 13. A-D) showed a smooth surface for all increasing concentrations of GO-CS-Pt-Cu<sub>2</sub>O/Cu incorporated chitosan films, AFM showed increasing surface roughness with increasing weight concentration of Cu<sub>2</sub>O/Cu in the chitosan films.

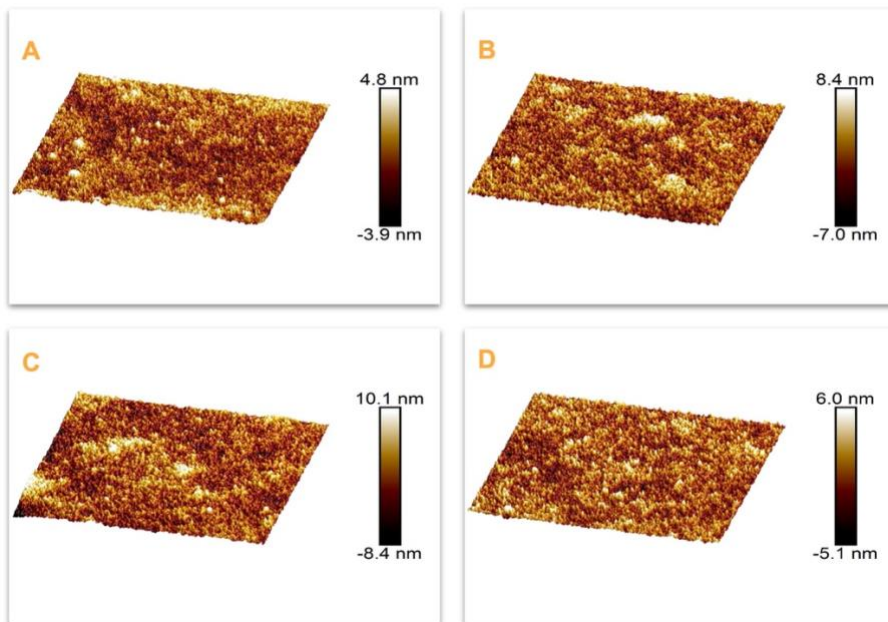


**Fig. 12.** Atomic Force Microscopy of the composites films with increasing concentration (A) GO-CS-Pt-Cu<sub>2</sub>O/Cu(0.5), (B) GO-CS-Pt-Cu<sub>2</sub>O/Cu(1), (C) GO-CS-Pt-Cu<sub>2</sub>O/Cu(1.5), (D) GO-CS-Pt-Cu<sub>2</sub>O/Cu(2).

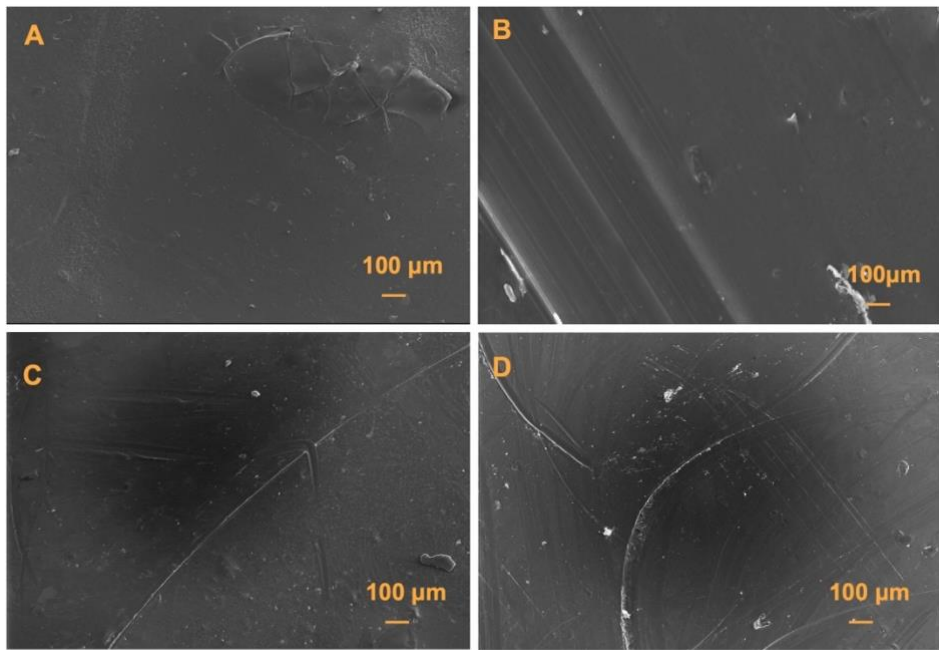


**Fig. 13.** SEM images of (A) GO-CS-Pt-Cu<sub>2</sub>O/Cu(0.5), (B) GO-CS-Pt-Cu<sub>2</sub>O/Cu(1), (C) GO-CS-Pt-Cu<sub>2</sub>O/Cu(1.5), (D) GO-CS-Pt-Cu<sub>2</sub>O/Cu(2) of nanocomposite thin films.

### 3.1.9. Migration of copper

Several studies have investigated the migration of copper from chitosan-copper nanocomposite (Ashrafi et al., 2020; Kalia et al., 2021; Llorens et al., 2012). In a study conducted by Liu et al. (2016), the objective was to examine the various parameters that influence the migration of copper in materials used for food packaging. This study showed that increased temperatures, longer exposure times and increased copper concentrations together contribute to an escalation of copper migration. It was found that the migration of copper from the packaging material into the food is accelerated at elevated temperatures, where copper concentrations up to 0.54 µg/mL migrated into rice vinegar from chitosan-copper films at high temperatures. It was also observed that longer exposure times lead to increased copper migration from the thin films into food simulants. Although copper nanoparticles in food packaging are extensively studied to improve mechanical properties, barrier properties, antimicrobial and antioxidant activities, there is little research on the migration of copper nanoparticles (CuNPs) from packaging coatings into food

products (Ahari & Lahijani, 2021; Cushen et al., 2014; F. Liu et al., 2016a; Mesgari et al., 2022).

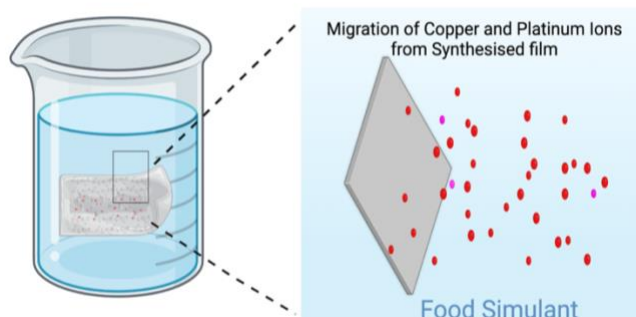


**Fig. 14.** Illustration of migration of copper and platinum ions from synthesised hybrid copper films

Different concentrations of GO-CS-Pt-Cu<sub>2</sub>O/Cu(0.5), GO-CS-Pt-Cu<sub>2</sub>O/Cu(1), GO-CS-Pt-Cu<sub>2</sub>O/Cu(1.5), GO-CS-Pt-Cu<sub>2</sub>O/Cu(2) nanocomposite films in chitosan were exposed to water, 10 % ethanol and 3 % acetic acid as food simulants at 32 °C for 10 days. The migration results show that the migration of copper ions from the film was less than 1 µg/L for all composite films and below the FDA approved concentration (5 µg/L). The results (Fig. 15) show that the migration of Cu from the thin films occurred in the order 3 % acetic acid > 10 % ethanol > water. GO-CS-Pt-Cu<sub>2</sub>O/Cu(1.5) showed the highest release of copper in only 3 % acetic acid, as chitosan has the highest solubility in acetic acid. Migration studies showed that the diffusion of copper ions from the film in all three food simulants, including 3 % acetic acid, remained below 1 mg kg<sup>-1</sup> and was lower than FDA's safety limit for copper migration into food substances. Nevertheless, only migration of copper ions was detected, but the nanoparticles remained intact within the membranes at all concentrations. Therefore, it is likely that the GO-CS-Pt-Cu<sub>2</sub>O/Cu composite films are safe for food packaging at normal temperature.

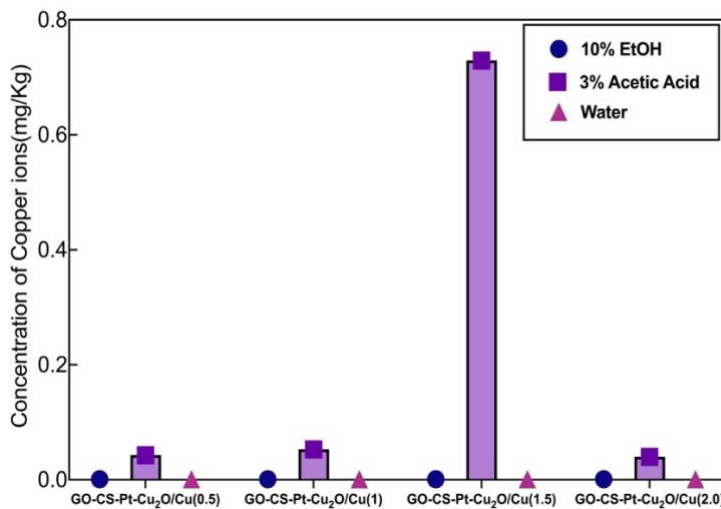


**Fig. 15.** The migration amount of copper (mg/kg) from the GO-CS-Pt-Cu<sub>2</sub>O/Cu(0.5), GO-CS-Pt-Cu<sub>2</sub>O/Cu(1), GO-CS-Pt-Cu<sub>2</sub>O/Cu(1.5), GO-CS-Pt-Cu<sub>2</sub>O/Cu(2) composite films, after 10 days in exposure to 10 % EtOH, 3 % Acetic Acid, and Water as food simulants.

Due to the different mechanical properties of the thin films as well as the differences in copper migration and biodegradability at variable weight concentrations of Cu<sub>2</sub>O/Cu, these films are suitable for food packaging with customizable properties. The integration of antibacterial properties, robust mechanical strength and customizable surface properties provides a versatile packaging solution that meets the diverse requirements of the food industry. Overall, this study provides valuable insights into the use of nanocoppers in food packaging and its potential impact on food preservation.

### 3.2. Characterisation of composites for adsorption studies

#### 3.2.1. XRD

The XRD patterns of GO, GO-MGH, and the composite of GO-MGH-CS performed in a  $2\theta$  range of 5–75°. In the XRD pattern of GO and GO-MGH, the diffraction peak at 10.98° corresponds to the typical (001) crystal plane of GO, which is also consistent with data published by other researchers (Johra et al., 2014; X. Zhang et al., 2022). The absence of a characteristic GO peak in the GO-MGH-CS composite can be explained by the possible overlap of the maghemite and chitosan peaks (Jiang et al., 2016). The values of  $2\theta = 30.2^\circ, 35.4^\circ, 42.5^\circ, 53.7^\circ, 57.5^\circ$ , and  $63.0^\circ$ , found in GO-MGH and GO-MGH-CS, correspond to the crystallographic planes (220), (311), (400), (422), (511), and (440) of maghemite ( $\gamma\text{-Fe}_2\text{O}_3$ ), respectively, which is consistent with the card (ICDD # 00-039-1346) and the literature data. In addition, an amorphous peak at  $2\theta = 17.5^\circ$  was found in the XRD pattern of the GO-MGH-CS composite, which can be attributed to chitosan.

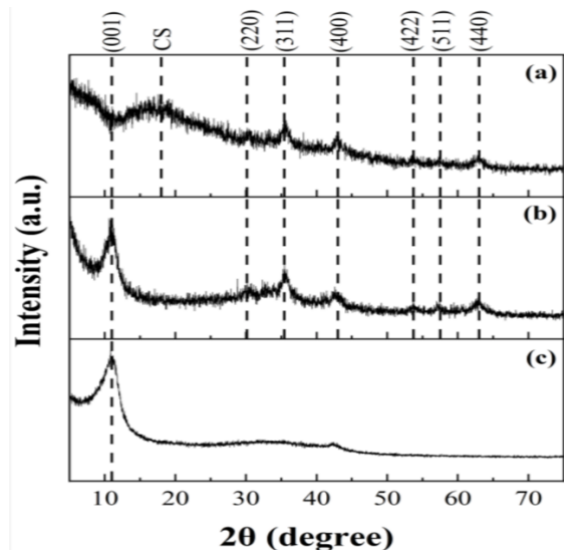


**Fig. 16.** XRD pattern of GO-MGH-CS (a), GO-MGH (b), and GO (c).

#### 3.2.2. Möessbauer Spectroscopy

The Möessbauer spectroscopy data presented in Table 3 and Fig. 17. Provide evidence of the presence of  $\text{Fe}^{3+}$  cations and the absence of  $\text{Fe}^{2+}$  cations in the MGH, GO-MGH, and GO-MGH-CS (I, II, III) samples. This

observation suggests that the samples include a maghemite phase rather than magnetite.

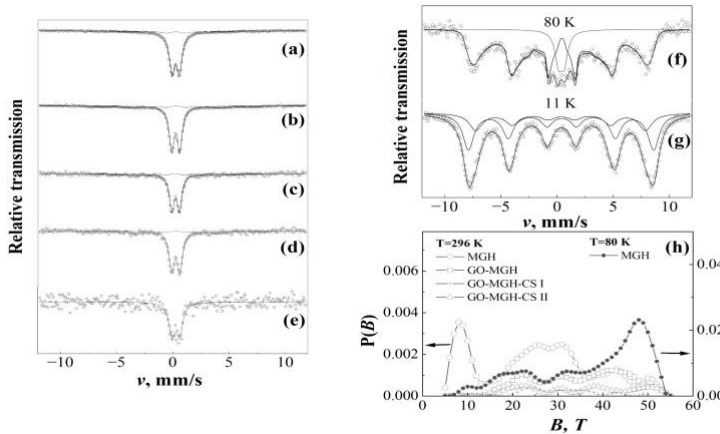


**Fig. 17.** Mössbauer spectra of samples at 296 K: MGH (a), GO-MGH (b), GO-MGH-CS I (c), GO-MGH-CS II (d), GO-MGH-CS III ©, MGH at 80 K (f), and 11 K (g). The applied hyperfine field distributions are shown in (h).

Although maghemite and magnetite have similar structures and magnetic characteristics, they exhibit distinct differences in terms of the existence of iron(III) cations in maghemite and the combination of iron(II) and iron(III) cations in magnetite (Yadav et al., 2020). The spectra of the MGH, GO-MGH, and GO-MGH-CS composites exhibit a doublet in the central region of the spectra (Fig. 17. (a–e)), which can be attributed to the presence of particles less than 10 nm. Nevertheless, apart from the doublet, around 18–19 % of the spectra pertain to the broader segment characterized by the hyperfine distribution  $P(B)$ . This occurrence can be rationalized by considering the particle size distribution and the existence of bigger particles measuring at least 10 nm. At room temperature, it has been observed that the average hyperfine field of distributions ranging from 25 to 35 T is approximately 30 to 50 % lower compared to the hyperfine field of bulk maghemite ( $B_0 = 49.1; 50.1$  T)(Oh et al., 1998). The decrease in the hyperfine field can be elucidated by the collective excitations of the magnetic moment of the minuscule maghemite nanoparticles. It is observed that an additional rise in the frequency of these excitations caused by smaller particles or elevated temperature induces superparamagnetic relaxation, which involves the reversal of the magnetic moment's orientation. This leads to a further

reduction in the spectrum's splitting and the emergence of a doublet at its centre. At reduced temperatures, there is a decrease in the rate of superparamagnetic relaxation and excitations. Consequently, the doublet observed in the spectra undergoes a transformation into magnetically split spectra, as visually depicted in Fig. 17 (f,g). The maximum particle size of about 11 nm, which is linked to the distribution of hyperfine fields at room temperature, was calculated using Eq. (12), considering the 30 % reduction in hyperfine field B due to the decrease in particle volume V (Dickson & Berry, 1986).

$$B = B_0 \left(1 - \frac{kT}{2KV}\right) \quad (12)$$

Where k, T, and K are the Boltzmann constant, temperature, and maghemite magnetic anisotropy. At 80 K, the reduction in temperature T led to a hyperfine field distribution that included 87 % of the spectral area. The average hyperfine field within this distribution was found to be 17-19 % lower than that of bulk maghemite at 77 K (Oh et al., 1998). According to Eq. 12, the measured particle size was 8.5 nm. However, it should be noted that smaller particles were present, which contributed to the appearance of a doublet in the spectrum. The temperature dependence of these spectra is consistent with previous findings (Mørup & Tronc, 1994; van Lierop & Ryan, 2001) which suggests that nanoparticles with a diameter of 6 nm exhibit similar behaviour. The maghemite mass percentage (M) estimation in the samples presented in Table 1 was conducted based on the ratio derived from the assumption that the spectrum area is directly proportional to the quantity of maghemite and the thickness of the sample mass. The samples had varying mass thicknesses ranging from 20 to 40 mg/cm<sup>2</sup>, except for GO-MGH-CS III, which had a 110 mg/cm<sup>2</sup> thickness. Table (3) shows the parameters of Mössbauer spectra of Graphene Oxide-Maghemite-Chitosan composite

**Table 3.** Parameters of Mössbauer spectra:  $T$ —measurement temperature,  $M$ —mass percentage of maghemite,  $I_d$  and  $I_B$ —relative area of doublet and hyperfine distribution or sextet, respectively,  $\delta$ —isomer shift relatively to  $\alpha$ -Fe,  $\Delta(2\epsilon)$ —quadrupole splitting (shift),  $B$ —hyperfine field.

Sample	T, K	M, %	Doublet			Hyperfine Distribution/Sextets				Field, T
			$I_d$ , %	$\delta$ , mm/s	$\Delta$ , mm/s	$I_B$ , %	$\delta$ , mm/s	$\Delta$ , mm/s		
MGH	296	100	81	0.36 ± 0.01	0.66 ± 0.01	19	0.36 *	0 *	25.4 **	
	80		13	0.48 ± 0.01	0.51 ± 0.04	87	0.46 ± 0.01	-0.14 ± 0.02	37.2 **	
	11		0	-	-	61	0.49 ± 0.01	-0.07 ± 0.02	51.0 ± 0.2	
						39	0.45 ± 0.01	-0.06 ± 0.03	46.8 ± 0.4	
GO-MGH	296	32	81	0.36 ± 0.01	0.72 ± 0.01	19	0.36 *	0 *	34.6 **	
GO-MGH-CS I	296	15	80	0.36 ± 0.01	0.68 ± 0.01	20	0.30 ± 0.06	0 *	29.9 **	
GO-MGH-CS II	296	17	74	0.37 ± 0.01	0.73 ± 0.01	26	0.37 *	0 *	35.2 **	
GO-MGH-CS III	296	0.6	100	0.37 ± 0.02	0.68 ± 0.03	-	-	-	-	

### 3.2.3. FTIR

The FTIR data describe the functional groups (GO, MGH, and CS) and their transformations in the GO-MGH, GO-CS, and GO-MGH-CS (I, II, III) composites (Fig. 18). The bands at 1226, 1623, and 1056  $\text{cm}^{-1}$  in the GO spectrum are related to C-O-C, aromatic C=C, and epoxy C-O stretching vibrations, respectively, whereas the bands at 1718 and 1397  $\text{cm}^{-1}$  correspond to the carboxyl C=O stretching vibrations (Ullah et al., 2020). MGH Ferreira et al. (2020) discovered a distinct band of Fe-O stretching vibrations at 585  $\text{cm}^{-1}$ . Furthermore, as demonstrated by the broad bands in the 580 and 800  $\text{cm}^{-1}$  regions (Chandrasekaran et al., 2015), the resulting maghemite had a well-ordered structure. The GO-MGH spectrum contained bands corresponding to the functional groups of graphene oxide and maghemite. The positions and intensities of the bands fluctuate.

The band at 1226  $\text{cm}^{-1}$  vanished, and a new band emerged at 1149  $\text{cm}^{-1}$  demonstrating the interaction of graphene oxide with maghemite (Ferreira et al., 2020). Furthermore, in the spectra of GO, MGH, and GO-MGH, the O-H stretching vibrations corresponded to a broad band at approximately 3000-3700  $\text{cm}^{-1}$ . For CS, the band at 892  $\text{cm}^{-1}$  corresponds to the CH bending of the monosaccharide ring. C-O stretching is indicated by the bands at 1023 and 1058  $\text{cm}^{-1}$ . The asymmetric C-O-C stretching and bending vibrations of the hydroxyl groups in chitosan were responsible for the signals at 1151 and 1261  $\text{cm}^{-1}$ . The bands at 1320 and 1651  $\text{cm}^{-1}$  show the presence of the C-N of amide III and C=O of amide I of the leftover N-acetyl groups. The band corresponding to the N-H of amide II was not observed due to overlap with other signals. The peaks at 1374 and 1418  $\text{cm}^{-1}$  represent the symmetrical deformation of  $\text{CH}_3$  and bending of  $\text{CH}_2$ , respectively. The band at 1589  $\text{cm}^{-1}$  corresponds to the N-H bending of the main amine. The bands at 2868 and 2920  $\text{cm}^{-1}$  confirm the occurrence of asymmetric and symmetric C-H stretching, respectively. The N-H and O-H stretching vibrations are represented by the absorption bands at 3292 and 3350  $\text{cm}^{-1}$ , respectively (Fernandes Queiroz et al., 2015).

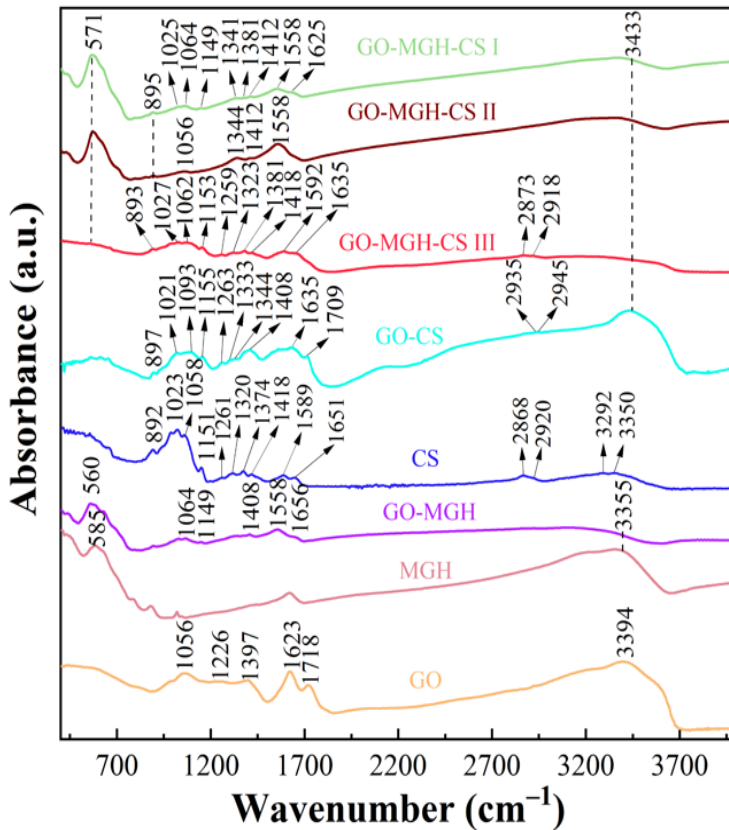


**Fig. 18.** The FTIR spectrum of MGH, GO-MGH, GO-MGH-CS I, GO-MGH-CS II, GO-MGH-CS III composites.

The absorption bands of graphene oxide and chitosan, as well as the absorption bands of maghemite, were present in the spectra of the GO-CS and GO-MGH-CS composites (I, II, and III). The spectra of the composites displayed variations in intensity and shift of the bands compared to the spectra of the original materials. The band associated with N-H stretching was absent in the spectra of the GO-MGH-CS composites. The intensity of the bands corresponds with the C-H stretching of chitosan and Fe-O maghemite, which decreased significantly for the GO-MGH-CS I, II, and III composites. This interaction was attributed to the formation of covalent bonds between the oxygen-containing functional groups of GO/GO-MGH and CS, as reported in previous studies (El Rouby et al., 2018; B. Zhang et al., 2018).

### 3.2.4. Raman Spectroscopy

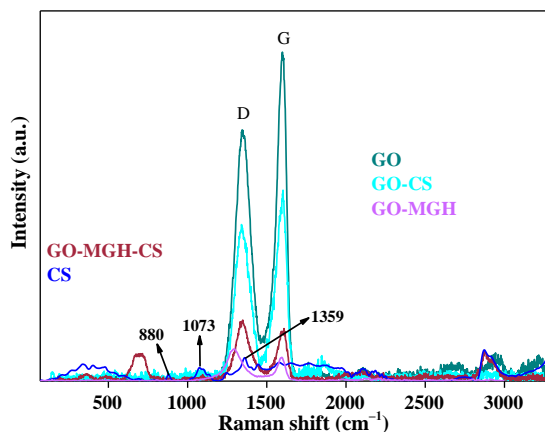


**Fig. 19.** The Raman spectrum of GO, GO-CS, GO-MGH-CS, GO-MGH, and CS.

The results of Raman spectroscopy (Fig. 19) showed the presence of an NH<sub>2</sub> band at 880 cm<sup>-1</sup> in the chitosan spectra. The stretching vibrations of the glycosidic bond, the ether bond and the methyl group are responsible for the bands at 1073 and 1359 cm<sup>-1</sup>, respectively (Vo et al., 2020). The spectra of GO and the composites containing GO showed distinct D and G bands in the ranges 1295-1347 cm<sup>-1</sup> and 1596-1609 cm<sup>-1</sup>, respectively. The structural defects arising from oxygen-containing functional groups in the basal plane of the disordered carbon are associated with the D band. In contrast, the stretching vibrations of the carbon atoms during  $sp^2$  hybridization are characterized by the G band (Sabzevari et al., 2018). In addition, the high intensity ratio of the D and G bands ( $I_D/I_G$ ) indicates that the oxygen-containing groups in GO decrease (López-Díaz et al., 2017). The  $I_D/I_G$  values for the composites were 0.82 (GO-CS), 1.16 (GO-MGH-CS) and 1.36 (GO-MGH), suggesting that the oxygenated groups in GO interact with the functional groups of CS and MGH.

### 3.2.5. TEM

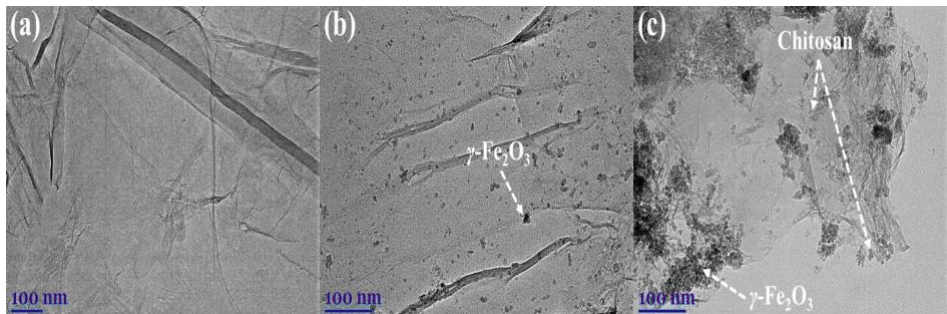


**Fig. 20.** The TEM images of GO (a), GO-MGH (b), and GO-MGH-CS (c).

TEM images of graphene oxide, GO-MGH and GO-MGH-CS. The GO-MGH composite (Fig. 20 (b)) exhibited a sheet structure with curved edges on which mainly individual maghemite particles (with a rare example of aggregates visible in the image) of 10 nm in size were dispersed. The GO sheets were aggravated by chitosan as a bridge between the layers in the GO-MGH-CS composite (Fig. 20 (c)), and the maghemite particles were aggregated on the GO surface.

### 3.2.6. Adsorption Studies

#### 3.2.6.1. Effect of the Initial Concentration of Eu(III) and the Adsorption Isotherms

It was found (Fig. 21) that increasing the initial Eu (III) concentration increased the adsorption capacity of the composites, with saturation reaching 200 mg/L for GO-MGH, GO-CS and GO-MGH-CS I. The adsorption capacity of GO-MGH-CS III showed a remarkable trend with an increase in relation to concentration, indicating a high number of available active sites. The adsorption capacity of GO-MGH-CS II also showed a positive relationship with concentration, indicating a large number of active sites. The maximum adsorption capacity/efficiency for GO-MGH, GO-CS and GO-MGH-CS I, II and III were 52/99, 54/99, 25/99, 103/99 and 102/100 (mg/g)/(%), respectively. It was also found that the percentage of chitosan in the GO-MGH-CS II and III composites had no effect on the adsorption capacity. The reduced adsorption capacity of GO-MGH-CS I seems to be related to the glutaraldehyde cross-linking of graphene oxide and chitosan,

which makes some active sites of GO inaccessible to Eu (III) (Huang et al., 2019b).

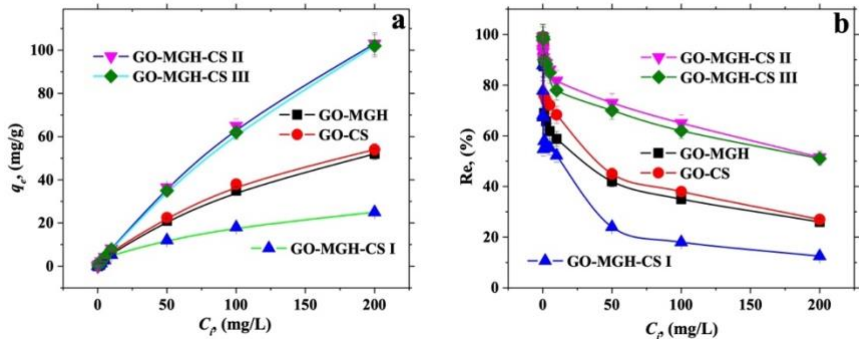


**Fig. 21.** Adsorption capacities (a) and efficiencies (b) of the composites as a function of initial concentrations

The collected data were subjected to nonlinear isotherm analysis using both Langmuir's Eq. (13) and Freundlich's Eq. (14). The results of this analysis are presented in Fig. 21. (a, b) and Table 4. The Langmuir and Freundlich isotherm models are widely used ( Li et al., 2014; Panda et al., 2017; B. Zhang et al., 2018) and suggest distinct adsorption scenarios. Langmuir's isotherm indicates a uniform distribution of active sites on a homogeneous adsorbent surface with equal adsorbate affinity, leading to monolayer adsorption, after which the adsorbates no longer interact. Conversely, Freundlich's isotherm implies multilayer adsorption on a heterogeneous surface with adsorbate interactions.

$$q_e = \frac{K_L q_m c_e}{(1 + K_L c_e)} \quad (13)$$

$$q_e = K_F c_e^{1/n} \quad (14)$$

Adsorption isotherm models describe substance adsorption onto a solid surface using Langmuir  $K_L$  (L/mg) and Freundlich  $K_F$  [(mg/g)(L/mg)] constants. The Freundlich constant measures the adsorption intensity, while the Langmuir constant measures the maximum quantity of adsorbate that can

be absorbed by a single surface site.  $q_m$  (mg/g) is the theoretical maximum quantity of adsorbate that may be adsorbed by a single site on the surface and  $q_e$ ;  $1/n$  in the Freundlich intensity parameter represents the adsorption intensity.

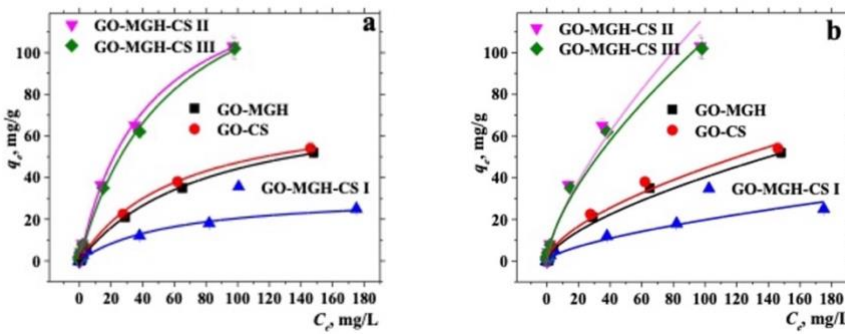


**Fig. 22.** The non-linear adsorption isotherms of the Langmuir (a) and Freundlich (b).

The Langmuir model provided a better explanation of the adsorption of Eu ions on the composites than the Freundlich model, as demonstrated by the higher  $R^2$  values obtained and the close approximation to the equilibrium adsorption capacity  $q_e$  for the maximum adsorption capacity values. Furthermore, the adsorption of Eu (III) on all composites was favourable, as evidenced by the values of the separation factor ( $R_L$ ) in Eq. 15, because adsorption is favorable at  $0 < R_L < 1$  and unfavourable at  $R_L > 1$ .

**Table 4.** The parameters of the isotherm models

Isotherms	Langmuir				Freundlich			
	Parameters	$R^2$	$Q_m$	$K_L$	$R_L$	$R^2$	$K_F$	$1/n$
GO-MSG	0.998	80	0.013	0.278	0.659	2.097	0.642	
GO-CS	0.995	77	0.016	0.238	0.540	2.681	0.859	
GO-MGH-CS I	0.982	32	0.017	0.227	0.871	1.000	0.649	
GO-MGH-CS II	0.999	147	0.024	0.172	0.967	4.794	0.695	
GO-MGH-CS III	0.998	160	0.018	0.217	0.920	5.100	0.658	

$$R_L = \frac{1}{(1 + K_L C_0)} \quad (15)$$

The predictions of the Langmuir model state that the adsorption of Eu (III) at the homogeneous sites of GO-MGH, GO-CS, and GO-MGH-CS (I, II, III) followed a monolayer type of adsorption, and there were no interactions in the adsorbate-adsorbate system following the adsorption process. This may be because of the large number of active sites that are present in the GO-MGH-CS II and III composites. In addition, the composite GO-MGH had a greater  $q_m$  value than maghemite and graphene oxide when used independently, in addition to a wide variety of other adsorbents, with the exception for chitosan. The composite GO-CS was inferior in terms of adsorption qualities to only chitosan and MnO<sub>2</sub>/graphene oxide, but the composite GO-MGH-CS I was inferior to almost all adsorbents except for magnetite and magnetic amidoxime-functionalized MCM-41.

### 3.2.6.2. Effect of pH

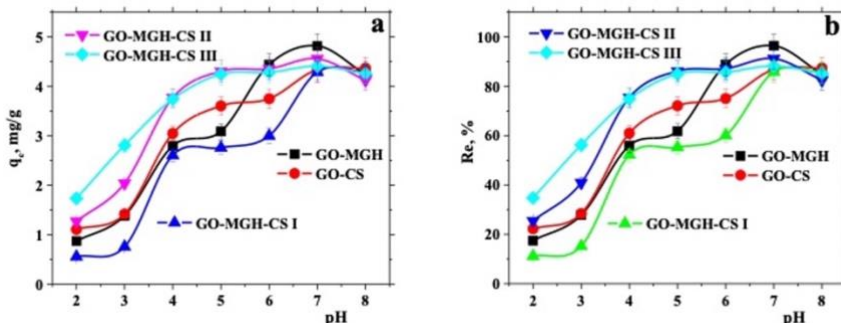


**Fig. 23.** Adsorption capacities (a) and efficiencies (b) of the composites as a function of initial concentration pH.

The pH owing to change in Eu (III) speciation is one of the most important factors affecting adsorption because Eu<sup>3+</sup> dominates at pH 5 and the hydrolysis species of Eu (OH)<sup>2+</sup> and Eu (OH)<sup>2+</sup> dominate at pH >5. GO-

MGH-CS composites (I, II, III) had high ion adsorption at pH levels larger than 4 and I at pH levels more than 6. Their adsorption capacity and efficiency rose with pH (Fig. 23 (a, b)). Europium ions behaved similarly in *Saccharomyces cerevisiae* immobilized in glutaraldehyde-cross-linked chitosan and graphene oxide nanosheets (B et al., 2019). Electrostatic repulsion between europium ions and the positively charged surface of GO-MGH-CS composites occurred at pH 7.5, the point of zero charge (pH<sub>PZC</sub>). Ion adsorption in the 2-7.5 range can be explained by complexation. Electrostatic interactions between europium ions and the composite's deprotonated surfaces cause adsorption at pH>7.5 (Huang et al., 2019; Li et al., 2014). Electrostatic attraction keeps Eu<sup>3+</sup> adsorption on GO-CS robust at pH 7 and 8, while complexation mechanisms increase it at pH 2-6. GO-MGH composite adsorption capacity/efficiency improves considerably at pH >5, possibly due to electrostatic attraction, as the observed pH<sub>PZC</sub> values are 3.9-4.2 for GO and 4.5-4.9 for MGH, which are close to published data 4.1-4.5 (Zhao et al., 2011) and 4.8 (Xu et al., 2016). Hence, a negative surface charge is suggested for composite GO-MGG at pH >5, supporting adsorption observations.

### 3.2.7. Kinetic Studies

The kinetics study revealed that the adsorption equilibrium for GO-MGH and GO-MGH-CS (I, II) composites was achieved in 30 minutes, while for GO-CS and GO-MGH-CS III composites it took 60 minutes. This is quicker than other comparable adsorbents, such as graphene oxide decorated with magnetite, which took 240 minutes and 60 minutes to reach adsorption equilibrium (Chen et al., 2009; Y. Li et al., 2014). To understand the kinetic and nature of Eu (III) adsorption on the composites, the data was fitted to pseudo-first-order and pseudo-second-order nonlinear kinetic models.

$$q_t = q_e(1 - e^{-k_1 t}) \quad (16)$$

$$q_t = q_e^2 k_2 t / (1 + k_2) q_e \quad (17)$$

The quantity  $q_t$  (mg/g) represents the amount of Eu (III) adsorbed per unit mass (mg/g) of the composite at time  $t$  (min), and the rate constants  $K_1$  (min<sup>-1</sup>) and  $K_2$  [g/(mg·min<sup>-1</sup>)] describe the kinetics of the pseudo-first-order and pseudo-second-order reactions, respectively. Fig 24. Fitting the

pseudo-first-order kinetic model (a) and the pseudo-second-order kinetic model (b) to the experimental values.

**Table 6.** The parameters of the kinetic models for Eu(III).

Models	Pseudo-First Order				Pseudo-Second Order		
Parameters	R <sup>2</sup>	K <sub>1</sub> (min <sup>-1</sup> )	q <sub>e</sub> Theo (mg/g)	q <sub>e</sub> Exp (mg/g)	R <sup>2</sup>	K <sub>2</sub> [g/(mg min <sup>-1</sup> )]	q <sub>e</sub> (mg/g)
GO-MGH	0.964	0.035	2.964	3.091	0.914	0.014	3.254
GO-CS	0.873	0.061	3.404	3.606	0.976	0.026	3.644
GO-MGH-CS I	0.904	0.050	2.689	2.763	0.931	0.027	2.872
GO-MGH-CS II	0.768	0.048	4.266	4.306	0.824	0.018	4.521
GO-MGH-CS III	0.851	0.048	3.995	4.249	0.914	0.016	4.320

The empirical data exhibited more substantial alignment with the pseudo-second-order model, as evidenced by the R<sup>2</sup> values. The maximum adsorption capacity also displayed a statistically significant increase, averaging 1.4 times higher than the equilibrium adsorption capacity (q<sub>e</sub>). The adsorption of Eu (III) on GO-MGH was described more accurately by a pseudo-first-order kinetic model. The results obtained from the pseudo-second-order model suggest that chemisorption occurred in the Eu (III)-GO-CS and Eu (III)-GO-MGH-CS (I, II, III) systems. On the other hand, the pseudo-first-order model indicates that the adsorption in the Eu (III)-GO-MGH system is of physical character (Al-Musawi et al., 2022).

Similarly, the adsorption of Eu on GO-MGH through physical means, as well as its chemical adsorption on GO-MGH-CS (I, II, III) and GO-CS, could be elucidated by examining the influence of pH on the adsorption process. Kinetic investigations were conducted at a pH value of 5, during which the surface charge of GO-MGH-CS (I, II, III) and GO-CS was observed to be positive. Concurrently, the Gibbs free energy change (GO-MGH) exhibited a negative value, resulting in the prevalence of chemical reactions in the former scenario and physical transformations in the latter.

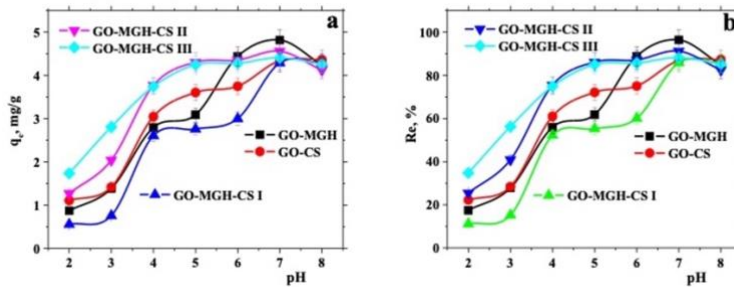
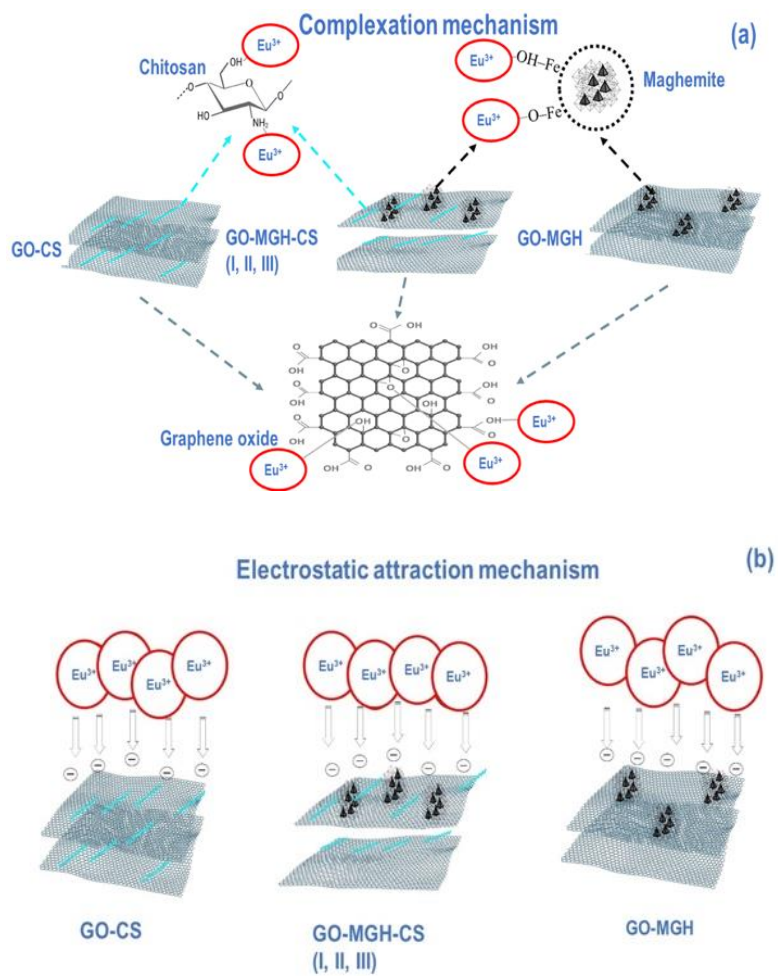


**Fig. 24.** Fitting the pseudo-first-order kinetic model (a) and the pseudo-second-order kinetic model (b) to the experimental values.

### 3.2.8 Adsorption Mechanism

The investigation of the influence of pH and kinetics sheds light on the chemical and physical properties of Eu ion adsorption on composites. Previous studies have used X-ray photoelectron spectroscopy and FTIR to examine the interaction between Eu (III) and various functional groups present in graphene oxide, MnO<sub>2</sub>/graphene oxide, chitosan, amidoxime-functionalized magnetic chitosan microparticles, and maghemite. These functional groups included C=O (carbonyl and carboxyl groups), C–O (epoxy group), O–H, C=C, C–C (alkoxy group), chitosan (NH<sub>2</sub> and OH), maghemite (Fe–O/OH), and Fe(III)- $\gamma$ -Fe<sub>2</sub>O<sub>3</sub>.

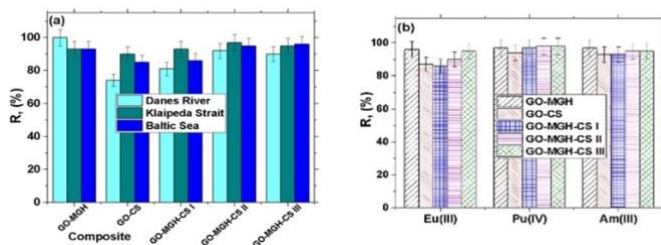
The investigation also revealed that the adsorption mechanism of these materials involves complexation and electrostatic attraction, as evidenced by the influence of pH and ionic strength on adsorption. Experimental and published data support that Eu adsorbs onto composites through complexation and electrostatic attraction (Cadogan et al., 2014; Hamza et al., 2018; Ma et al., 2019; B. Xu et al., 2016).



**Fig. 25.** Proposed mechanism of adsorption of Eu (III) on composites by complexation (a) and electrostatic attraction (b).

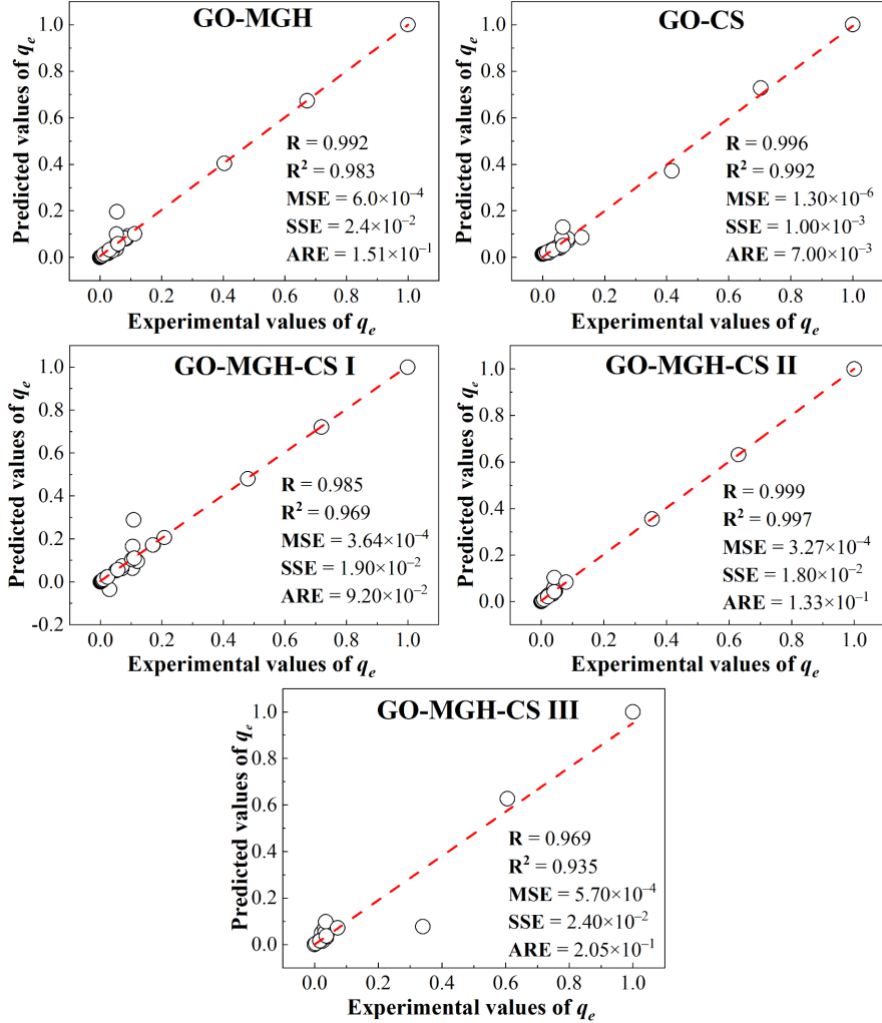
### 3.2.9. Removal of Eu (III), Pu (IV), and Am (III) from Natural Waters

Fig. 26. (a) depicts data on the adsorption of europium by composites in natural waters of the Danes River, Klaipeda Strait, and Baltic Sea, with adsorption efficiencies ranging from 74-100, 90-97, and 85-96 %, respectively. The experiment was carried out under near-natural settings (typically, Eu concentrations in freshwater range between 1 mg/L and  $1.1 \times 10^{-6}$  in seawater) without introducing stable Eu to the water samples and using dialysis tubes with a seven-day contact. The major species of Eu (III) in natural waters at pH 7.8 had the highest effectiveness of all sorbents examined,  $\text{Eu}^{3+}$  and  $\text{Eu}(\text{CO}_3)^+$  (Plancque et al., 2003). Data on the pre-concentration of Eu (III), Pu (IV), and Am (III) from seawater samples revealed high efficiency for all composites investigated when the composites were introduced into seawater samples for 24 h (Fig. 26. (b)). These preliminary findings imply that the composites could be employed for long-term exposure and pre-concentration of actinides from ambient samples, followed by radiochemical examination and quantification using alpha or mass spectrometry.



**Fig. 26.** Removal of Eu (III) from different types of natural waters (a) and comparison of adsorption efficiency of the composites for Eu (III), Pu (IV), and Am (III) in seawater samples (b).

### 3.2.10. ANFIS



**Fig. 27.** Comparison of the experimental data with the data predicted by ANFIS.

Fig. 27. displays the outcomes of the ANFIS-based analysis, which involves the comparison of experimental and anticipated data, both in terms of total and testing. Additionally, the figure also presents the results of the error analysis. According to Onu et al., (2021) and Souza et al., (2018) the testing data of these systems demonstrate strong positive correlations and minimal mean squared error (MSE), the sum of squared errors (SSE), and absolute relative

error (ARE) values, suggesting that ANFIS exhibits favourable generalisation capabilities.

The results of the 3D surface modelling (Figs. 28-30) show that Eu (III) is adsorbed on the composites MGH, GO-MGH, GO-MGH-CS I, GO-MGH-CS II and GO-MGH-CS III. The ANFIS prediction results showed close proximity to the empirical data, while the three-dimensional surface modelling results revealed the complex and non-linear nature of europium ion adsorption on the composites. This complex and linear nature of the composites is based on the investigated parameters such as pH, initial concentration, contact time and mass of adsorbent.

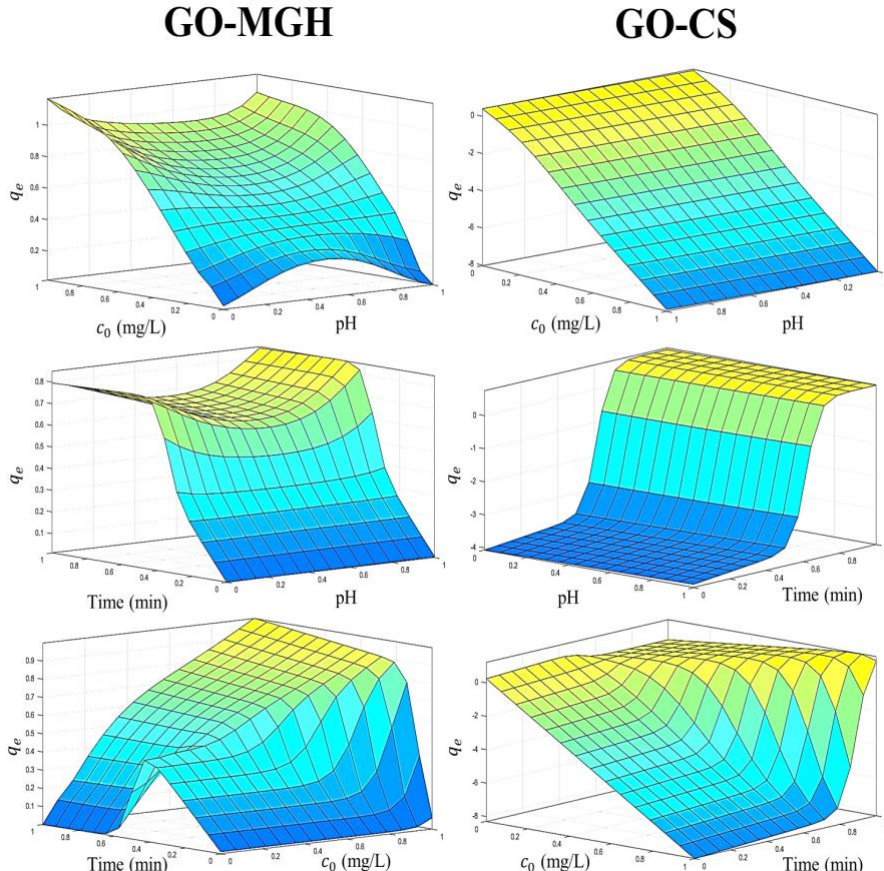


**Fig. 28.** Input-output surfaces of the ANFIS model for the GO-MGH and GO-CS composites.

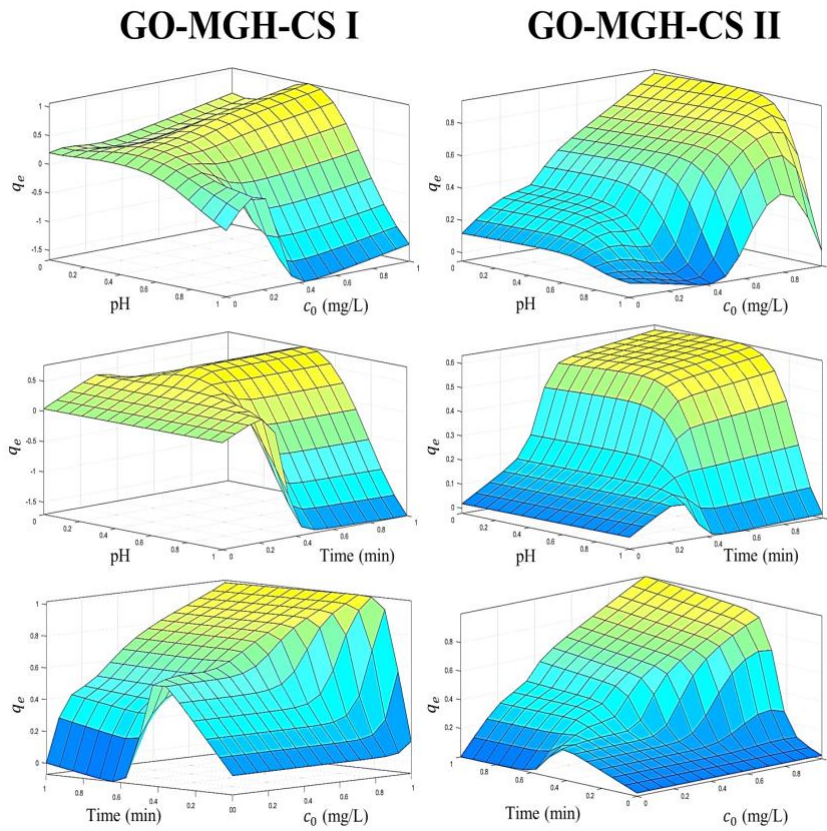


**Fig. 29.** Input-output surfaces of the ANFIS model for the GO-MGH-CS I and GO-MGH-CS II composites.

## GO-MGH-CS III

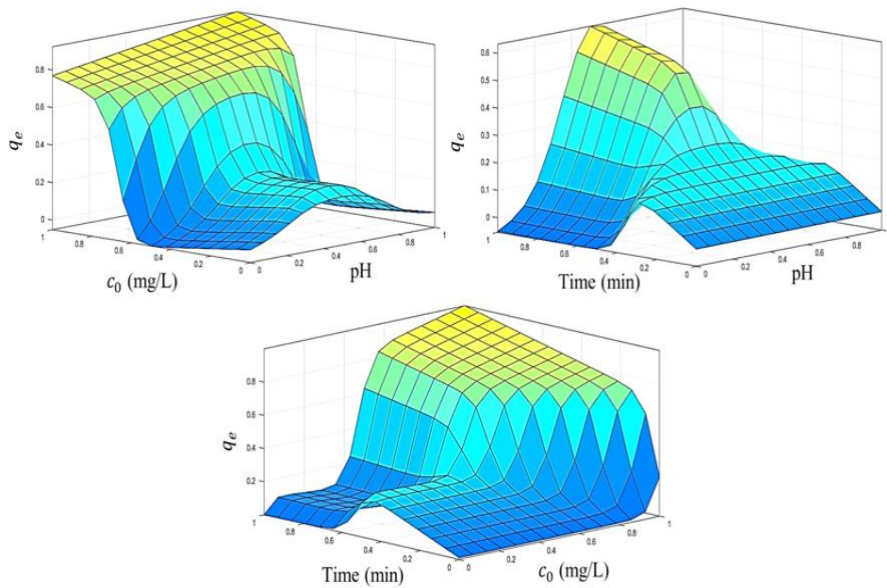


**Fig. 30.** Input-output surfaces of the ANFIS model for the GO-MGH-CS III composites.

The Adaptive Neuro-Fuzzy Inference System (ANFIS) enables researchers to effectively analyze tiny data sets while demonstrating strong performance and generalization capability. The generated prediction results are very close to the experimental data. Moreover, the 3D surface modeling shows that the interaction between the adsorbate and the adsorbents is characterized by a complex and non-linear behaviour. Furthermore, the trained ANFIS model can be used to predict the adsorption capacity of composites for ions, taking into account several factors such as pH, initial concentration, contact time, adsorbent mass and temperature.

## CONCLUSIONS

1. The thin films of graphene oxide and chitosan containing nanoparticles of Cu, CuO, Cu<sub>2</sub>O, Cu<sub>2</sub>O/Cu and Pt were synthesized, characterized and their antibacterial effect on *E. coli* and the optical properties of the thin films were evaluated. The thin film of the GO-CS-Pt-Cu<sub>2</sub>O/Cu showed a better antibacterial zone of inhibition (11 mm) and better optical transmittance (32.4 %) while maintaining film transparency.
2. Thus, in order to find the optimal concentration of Cu<sub>2</sub>O/Cu, different weights of Cu<sub>2</sub>O/Cu were added to chitosan-graphene oxide thin films. It was found that the physical properties of the GO-CS-Pt-Cu<sub>2</sub>O/Cu thin films change with different weight concentrations of Cu<sub>2</sub>O/Cu nanoparticles, making these thin films tunable.
3. The GO-CS-Pt-Cu<sub>2</sub>O/Cu(2) thin film showed a maximum migration rate of Cu ions from the thin film was estimated at 0.7 mg/kg (in 3 % acetic acid after 10 days), which is below the European Commission (EC) migration limit for copper (5 mg/kg), without traces of platinum ions. Even with other simulants (i.e., water and 10 % EtOH), the migration of Cu remained below 0.1 mg/kg.
4. The Langmuir, pseudo-second order and pseudo-first order models were found to be better suited to describe the data of Eu (III) adsorption on GO-MGH. This suggests that the adsorption of Eu (III) on GO-MGH follows a monolayer mechanism involving physisorption, while the pseudo-second-order model indicates the occurrence of chemisorption in the Eu (III)-GO-CS and Eu (III)-GO-MGH-CS (I, II, III) systems.
5. The GO-MGH-CS composites show equivalent efficiency (85-96 %) in the removal of Eu (III), Pu (IV) and Am (III) from seawater samples. The removal efficiency of Eu (III) from water samples of the Dane River, the Klaipeda Strait and the Baltic Sea ranged from 74 % to 100 %.
6. The ANFIS prediction results agreed well with the experimental data of Eu adsorption on GO-MGH-CS composites, and the three-dimensional surface modelling showed that the adsorption of europium ions on the composites was complicated and non-linear.

## SANTRAUKA

### ĮVADAS

Dėl savo unikalių savybių ir ekonominio naudingumo plastikai iš esmės pakeitė daugelį pramonės šakų. Plastiko gaminijų paplitimas įvairiose pramonės šakose - nuo pakuočių iki sveikatos priežiūros - rodo jų svarbą šiuolaikinėje visuomenėje (Andrade ir Neal, 2009). Nepaisant galimos naudos, plastiko perdirbimas susiduria su technologinėmis kliūtimis ir rinkos veiksniais. Šių kliūčių identifikavimas ir jų įveikimas suteikia galimybių padidinti plastiko naudojimo tvarumą ir sumažinti jo neigiamą poveikį aplinkai (Hopewell et al., 2009). Plastiko gamybos procesui reikia nemažai energijos, todėl jis reikšmingai prisideda prie bendro pasaulyje išmetamo anglies dioksido kiekio padidėjimo ir klimato kaitos (Cabenard et al., 2022; Geyer et al., 2017). Todėl vyksta ne tokią taršią polimerų paieška. Chitozanas yra biopolimeras, kuris gaunamas iš vėžiagyvių, (krevečių ir krabų kiautų) ir iš tam tikrų grybų rūšių. Ši medžiaga yra gaunama deacetilinant natūraliai gamtoje paplitusį chitiną, kuris pagal paplitimą yra antrasis polisacharidas po celiuliozės. Biologiškai skaidžios medžiagos sulaukė dėmesio dėl jų plataus pritaikymo įvairiose pramonės šakose, ypač biomedicinoje ir maisto produktų pakavime (Rinaudo, 2006).

Grafeno atradimas ir apibūdinimas - reikšmingas pasiekimas nanomedžiagų srityje (Novoselov et al., 2004). Grafenas sudarytas iš vieno anglies atomų sluoksnio, išsidėsčiusio dvimatėje gardelės struktūroje. Oksiduotame grafeno okside (GO) yra deguonies turinčių funkinių grupių, todėl jis lengviau disperguojamas įvairiuose tirpikliuose, todėl padidėja jo funkcionalizavimo galimybės. Dėl jam būdingos atominės struktūros grafenas pasižymi išskirtinėmis mechaninėmis savybėmis, neįtikėtinu tvirtumu ir gebėjimu išlaikyti lankstumą, taip išsiskirdamas iš kitų šiuo metu žinomų medžiagų (Zhu et al., 2010). Be to, grafeno oksido cheminis pritaikomumas turi daugybę perspektyvų prisijungti (Dreyer et al., 2009) papildomų molekulių, taip išplečiant jo pritaikymo spektrą ir pritaikant jo savybes konkrečioms reikmėms. Tai padidina grafeno oksido, kaip savarankiškos medžiagos ir kaip sudėtinių medžiagų, pasižyminčių patobulintomis savybėmis, pagrindo pritaikomumo perspektyvas.

**Maisto produktų pakuotės:** Chitozano (CS) plėvelės yra biologiškai skaidžios. Ši savybė padeda spręsti aplinkosaugos problemas, susijusias su

sintetinių plastikinių pakavimo medžiagų išlikimu aplinkoje (Kumar et al., 2020). GO savybė, svarbi maisto pramonei, yra jos išskirtinis gebėjimas veikti kaip dujų barjeras. GO gali veiksmingai blokuoti deguonies patekimą į maisto pakuotę, taip pailgindamas laiką, per kurį maistas išlieka tinkamas vartoti (Huang et al., 2012). GO sujungimas su CS į GO-CS kompozitus idealiai tinkas maisto pakuotėms, nes deguonies patekimo ir drėgmės valdymas gali prailginti gaminio galiojimo laiką (Cabrini et al., 2023; Han Lyn et al., 2019; Vilvert et al., 2022).

Metalų nanodalelės (MNP) dėl savo unikalių savybių sulaukė didelio dėmesio nanotechnologijų srityje (Ganachari ir et al., 2019). Įterptos į biopolimerus, pavyzdžiui, chitozaną, MNP gali gerokai pagerinti medžiagos savybes, kurias galima pritaikyti maisto pakavimo ir saugojimo technologijose (Adeyemi ir Fawole, 2023). Šių darinių fizikinės ir cheminės savybės visų pirma priklauso nuo to, ar yra laisvų paviršiaus elektronų. Todėl jie pasižymi išskirtinėmis savybėmis, iškaitant padidėjusią paviršiaus energiją, efektyvų plazmonų sužadinimą ir įvairias optines savybes (Kolwas & Derkachova, 2020; Dobrucka & Ankiel, 2019). MNP panaudojimas ypač pagerino įvairių maisto pakuočių savybes, tame tarpe mechanines, vandens garų pralaidumą ir antibakterinį aktyvumą (Cano-Sarmiento et al., 2015; dos Santos et al., 2020). Tai leido išsaugoti produktų šviežumą, pailginti jų galiojimo laiką ir sukurti saugesnius ir aplinkai draugiškesnius maisto pakavimo sprendimus (Kumar et al., 2021). Auksas (Au), sidabras (Ag), titano dioksidas ( $TiO_2$ ), cinko oksidas (ZnO), varis (Cu), vario oksidas (CuO) buvo tiriami dėl galimo pritaikymo maisto produktų pakuotėse (Mohan et al., 2019; Paidari & Ibrahim, 2021; Pissuwan et al., 2020; Devlieghere et al., 2004; Fernández et al., 2010; Zimoch-Korzycka & Jarmoluk, 2015; Oun & Rhim, 2017). Nustatyta, kad į GO-CS nanokompozitinę matricą įterpus metalo nanodaleles, galima padidinti antimikrobines savybes, atsparumą drėgmei ir tempimui, bei terminį stabilumą (Applerot et al., 2009; Dhillon et al., 2014; Terzioglu et al., 2020; Kanted et al., 2023).

Yra darbų apie GO-CS maisto pakuočių, kuriose kaip užpildai naudojami sidabro ir cinko oksidas, tačiau vario kaip užpildo panaudojimo GO-CS matricoje galimybės ištirtos mažai. Grass et al. (2011) teigimu, vario nanodalelių, pasižyminčių antimikrobiniu aktyvumu bei šilumos laidumu, įterpimas į šią matricą pagerina pakavimo medžiagų drėgmės barjerines ir mechanines savybes. Vienas iš pristatomo darbo tikslų - pateikti informaciją apie vario, kaip užpildo naudojimo GO-CS matricoje, šio nanokompozito sintezę ir charakteristikas bei galimybes jį naudoti maisto pakuotėse.

Metalų nanodalelės ar jonai iš pakuočių gali patekti į maisto produktus ar maisto modelinius produktus, o tai gali pakenkti maisto kokybei ir

sveikatai. Dėl didelio paviršiaus ir tūrio santykio metalo nanodalelės chitozane gali išskirti jonus į maisto modelinius produktus (Ma ir et al., 2019). Norint laikytis maisto saugojimą reglamentuojančių apribojimų, labai svarbu suprasti jonų migracijos greičius ir kiekius (Bott et al., 2014b). Migracijos parametrai apima metalo ir chitozano ryšio stabilumą, maisto modeliavimo medžiagos tipą, temperatūrą, pH ir kontakto laiką. Nustatyta, kad sidabro nanodalelės chitozano plėvelėse mažai migruoja į maisto modelinius tirpalus, tokius kaip acto rūgštis ir etanolis. Echegoyen ir Nerín (2013) naudojant ICP-MS analizę ištyrė nanosidabro dalelių prasiskverbimą ir išsiskyrimą iš antimikrobinių maisto talpyklų ir įrodė, kad migracija priklauso nuo pH ir kontakto laiko. Bumbudsanpharoke et al., (2019) ištyrė cinko migraciją iš mažo tankio polietileno - cinko nanokompozitinės plėvelės ir patvirtino, kad didžiausia migracija buvo stebima rūgščiame maisto simuliatoriuje. Hannon et al., (2016) nagrinėjo migracijos parametrus esant 60 °C temperatūrai 10 dienų 3 % acto rūgštyje (HAc), kurioje, naudojant ICP-AES įvertino bendrą Ag ir Cu migraciją į maisto imitatorių. Tačiau nerasta tyrimų apie GO-CS-Pt-Cu<sub>2</sub>O/Cu nanokompozito kartu su nanodalelių chitozano matricoje migraciją į maisto modelinius tirpalus taikymą.

Adsorbentai: Dabartiniame branduolinės energetikos sektoriaus pažangos etape ir artimiausioje ateityje uranas išlieka ir toliau bus labai svarbus pirminis išteklis patikimai elektros energijai gaminti, paliekant minimalų anglies dvideginio pėdsaką, ypač bazinės apkrovos energijos poreikiams tenkinti (Kurniawan et al., 2022). Pavojingos urano savybės, iškaitant jo radioaktyvumą, toksiškumą gyviems organizmams ir ilgą pusėjimo trukmę, kelia didelę grėsmę aplinkai, jei užterštos nuotekos į aplinką išleidžiamos tiesiogiai. Ilgalaikis žmogaus veiklos, susijusios su urano gavyba ir perdirbimu, poveikis aplinkai, taip pat įprastinai išmetimai iš atominių elektrinių ir netycinis užteršto vandens išleidimas (pavyzdžiui, įvykiai Pensilvanijoje 1979 m., Černobylyje 1986 m. ir Fukušimoje 2011 m.) kelia didelę grėsmę ir žmonėms, ir organizmams (Lv et al., 2021; Hirose, 2016). Per pastaruosius dešimt metų atlikta daug tyrimų atliekų regeneravimo srityje, taikant įvairius metodus, tokius kaip: jonų mainai, filtravimas, ekstrakciją tirpikliais, redukcinį nusodinimą ir adsorbciją (Foster et al., 2020; Mahmoud et al., 2017; Tang et al., 2020; G. Wu et al., 2020; Xie et al., 2019).

Maghemitas priskiriamas prie geležies oksido nanodalelių, kurioms būdingos magnetinės savybės. Maghemito magnetinės savybės yra labai naudingos, nes palengvina adsorbento atskyrimą nuo vandeninės terpės po adsorbcijos proceso. Po adsorbcijos radionuklidus galima patogiai atskirti naudojant išorinį magnetinį lauką, taip supaprastinant valymo procedūrą. Be

to, didelis medžiagos paviršiaus plotas ir įvairios aktyvios grupės suteikia daugybę vietų radionuklidams adsorbuoti (Afkhami ir Norooz-Asl, 2009; Etale ir kt., 2016). Dėl GO sudėtyje esančių deguonies turinčių funkinių grupių ji sėkmingai jungiasi su įvairiais metalų jonais ir radionuklidais. Dėl didelio šios medžiagos paviršiaus ploto ir žymaus adsorbcinio pajėgumo ji tampa patrauklia radionuklidų šalinimo priemone. Be to, grafeno oksidas gali sudaryti stabilias dispersijas vandenye, todėl lengviau sąveikauja su vandeniniais teršalais (Huang et al., 2019; Y. Sun et al., 2012).

Chitozanas dėl amino grupių buvimo gali sudaryti chelatus su metalų jonais ir radionuklidais. Chitozanas yra perspektyvus adsorbentas, pasižymintis aplinkai draugiškomis savybėmis, tokiomis kaip, biologinis sudeerinamumas ir skaidumas. Yra nustatyta, kad ši medžiaga pasižymigerasnėmis katijoninėmis savybėmis rūgštinėje aplinkoje, todėl padidėja jos gebėjimas adsorbuoti neigiamą krūvį turinčias medžiagas (S. Liu ir kt., 2021 ; Lujanienė ir kt., 2024). Citozano ir GO kompozitų derinys kartu gali pagerinti radionuklidų adsorbcijos pajėgumus (Pujol Pozo et al., 2022).

Šiuo metu adsorbcijos tyrimuose plačiai taikomas mašininis mokymas. Jis leidžia prognozuoti adsorbcijos talpą arba adsorbentų efektyvumą kaip įvairių parametrų (pH, kontakto laiko, pradinės koncentracijos ir kt.) funkciją, o tai savo ruožtu yra svarbu planuojant eksperimentus, taupant laiką ir naudojamus reagentus (Amiri et al., 2013; Onu et al., 2021a). Tarp vyraujančių modeliavimo metodų yra atsako paviršiaus metodas, dirbtinių neuronų tinklas, neuroninis bendarasis regresijos tinklas ir adaptyvioji „neuro-fuzzy“ išvadų sistema. Iš visų šių sistemų ANFIS pademonstravo geriausias prognozavimo savybes (Dolatabadi et al., 2018). Adaptyvioji „neuro-fuzzy“ išvadų sistema (ANFIS) - tai hibridinis skaičiavimo modelis, kuriamo dirbtinio neuronų tinklo metodai integruoti su „fuzzy“ logikos metodikomis. ANFIS yra veiksminga metodika, naudojama sudėtingoms sistemoms, pasižymintiems netiesine elgsena, pavyzdžiui, adsorbentų ir adsorbentų sąveikai, modeliuoti ir analizuoti. Ji veikia kaip daugiapakopis tinklas, kuris konstruoja „fuzzy if-then“ taisyklių rinkinį ir generuoja iš anksto nustatytas įvesties-išvesties poras. Tačiau nerasta darbų apie ANFIS taikymą MGH, GO-MGH, GO-MGH-CS I, GO-MGH-CS II, GO-MGH-CS III europio adsorbcijai.

## TYRIMO TIKSLAS IR UŽDAVINIAI

Šiuo tyrimu buvo siekiama sukurti konceptualią sistemą, skirtą kurti aplikai draugiškus kompozitus ir membranas su reguliuojamu biologiniu skaidumu, kurie galėtų būti naudojami vandens sistemų apsaugai ir galėtų sumažinti

aplinkos užterštumą toksiškomis atliekomis, pakeičiant plastiką netoksiškomis natūraliomis medžiagomis. Teršalai gali būti išgaunami ir naudojami uždaro ciklo gamybos procesuose.

Tyrimo tikslams pasiekti buvo suformuluoti šie uždaviniai:

1. Nanodalelių, kompozitų ir plėvelių sintezė ir jų apibūdinimas.
2. Eu adsorbcijos ant GO-MGH-CS kompozitų mechanizmo tyrimas kompleksiniuose laboratoriniuose eksperimentuose ir Eu adsorbcijos palyginimas su Am ir Pu adsorbcija gamtiniuose vandenye.
3. ANFIS modelio taikymas prognozuojant GO-MGH-CS kompozitų pajęgumą adsorbuoti  $\text{Eu}^{+3}$ .
4. GO-CS-Pt/vario oksido/vario kompositinių plėvelių, skirtų naudoti maisto produktų pakuotėms, antibakterinio poveikio *Escherichia coli* (*E.coli*) tyrimas.
5. GO-CS-Pt/vario oksido/vario kompositinių plėvelių savybių (UV spinduliuotės blokavimo, hidrofiliškumo, brinkimo ir tirpumo lygio) tyrimas.
6. GO-CS-Pt/vario oksido/vario kompozicinių plėvelių biologinio skaidymosi dirvožemyje ir vario migracijos greičio (dvigubo kontakto metodais maisto modeliniuose tirpaluose) tyrimas.

## TYRIMO NAUJUMAS

Pirmą kartą buvo susintetintos GO-CS-Pt/vario oksido/vario kompositinės plonos plėvelės ir nustatyta jų antimikrobinis aktyvumas. Be to, pirmą kartą buvo ištirtas GO-CS-Pt/vario oksido/vario kompozitų biologinis skaidumas dirvožemyje ir vario migracijos greitis dvigubo kontakto metodu maisto modeliniuose tirpaluose po 10 dienų.

Pirmą kartą MGH, GO-MGH, GO-MGH-CS I, GO-MGH-CS II, GO-MGH-CS III buvo naudoti Eu(III) adsorbcijos tyrimuose, bei Eu(III), Pu(IV) ir Am (III) šalinimui iš natūralių vandenų. Be to, ANFIS modelis pirmą kartą buvo pritaikytas sistemoms MGH-Eu(III), GO-MGH-Eu(III), GO-MGH-CS I - Eu(III), GO-MGH-CS II -Eu(III). ) ir GO-MGH-CS III -Eu(III).

## GINAMIEJI TEIGINIAI

1.  $\text{Cu}_2\text{O}/\text{Cu}$  nanodalelių, grafeno oksido-chitozano-platinos (Pt) nanokompozito ir chitozano matricos (plonos plėvelės) darinys, pasižymi antibakteriniu aktyvumu prieš *E.coli* ir mažesne vario jonų migracija iš GO-CS-Pt- $\text{Cu}_2\text{O}/\text{Cu}$  nanokompozito plėvelių.

2. Sudėtinių plėvelių stabilumas ir biologinis skaidumas, taip pat Cu migracijos greitis maisto modeliniuose tirpaluose padidėja plėvelėse sudidesne vario nanodalelių masės koncentracija.
3. GO-MGH-CS kompozitai, atliekant kompleksinius laboratorinius tyrimus, parodė puikų pajėgumą adsorbuoti Eu(III). Eu(III) pašalinimo iš įvairios kilmės vandens mėginių efektyvumas svyravo nuo 74 % iki 100 %.
4. ANFIS pasižymi geru našumu ir apibendrinamuoju gebėjimu prognozuoti GO-MGH-CS kompozitų gebą adsorbuoti Eu(III).

#### 4.1. MEDŽIAGOS IR METODAI

##### 4.1.1 Maisto pakavimo medžiagų sintezė

Vario (Cu) ir vario(II) oksido (CuO) nanodalelės: Pentahidratus vario sulfatas ( $\text{CuSO}_4 \cdot 5\text{H}_2\text{O}$ ) buvo ištirpintas distiliuotame vandenye, pastoviai maišant,  $60^\circ\text{C}$  temperatūroje. Tada tirpalo pH buvo pakoreguotas iki maždaug 9 naudojant natrio hidroksido (NaOH) tirpalą, gaunant tamsiai mėlyną koloidinę suspensiją. Vario nanodalelėms kaip reduktorius buvo naudota L-askorbo rūgštis, o CuO nanodalelės buvo sintetintos be reduktoriaus. Po reakcijos nanodalelės buvo išgautos centrifuguojant, nuplautos vandeniu ir etanoliu bei išdžiovintos.

Vario(I) oksido ( $\text{Cu}_2\text{O}$ ) nanodalelės: Panašiai kaip Cu ir CuO sintezės metu, buvo ištirpintas  $\text{CuSO}_4 \cdot 5\text{H}_2\text{O}$  ir sureguliuotas pH iki 9. Tačiau šiuo atveju prieš įdedant natrio borohidrido ( $\text{NaBH}_4$ ) kaip kitą reduktorių, buvo įpilta askorbo rūgštis ir NaOH tirpalą. Gautas tamsiai raudonas tirpalas parodė  $\text{Cu}_2\text{O}$  nanodalelių susidarymą, kurios vėliau buvo atskirtos centrifuguojant, plaunant ir džiovinant.

Vario(I) oksido / vario ( $\text{Cu}_2\text{O}/\text{Cu}$ ) nanodalelės:  $\text{Cu}_2\text{O}/\text{Cu}$  nanodalelių sintezė buvo dviejų etapų procesas. Pirmiausia  $60^\circ\text{C}$  temperatūroje buvo paruoštas tamsiai mėlynas koloidinis  $\text{CuSO}_4$  tirpalas (pH 9). Tada temperatūra buvo pakelta ir įdėta askorbo rūgštis ir NaOH mišinio. Po reakcijos  $90^\circ\text{C}$  temperatūroje tirpalas buvo atšaldytas ir gautos tamsiai raudonos  $\text{Cu}_2\text{O}/\text{Cu}$  nanodalelių nuosėdos. Galiausiai nanodalelės buvo išgrynintos centrifuguojant, plaunant ir džiovinant.

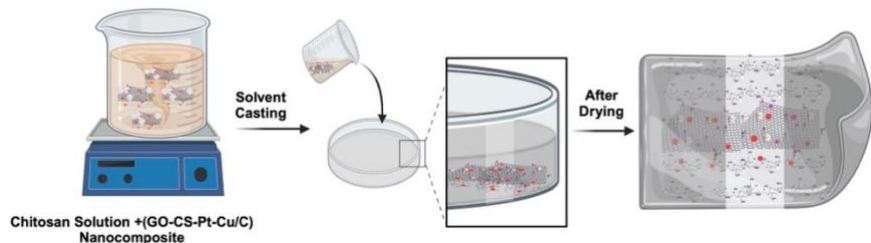
Grafeno oksido-chitozano (GO-CS) paruošimas: Chitozanas pirmiausia buvo sumaišytas su  $\text{KMnO}_4$  ir  $\text{H}_2\text{SO}_4$ , po to 3 valandas inkubuotas  $37^\circ\text{C}$  temperatūroje. Vėliau susintetinta grafeno oksido suspensija buvo įtraukta į apdorotą chitozaną, kad susidarytų GO-CS nuosėdos.

GO-CS-Pt nanokompozito sintezė: GO-CS buvo disperguotas dejonizuotame vandenye naudojant sonikaciją. Po to, tēsiant sonikaciją, į GO-CS dispersiją buvo įleistas NaOH tirpalas ir  $H_2PtCl_6$  tirpalas. Po 30 min. maišymo, naudojant magnetinę maišyklę, palaipsniui įpilta  $NaBH_4$  tirpalo. Galutinis produktas - GO-CS-Pt nanokompozitas - buvo gautas miltelių pavidalo po centrifugavimo ir džiovinimo 6 valandas 45 °C temperatūroje.

Grafeno oksido-Chitozano-Platinos-Vario oksido/Vario nanokompozito plonų plėvelių paruošimas: Chitozano plėvelėms, iškaitant GO-CS-Pt/Vario oksido/Vario/nanokompozitus, buvo paruoštas liejimo metodas. Šiame procese 5 ml 1,5 % tūrio acto rūgšties buvo sumaišyta su 20 mg Cu, CuO,  $Cu_2O$  ir  $Cu_2O/Cu$  NP atskirai, išdžiovinta ir pavadinta chitozano-grafeno oksidu-platinos-variu (GO-CS-Pt-Cu), chitozanas-grafeno oksidas-platinos-vario(II)oksidas (GO-CS-Pt-CuO), grafeno oksidas-platinos-vario(I)oksidas (GO-CS-Pt-Cu<sub>2</sub>O), chitozanas-grafenas Oksido-platinos-vario(I) oksido/vario (GO-CS-Pt-  $Cu_2O/Cu$ ) nanokompozitai.

Norint pagaminti ploną plėvelę, 20 mg vario nanokompozito miltelių buvo sumaišyta su 0,6 mg chitozano tirpalo 100 ml vandens. Tada mišinys dedamas ant silicio dioksono stiklo plokštelės ir paliekamas džiūti per naktį. Palyginimui, švari chitozano plėvelė buvo paruošta atliekant aukščiau nurodytus veiksmus. Pagamintos nanokompozitinės plėvelės buvo GO-CS-Pt-Cu, GO-CS-Pt-CuO, GO-CS-Pt-Cu<sub>2</sub>O ir GO-CS-Pt-Cu<sub>2</sub>O/Cu tokia tvarka. Prieš nustatant, kokios buvo išdžiovintos plėvelės, jos buvo nuplėštos nuo plokštelės ir džiovinamos vakuuminėje krosnyje 35°C temperatūroje 48 valandas (31 pav.).

**(A) Preparation of GO-CS-Pt-Cu<sub>2</sub>O/Cu nano composites thin film**



**(B) Demonstration of Cu<sub>2</sub>O/Cu thin film flexibility**



**31. pav.** GO-CS-Pt-Cu<sub>2</sub>O/Cu nano kompozitų plonos plėvelės paruošimas(A); GO-CS-Pt- Cu<sub>2</sub>O/Cu plonos plėvelės lankstumo demonstravimas (B).

#### 4.1.2. Apibūdinimas

Rentgeno spindulių difrakcija (XRD): Nustatoma medžiagų kristalinė struktūra.

Furjė transformacijos infraraudonųjų spindulių spektroskopija (FTIR): Analizuojama medžiagų cheminė sudėtis.

Atominės jėgos mikroskopija (AFM) ir energiškai dispersinė rentgeno spindulių spektroskopija (EDS): tiriama plonų plėvelių paviršiaus morfologija ir elementinė sudėtis (konkrečių bandinių atveju).

Lauko emisijos skenuojanti elektroninė mikroskopija (FE-SEM): Pateikia didelės skiriamosios gebos medžiagų paviršių vaizdus.

Kontaktinio kampo matavimai: Išmatuojamas plonų plėvelių hidrofiliškumas.

Induktyviai surištos plazmos optinės emisijos spektrometrija (ICP-OES): Kiekybiškai įvertinamas vario jonų, migruojančių iš sudėtinių plonų plėvelių, kiekis.

Plėvelės storis ir ultravioletinių spindulių spektroskopija: Šiame skyriuje aprašoma, kaip, naudojant skaitmeninį mikrometrą ir UV-VIS spektrofotometrą, matuojamas plonų plėvelių storis ir skaidrumas.

Antimikrobinis nanokompozitų ir plonų plėvelių aktyvumas: Susintetintų medžiagų antibakterinės savybės prieš *Escherichia coli* įvertintos taikant tiek kontakto su plėvele, tiek šulinėlių difuzijos metodus. Augimo slopinimo zona aplink medžiagas rodo jų veiksmingumą naikinant bakterijas.

Brinkimo laipsnis ir drėgmės kiekis: Kompozitinių plėvelių vandens įgeriamumas nustatomas matuojant jų masės pokyčius, skirtingai trukmei panardinus jas į vandenį.

Plėvelių paviršiaus hidrofiliškumas: Siekiant įvertinti plėvelės hidrofiliškumą, matuojamas vandens lašelio ir plėvelės paviršiaus kontaktinis kampas.

GO-CS-Pt-Cu<sub>2</sub>O/Cu plonų plėvelių irimas: Plonų plėvelių svorio sumažėjimas imituojamomis kompostavimo sąlygomis (užkasant dirvožemyje ir purškiant vandeniu) stebimas siekiant įvertinti jų irimo greitį.

Vario migracija iš GO-CS-Pt-Cu<sub>2</sub>O/Cu plonų plėvelių: Vario jonų išsiskyrimas iš plonų plėvelių į maisto imitacines medžiagas (etanolio ir acto rūgšties tirpalus) matuojamas naudojant ICP-OES, siekiant įvertinti galimas maisto saugos problemas.

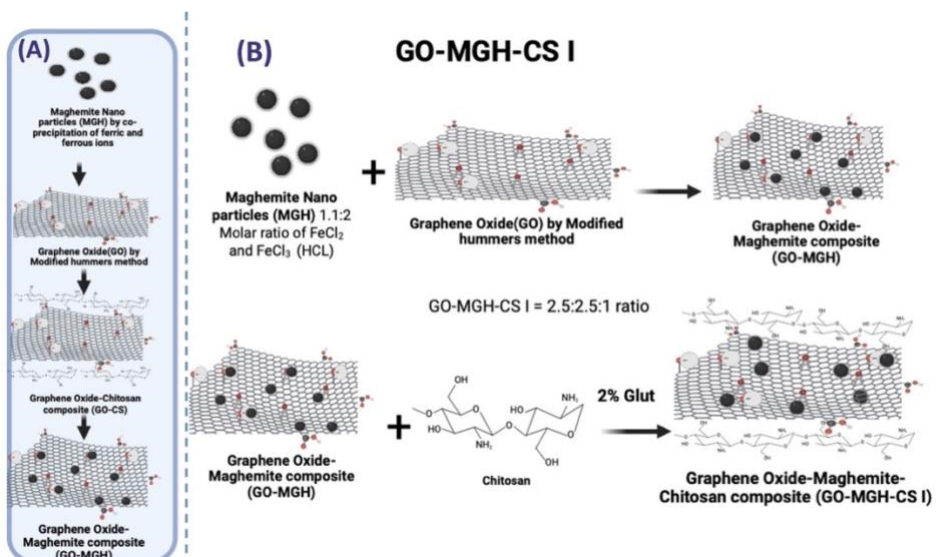
## 4.1.2 Magnetinio nanoadsorbento sintezė

### 4.1.2.1 Grafeno oksido-maghemito nanodalelių ir grafeno oksido-maghemito-chitozano kompozito paruošimas

Maghemito nanodalelės (MGH-NP): Maghemitas gaminamas sumaišius  $\text{FeCl}_2$  ir  $\text{FeCl}_3$  ir veikiamas natrio hidroksidu ( $\text{NaOH}$ ). Šis mišinys išplaunamas, parūgštinamas ir hidrotermiškai brandinamas, kad susidarytų MGH-NP. Galutinis produktas išgryninamas ir laikomas šaldytuve.

Grafeno oksido ir maghemito kompozitai (GO-MGH): MGH-NP ir grafeno oksido (GO) suspensijos sujungiamos veikiamos ultragarso. Mišinys laikomas tam tikrame pH diapazone, kad būtų galima jį naudoti toliau.

Grafeno oksido-maghemito-chitozano kompozitai (GO-MGH-CS-I, II, III): Aprašyti du variantai (I ir II), kurie šiek tiek skiriasi: Pirmiausia MGH-NP sintetinami, kaip aprašyta anksčiau. Paruošiami GO ir chitozano tirpalai. GO-MGH kompozitas gaunamas sumaišant MGH-NP ir GO suspensijas. I GO-MGH kompozitą įpilamas chitozano tirpalas, po to - glutaraldehidas (skersinio ryšio medžiaga) ir natrio hidroksidas ( $\text{NaOH}$ ) (I variantas). Mišinys maišomas, plaunamas ir džiovinamas vakuumu (32 pav.).



**32. pav.** Grafeno oksido-maghemito (GO-MGH) paruošimas (A); Grafeno oksido-maghemito-chitozano (GO-MGH-CS - I) kompozitai (B).

#### 4.2.2 Apibūdinimas

Kompozitai buvo charakterizuoti naudojant įvairius analitinius instrumentus. Rentgeno spindulių difrakcija (XRD) atlikta naudojant „Bruker D8“ difraktometrą (Brēmenas, Vokietija). Funkcinės grupės identifikuotos naudojant „Fourier-transform“ infraraudonosios spinduliuotės (FTIR) spektroskopiją su „Bruker Vertex 70v“ spektrometru (Brēmenas, Vokietija) 2  $\text{cm}^{-1}$  skiriamaja geba. FTIR analizei mėginių paruošti KBr peletų pavidalu. Kompozitų morfologija ir dalelių dydis tirti naudojant „Tecnai G2 F20 X-TWIN“ persviečiamos elektroninės mikroskopijos (TEM) prietaisą iš FEI (Eindhovenas, Nyderlandai). Šio TEM skiriamoji geba svyruoja nuo 0,25 iki 0,102 nm. Mössbauerio spektroskopija atlikta kambario temperatūroje naudojant „Wissenschaftliche Elektronik GmbH“ (Starnbergas, Vokietija) spektrometrą su  $^{57}\text{Co}$  (Rh) šaltiniu. Mössbauerio spektrai buvo analizuojami „Normos Dist“ programa.

#### Kompleksiniai laboratoriniai Eu (III) adsorbcijos tyrimai

Kompozitų Eu (III) adsorbcijos talpa buvo įvertinta atliekant kompleksinius laboratorinius eksperimentus. Pradinė Eu (III) koncentracija svyravo nuo 0,01 iki 200 mg/L, naudojant 1 g/L adsorbento kiekį (išlaikant 1:1000 g/mL santykį). Eksperimentai atlikti 25 °C temperatūroje, pH diapazone nuo 2 iki 8. Pradinis pH matuotas „WTW inoLab Multi Level 1 m“ (Weilheimas, Vokietija) pH matuokliu su „SenTix 41“ pH elektrodu (Weilheimas, Vokietija), kalibruotu pagal DIN 19266 standartinius buferinius tirpalus. Eu (III) izotopas  $^{152}\text{Eu}$  buvo naudojamas kaip Eu (III) žymeklis. Maišymo greitis buvo nustatytas 200 aps./min., o sąlyčio laikas nuo 5 iki 1440 minučių. Pasibaigus nurodytam sąlyčio laikui, adsorbentas atskirtas naudojant magnetą arba centrifugojant 20 000 for 15 minučių. Adsorbuoto Eu (III) kiekis kiekybiškai nustatytas  $\gamma$ -spektrometrija naudojant HPGe detektorius (techniniai duomenys pateikti disertacijoje). Lygtys (6) ir (7) buvo naudojamos kiekvieno kompozito Eu (III) adsorbcijos talpai ( $Q_e$ ) ir šalinimo efektyvumui ( $R_e$ ) apskaičiuoti.

#### Aktinidų koncentravimas iš jūros vandens

Buvo tirtas GO-MGH kompozitų gebėjimas sorbuoti aktinidus iš jūros vandens. Vieno litro jūros vandens mėginių buvo paženklinti Pu (IV) ir Am (III) izotopų mišiniu (nurodyta disertacijoje). Kompozitinė medžiaga

buvo įdėta į jūros vandenį, maišoma 1 valandą ir laikoma per naktį. Kompozitai buvo išgauti naudojant magnetą arba centrifugavimą. Po radiocheminio atskyrimo naudojant TEVA ir TRU kolonėles („Eichrom Industries“) su specifiniais žymekliais, alfa spektrometrija buvo matuojami Am ir Pu izotopai.

## ANFIS

Šiame tyrime buvo naudotas adaptyvus „neuro-fuzzy“ išvadų logikos interferencijos sistemos (ANFIS) modelis „MATLAB“ aplinkoje, siekiant numatyti įvairių kompozicinių medžiagų (GO-MGH, GO-CS ir kt.) adsorbcijos gebą šalinant teršalus iš vandens. Modelio mokymui buvo naudota 15 duomenų rinkinių, o testavimui ir atestavimui - po 6 atskirus rinkinius. ANFIS modelis turi šešis sluoksnius: pirmame sluoksnyje pateikiami įvesties duomenys, tokie kaip pH ir sąlyčio laikas. Sekančiose sluoksniuose naudojama „neuro-fuzzy“ išvadų ir taisyklių „fuzzy if-then“ logika duomenims apdoroti. Galiausiai, modelis pateikia sumodeliuotą adsorbcijos gebą. Modelio našumas buvo įvertintas naudojant tokius parametrus kaip vidutinė kvadratinė paklaida ir vidutinė santykinė paklaida, siekiant užtikrinti tikslumą numatant faktinę adsorbcijos gebą.

## 4.2. REZULTATAI IR APTARIMAS

### 4.2.1. Plėvelių maisto produktams saugoti charakterizavimas

*Rentgeno spindulių difrakcija (XRD)* patvirtino kompozitų susidarymą ir numatytių elementų buvimą. Pateikiame kiekvieno kompozito apžvalgą: GO-CS-Pt-Cu: Šis kompozitas turi šešiakampę GO struktūrą kartu su variu (Cu) ir platina (Pt). GO kristalito dydis yra 3,5 nm, o Cu ir Pt - atitinkamai 25,1 nm ir 3,6 nm. GO-CS-Pt-CuO: Šiame kompozite yra vario oksido (CuO). Vidutinis CuO nanodalelių kristalito dydis yra 11,9 nm. GO-CS-Pt-Cu<sub>2</sub>O: Šiame kompozite yra vario (I) oksido (Cu<sub>2</sub>O). Apskaičiuotas Cu<sub>2</sub>O kristalito dydis yra 16,9 nm. GO-CS-Pt-Cu<sub>2</sub>O/Cu: Šis kompozitas turi ir Cu<sub>2</sub>O, ir Cu.

*Fourierio transformacijos infraraudonosios spektroskopijos (FTIR)* analizė leido nustatyti kompozitų funkcinės grupės. Visuose kompozituose buvo pastebėtas pikas ties 1622 cm<sup>-1</sup>, atitinkantis C=C tempimo virpesį. Papildomai: GO-CS-Pt-CuO: Šiame kompozite yra pikai ties 474 ir 545 cm<sup>-1</sup> bangos ilgiais, priskiriami Cu-O virpesiams. GO-CS-Pt-Cu<sub>2</sub>O: Šiame kompozite yra papildomų pikų ties 1416 cm<sup>-1</sup> ir 1558 cm<sup>-1</sup> dėl O-H lenkimo ir

N-O tempimo bei papildomų pikų ties  $474$  ir  $545\text{ cm}^{-1}$ , priskirtų Cu-O virpesių lenkimo vibracijoms. GO-CS-Pt-Cu<sub>2</sub>O / Cu: Šiame kompozite yra pikas ties  $1719\text{ cm}^{-1}$  dėl C=O tempimo ir pikas ties  $1382\text{ cm}^{-1}$ , susijęs su O-H deformacijos virpesiais.

*Ultravioletinės spinduliuotės ekranavimo efektyvumas* Visų kompozitų ultravioletinių (UV) spinduliu (200–280 nm bangos ilgis) pralaidumas buvo mažesnis nei 1%, tai rodo puikias UV spinduliuotės blokavimo savybes. Tarp visų kompozitų GO-CS-Pt-Cu<sub>2</sub>O/Cu pasižymėjo mažiausiu UV spinduliuotės praleidimu. Iterpus vario nanodaleles, taip pat sumažėjo matomos šviesos pralaidumas.

*Antibakterinis tyrimas* Į kompozitus įterptos vario nanodalelės pasižymėjo puikiu antibakteriniu aktyvumu prieš *E. coli* bakterijas. Iš tirtų kompozitų GO-CS-Pt-Cu<sub>2</sub>O/Cu parodė didžiausią augimo slopinimo zoną (11,3 mm) (6 pav. (B)). Tai rodo, kad Cu<sub>2</sub>O/Cu nanodalelės yra ypač veiksmingos prieš *E. coli*. Antibakterinis mechanizmas greičiausiai susijęs su bakterinės membranos pažeidimu, kurį sukelia elektronų perdavimas tarp neigiamai įkrautų bakterijų ir vario nanodalelių (6 pav. (A)).

*Hidrodinaminės savybės* Vandens atsparumas ir brinkimo laipsnis yra labai svarbios maisto pakuočių medžiagų savybės. Kompozitų tirpumas (WS) didėjo didėjant Cu<sub>2</sub>O/Cu koncentracijai (7 pav.). Tačiau brinkimo laipsnis sumažėjo, o tai rodo pagerėjusį atsparumą drėgmės pralaidumui (Susilowati et al., 2020). Taip gali būti dėl vario nanodalelių ir vandens molekulių sąveikos. Kompozitų paviršiaus drėkinamumas buvo įvertintas vandens kontaktinio kampo (WCA) matavimais (8 pav.). Rezultatai parodė, kad didėjant nanodalelių koncentracijai, hidrofobiškumas mažėja. Tai rodo, kad kompozitai tampa hidrofiliškesni, kai nanodalelių kiekis didesnis, o tai gali sumažinti kondensato susidarymo ir maisto užteršimo riziką (Vasi et al., 2022). Sumažėjęs WCA gali būti dėl padidėjusio paviršiaus šiurkštumo, kurį sukelia nanodalelės (Lim et al., 2015).

*Kompozitinių plėvelių biodegradacija* Biodegraduojamos plėvelės yra aplinkai nekenksmingos, nes sujra nesukeldamos taršos. Šios medžiagos skyla etapais dėl įvairių veiksnių, tokų kaip drėgmė, temperatūra ir aplinkoje esantys mikroorganizmai. Įterptos medžiagos gali paveikti plėvelės biodegradaciją. Įterptos medžiagos gali pagerinti patvarumą, sudarydamos tankesnę struktūrą, arba pasižymeti antibakterinėmis savybėmis. Biologinis skaidymas paprastai apima vandens absorbciją, dėl kurios plėvelė išbrinksta, ir vėlesnį mikrobiologinį skaidymą. Svorio netekimas ir paviršiaus pokyčiai rodo skaidymosi mastą. Merino ir kt. (2019 m.) atliktame tyrime nustatyta, kad chitozanu dengtos krakmolo plėvelės dirvožemyje per 3 mėnesius žymiai degraduoja. Panašiai Oberlintner ir kt. (2021) įvairiuose dirvožemio

mëginiuose stebëjo greitą chitozano plévelių su „Quercus“ polifenolių ekstraktu (per 3 dienas) degradaciją. Hidrofilinė chitozano-grafeno oksido nanokompozitų savybë gali pagerinti jų biodegradaciją dirvožemyje, nes pagerina sąveiką su dirvožemio dalelëmis ir skatina sklaidymąsi. Paveiksle 9 parodytas chitozano plévelių su skirtingomis  $\text{Cu}_2\text{O}/\text{Cu}$  koncentracijomis svorio netekimas po 50 dienų laikymo dirvožemyje. GO-CS-Pt plévelė pasižymėjo didžiausiu biodegradacijos lygiu (86,12 %) dël dirvožemyje esančių mikroorganizmų. Didéjant  $\text{Cu}_2\text{O}/\text{Cu}$  kiekiui, biodegradacija mažėjo (nuo 68 % iki 45 %). Taip gali būti dël to, kad didesnė nanomedžiagų koncentracija sustiprina medžiagą ir sumažina sklaidymąsi.

*Energijos dispersivinė rentgeno spindulių analizė (EDX)* EDX analizè patvirtino vario buvimą plévelėse. Vario piko intensyvumas didéjo didéjant  $\text{Cu}_2\text{O}$  kiekiui. Elementinis žemëlapis (11 pav.) taip pat atskleidé gerą vario nanodalelių dispersiją plévelėse. AFM vaizdai (12 pav.) parodé sferines GO-CS-Pt- $\text{Cu}_2\text{O}/\text{Cu}$  nanodales, gerai integruotas į chitosano matricą. Dalelių dydis nerodë aglomeracijos požymių. Nors SEM vaizdai (13 pav.) visose plévelėse parodé lygų paviršių, AFM rodë didéjantį paviršiaus šiurkštumą didéjant  $\text{Cu}_2\text{O}$  kiekiui.

Vario migracija Vario migraciją iš GO-CS-Pt- $\text{Cu}_2\text{O}/\text{Cu}$  plévelių lemia temperatûra, poveikio laikas ir vario koncentracija. Ankstesniuose tyrimuose pranešta apie vario jonų migraciją aukštesneje temperatûroje ir ilgesnį poveikio laiką (Liu et al., 2016; Jiang et al., 2019). Šiame tyime buvo matuota vario jonų migracija iš kompozitinių plévelių į vandenį, 10 % etanolą ir 3 % acto rûgštį (maisto simuliatorius). Rezultatai (15 pav.) parodé minimalią vario migraciją (mažiau nei 1  $\mu\text{g}/\text{L}$ ) iš visų plévelių, gerokai žemesnę nei FDA ribą (5  $\mu\text{g}/\text{L}$ ). Didžiausia migracija stebëta naudojant 3 % acto rûgštį, po to – 10 % etanolį ir vandenį. Taip gali būti dël to, kad chitozanas yra labiau tirpus acto rûgštyje. Apskritai, vario migracija iš šių kompozitinių plévelių laikoma saugia, maisto pakavimo taikymams.

#### 4.2.2 Kompozitų, skirtų adsorbcijos tyrimams, apibûdinimas

Rentgeno spindulių difrakcijos (XRD) analizè (16 pav.) patvirtino maghemito ( $\gamma\text{-Fe}_2\text{O}_3$ ) buvimą GO-MGH ir GO-MGH-CS kompozituose. Bûdingo GO piko nebuvinamas kompozite rodo galimą maghemito ir chitosano pikų sutapimą.

Mösbauerio spektroskopijos rezultatai (17 pav.) atskleidé  $\text{Fe}^{3+}$  katijonų buvimą ir  $\text{Fe}^{2+}$  katijonų nebuvinamą, tai patvirtina maghemito, o ne magnetito, egzistavimą MGH, GO-MGH, and GO-MGH-CS (I, II, III) mëginiuose.

Pavaizduoti spektrų dubletai rodo mažesnių nei 10 nm dalelių buvimą. Platesni spektrų segmentai taip pat rodo didesnių dalelių ( $> 10$  nm) buvimą. Tačiau, be dubleto, 18–19 % spektrų priklauso plačiajai daliai, aprašytai hipersmulkiu P(B) pasiskirstymu, o tai galima paaiškinti dalelių dydžio pasiskirstymu ir didesnių  $\geq 10$  nm dydžio dalelių buvimu. Maksimalus dalelių dydis ivertintas atliekant matavimus kambario temperatūroje buvo maždaug 11 nm, tačiau matuojant 80 K temperatūroje nustatytas dalelių dydis yra 8,5 nm. Spektruose esantys dubletai taip pat rodo mažesnių 6 nm dalelių buvimą. Šie rezultatai atitinka ankstesnius tyrimus apie superparamagnetinę relaksaciją maghemito nanodalelėse.

*FTIR analizė* FTIR spektrai patvirtino funkcinių grupių būdingų GO, MGH ir CS kompozituose buvimą (18 pav.). GO spektre identifikuotos C–O–C, aromatinio C=C ir epoksidinio C–O juostos. MGH aptikta būdinga Fe–O tempimo virpesių ties  $585\text{ cm}^{-1}$  ryški juosta. GO–MGH spektre yra juostų, atitinkančių grafeno oksido ir maghemito funkcinės grupės. Šių juostų padėtis ir intensyvumas kinta. GO  $1226\text{ cm}^{-1}$  juosta kompozituose neaptikta dėl grafeno oksido ir maghemito sąveikos. GO–CS ir GO–MGH–CS (I, II, III) spektruose sujungtos grafeno oksido ir chitozano, o GO–MGH–CS kompozitų atveju – maghemito sugerties juostos. Palyginti su originalių medžiagų spektrais, kompozitų spektruose galima stebėti daugybę intensyvumo pokyčių ir juostų poslinkių. Juosta ties  $1550\text{ cm}^{-1}$ , atitinkanti amido II N–H, nebuvo aptikta, nes ji sutampa su kitomis juostomis.

GO–MGH–CS kompozitų I, II ir III atveju, C–H chitozano ir Fe–O maghemito tempimo jungčių juostų intensyvumas ženkliai sumažėjo. Remiantis gautais rezultatais ir publikuotais duomenimis, padaryta prielaida, kad sąveiką lemia kovalentinių ryšių susidarymas tarp GO/GO–MGH ir CS deguonies turinčių funkcinijų grupių.

*Ramano spektroskopija* Ramano spektroskopija patvirtino specifinių funkcinijų grupių buvimą chitoxane, GO ir kompozituose. Chitozano spectre aptikta būdinga  $\text{NH}_2$  juosta ties  $880\text{ cm}^{-1}$ . GO ir GO turinčių kompozitų spektrai rodė D ir G juostas  $1295$ – $1347\text{ cm}^{-1}$  ir  $1596$ – $1609\text{ cm}^{-1}$  diapazone. D juosta susijusi su struktūriniais defektais, atsirandančiais dėl deguonies turinčių funkcinijų grupių netvarkingos anglies bazineje plokštumoje, o G juosta apibūdina anglies atomų tempimo virpesius  $\text{sp}^2$  hibridizacijos metu. Didelis D ir G juostų intensyvumo santykis (ID/IG) rodo GO deguonies turinčių grupių sumažėjimą, dėl deguonies turinčių grupių dalyvavimo sąveikoje su CS ir MGH funkcinėmis grupėmis.

*TEM analizė* TEM vaizdai atskleidė kompozitų morfologiją (20 pav.). GO–MGH turėjo lakštinę struktūrą lenktais kraštais, kurių paviršiuje tolygiai pasiskirsto pavienės maghemito dalelės, kurių dydis  $< 10$  nm. GO–MGH–CS

kompozite chitozanas veikė kaip tiltas tarp GO sluoksnii, o maghemito dalelės yra agreguojamos GO paviršiuje.

*Adsorbcijos tyrimai* Didėjant pradinei Eu (III) koncentracijai, padidėjo kompozitų adsorbcijos geba, išskyrus GO-MGH-CS I. GO-MGH-CS III pasižymėjo didžiausiu adsorbciniu gebėjimu dėl daugybės aktyvių vietų. Chitozano masės procentas GO-MGH-CS II ir III neturėjo įtakos adsorbciniam pajėgumui. Mažesnis GO-MGH-CS I adsorbcinis pajėgumas greičiausiai atsiranda dėl glutaraldehydo poveikio, kuris sumažina prieinamų aktyvių vietų. Adsorbcijos elgsenai analizuoti buvo naudojami Langmuir ir Freundlich izotermų modeliai. Langmuir modelis rodo monosluoksnio adsorbciją ant vienalyčio paviršiaus, o Freundlich - daugiasluoksnę adsorbciją ant nevienalyčio paviršiaus.

*Langmuiro modelis* Langmuiro modeliavimo rezultatai rodo, kad Eu (III) būdinga monosluoksnio adsorbciją ant visų kompozitų. Didesnė GO-MGH  $q_m$  vertė rodo didesnę adsorbcijos talpą, lyginant su atskirais komponentais (išskyrus chitozaną) ir daugeliu kitų adsorbentų.

*pH poveikis* pH pokičiai veikia adsorbciją dėl Eu(III) cheminių formų kaitos. Visi kompozitai, išskyrus GO-MGH-CS I, rodo didesnę adsorbcijos talpą ir efektyvumą esant aukštesnėms pH vertėms. Šis elgesys siejamas su elektrostatinėmis sąveikomis ir kompleksavimu skirtinguose pH diapazonuose.

pH < 7,5: Elektrostatinis atstumimas tarp teigiamai įkrautų kompozitų ir Eu(III) jonų riboja adsorbciją.

pH 2-7,5: Tikėtina, kad adsorbciją lemia kompleksų susidarymas.

pH > 7,5: Elektrostatinė trauka tarp deprotonuotų kompozitinių paviršių ir Eu(III) jonų padidina adsorbciją.

GO-MGH pasižymi ženkliai padidėjusia adsorbcijos geba, esant pH > 5, o tai galimai lemia elektrostatinė trauka dėl neigiamai įkrauto paviršiaus šiame pH diapazone.

*Kinetika* Adsorbcinė pusiausvyra GO-MGH ir GO-MGH-CS (I, II) pasiekama per 30 minučių, o GO-CS ir GO-MGH-CS III - per 60 minučių. Tai greičiau, palyginti su kitais panašiais adsorbentais. Adsorbcijos proceso aprašymui buvo naudoti pseudo-pirmosios ir pseudo-antrosios eilės kinetikos modeliai. Duomenys geriau atitiko pseudo-antrosios eilės modelį, tai rodo cheminę Eu (III) adsorbciją GO-CS ir GO-MGH-CS kompozituose. Eu (III) adsorbcija ant GO-MGH vyko pagal pseudo-pirmos eilės modelį, tai rodo fizinę adsorbciją.

GO-MGC ir GO-MGC-CS (I, II) adsorbcijos pusiausvyra pasiekiamą per 30 minučių, o GO-CS ir GO-MGC-CS III – per 60 minučių. Jis yra greitesnis nei kiti panašūs adsorbentai. Adsorbcijos procesui apibūdinti buvo naudojami pseudo-pirmos ir pseudo-antros eilės kinetikos modeliai. Duomenys geriau atitinka pseudo-antros eilės modelį, nurodant Eu (III) chemisorbciją GO-CS ir GO-MGH-CS kompozituose. Eu (III) adsorbcija į GO-MGH laikėsi pseudo-pirmos eilės modelio, rodančio fizinę adsorbciją.

*Adsorbcijos mechanizmas* Kinetikos ir pH įtakos tyrimo rezultatai rodo europio jonų adsorbcijos cheminę ant GO-CS ir GO-MGH-CS arba fizinę ant GO-MGH kompozitų prigimtį. Ankstesniuose tyrimuose nustatytos funkcinės grupės panašiose medžiagose, kurios sąveikauja su Eu (III). Remiantis eksperimentiniais ir literatūros duomenimis, nustatyta, kad europis yra adsorbuojamas ant kompozitų dėl kompleksavimo ir elektrostatinės traukos.

*Radioaktyviųjų elementų šalinimas* Kompozitai efektyviai adsorbavo Eu (III) iš įvairių gamtinių vandens šaltinių (Danės upės, Klaipėdos sąsiaurio, Baltijos jūros). Efektyvumas siekė nuo 74 % iki 100 % (26 pav.). Eksperimentas vyko imituojant gamtines sąlygas, naudojant realias Eu koncentracijas ir nejnešant stabilaus Eu į vandens mėginius. Nustatyta, kad kompozitai vienodai efektyviai pašalina Eu (III), Pu (IV) ir Am (III) iš jūros vandens mėginių.

*ANFIS modeliavimas* Eksperimentinių ir prognozuojamų duomenų palyginimo rezultatai parodyti 27 paveiksle. Prognozuojamos ir eksperimentinės vertės gerai sutampa, o tai rodo didelį prognozės tikslumą. 3D paviršiaus modeliavimas Trimačio paviršiaus modeliavimo rezultatai (28-30 paveikslai) rodo, kad Eu (III) adsorbcijos elgsena ant kompozitų yra sudėtinga ir netiesinė, priklausomai nuo Eu pradinės koncentracijos, pH ir kontakto laiko. Stipri teigama koreliacija rodo, kad ANFIS modelis gali gana tiksliai numatyti adsorbcijos gebą ar elgseną, todėl jo naudojimas gali būti naudingas planuojant adsorbcijos eksperimentus.

### 4.3 IŠVADOS

1. Susintetintos plonos grafeno oksido ir chitozano plėvelės, turinčios Cu, CuO, Cu<sub>2</sub>O, Cu<sub>2</sub>O/Cu ir Pt nanodalelių, apibūdintos ir įvertintas jų antibakterinis poveikis *E. coli* bei plonų plėvelių optinės savybės. Plona GO-CS-Pt-Cu<sub>2</sub>O/Cu plėvelė parodė geresnį antibakterinį poveikį (11 mm) ir optinį pralaidumą (32, 4 %), išlaikant plėvelės skaidrumą.
2. Taigi, siekiant rasti optimalią Cu<sub>2</sub>O/Cu koncentraciją, į chitozano-grafeno oksido plonąsias plėveles buvo dedama skirtingų svorių Cu<sub>2</sub>O/Cu. Nustatyta, kad GO-CS-Pt-Cu<sub>2</sub>O/Cu plonų plėvelių fizinės savybės keičiasi esant skirtingoms Cu<sub>2</sub>O/Cu nanodalelių masėms, todėl šias plonas plėveles galima derinti.
3. GO-CS-Pt-Cu<sub>2</sub>O/Cu(2) plona plėvelė parodė, kad didžiausias Cu jonų migracijos greitis iš plonos plėvelės buvo 0,7 mg/kg (3 % acto rūgštyje po 10 dienų), o tai yra mažesnis. Europos Komisijos (EK) nustatyta vario migracijos riba (5 mg/kg), be platinos jonų pėdsakų. Net naudojant kitus modelinius tirpalus (ty vandenį ir 10 % EtOH), Cu migracija išliko mažesnė nei 0,1 mg/kg.
4. Nustatyta, kad Eu (III) adsorbcijos ant GO-MGH duomenims aprašyti geriau tinka Langmuiro, pseudo-antrosios eilės ir pseudo-pirmosios eilės modeliai. Tai rodo, kad Eu (III) adsorbcija ant GO-MGH vyksta pagal viensluoksnį mechanizmą, apimantį fiziosorbciją, o pseudo-antrosios eilės modelis rodo, kad Eu(III)-GO-CS ir Eu(III)-GO-MGH-CS (I, II, III) sistemose vyksta chemisorbcija.
5. GO-MGH-CS kompozitai vienodai veiksmingai (85-96 %) šalina Eu (III), Pu (IV) ir Am (III) iš jūros vandens mėginių. Eu (III) pašalinimo iš Danės upės, Klaipėdos sąsiaurio ir Baltijos jūros vandens mėginių efektyvumas svyravo nuo 74 % iki 100 %.
6. ANFIS prognozavimo rezultatai gerai sutapo su eksperimentiniais Eu adsorbcijos ant GO-MGH-CS kompozitų duomenimis, o trimatis paviršiaus modeliavimas parodė, kad europio jonų adsorbcija ant kompozitų buvo sudėtinga ir netiesinė.

## REFERENCES

Abdolsattari, P., Rezazadeh-Bari, M., & Pirsa, S. (2022). Smart Film Based on Polylactic Acid, Modified with Polyaniline/ZnO/CuO: Investigation of Physicochemical Properties and Its Use of Intelligent Packaging of Orange Juice. *Food and Bioprocess Technology*, 15(12).  
<https://doi.org/10.1007/s11947-022-02911-3>

Abdullah, N., Sahudin, S., & Kaharudin, N. (2023). Exploring the Role of Chitosan in Fabricating Biodegradable Films for Functional Food Packaging: A Review. *Journal of Young Pharmacists*, 15(1).  
<https://doi.org/10.5530/097515050505>

Adeyemi, J. O., & Fawole, O. A. (2023). Metal-Based Nanoparticles in Food Packaging and Coating Technologies: A Review. *Biomolecules*, 13(7).  
<https://doi.org/10.3390/biom13071092>

Afkhami, A., & Norooz-Asl, R. (2009). Removal, preconcentration and determination of Mo(VI) from water and wastewater samples using maghemite nanoparticles. *Colloids and Surfaces A: Physicochemical and Engineering Aspects*, 346(1–3), 52–57.  
<https://doi.org/10.1016/j.colsurfa.2009.05.024>

Aftab, K., Hou, J., & Rehman, Z. U. (2022). 13 - Graphene oxide–metal oxide composites, syntheses, and applications in water purification. In M. A. Chaudhry, R. Hussain, & F. K. Butt (Eds.), *Metal Oxide-Carbon Hybrid Materials* (pp. 341–369). Elsevier.  
<https://doi.org/10.1016/B978-0-12-822694-0.00017-X>

Agbaogun, B. K., Alonso, J. M., Buddenbaum, H., & Fischer, K. (2021). Modelling of the adsorption of urea herbicides by tropical soils with an Adaptive-Neural-based Fuzzy Inference System. *Journal of Chemometrics*, 35(5), e3335. <https://doi.org/10.1002/cem.3335>

Ahari, H., & Lahijani, L. K. (2021). Migration of Silver and Copper Nanoparticles from Food Coating. *Coatings*, 11(4), 380.  
<https://doi.org/10.3390/coatings11040380>

Aider, M. (2010). Chitosan application for active bio-based films production and potential in the food industry: Review. In *LWT* (Vol. 43, Issue 6, pp. 837–842). Academic Press.  
<https://doi.org/10.1016/j.lwt.2010.01.021>

Akhavan, O., & Ghaderi, E. (2010). Cu and CuO nanoparticles immobilized by silica thin films as antibacterial materials and photocatalysts. *Surface and Coatings Technology*, 205(1), 219–223.  
<https://doi.org/10.1016/j.surfcoat.2010.06.036>

Al-Musawi, T. J., Mengelizadeh, N., Al Rawi, O., & Balarak, D. (2022). Capacity and Modeling of Acid Blue 113 Dye Adsorption onto Chitosan Magnetized by Fe<sub>2</sub>O<sub>3</sub> Nanoparticles. *J Polym Environ*, 30(1), 344–359. <https://doi.org/10.1007/s10924-021-02200-8>

Alves, Z., Ferreira, N. M., Ferreira, P., & Nunes, C. (2022). Design of heat sealable starch-chitosan bioplastics reinforced with reduced graphene oxide for active food packaging. *Carbohydrate Polymers*, 291, 119517. <https://doi.org/10.1016/j.carbpol.2022.119517>

Amiri, M. J., Abedi-Koupai, J., Eslamian, S. S., Mousavi, S. F., & Hasheminejad, H. (2013). Modeling Pb (II) adsorption from aqueous solution by ostrich bone ash using adaptive neural-based fuzzy inference system. *Journal of Environmental Science and Health, Part A*, 48(5), 543–558. <https://doi.org/10.1080/10934529.2013.730451>

Andrade, A. L., & Neal, M. A. (2009). Applications and societal benefits of plastics. *Philosophical Transactions of the Royal Society B: Biological Sciences*, 364(1526), 1977–1984. <https://doi.org/10.1098/rstb.2008.0304>

Anyaogu, K. C., Fedorov, A. V., & Neckers, D. C. (2008). Synthesis, Characterization, and Antifouling Potential of Functionalized Copper Nanoparticles. *Langmuir*, 24(8), 4340–4346. <https://doi.org/10.1021/la800102f>

Applerot, G., Lipovsky, A., Dror, R., Perkas, N., Nitzan, Y., Lubart, R., & Gedanken, A. (2009). Enhanced Antibacterial Activity of Nanocrystalline ZnO Due to Increased ROS-Mediated Cell Injury. *Advanced Functional Materials*, 19(6), 842–852. <https://doi.org/10.1002/adfm.200801081>

Ashrafi, M., Bayat, M., Mortazavi, P., Hashemi, S. J., & Meimandipour, A. (2020). Antimicrobial effect of chitosan–silver–copper nanocomposite on *Candida albicans*. *J Nanostruct Chem*, 10(1), 87–95. <https://doi.org/10.1007/s40097-020-00331-3>

B, A., Talasila, S., Rajesh, V., & N., R. (2019). Removal of Europium from aqueous solution using *Saccharomyces cerevisiae* immobilized in glutaraldehyde cross-linked chitosan. *Separation Science and Technology*, 54(10), 1620–1631. <https://doi.org/10.1080/01496395.2018.1556303>

Bai, W., Sheng, Q., & Zheng, J. (2016). Morphology controlled synthesis of platinum nanoparticles performed on the surface of graphene oxide using a gas-liquid interfacial reaction and its application for high-performance electrochemical sensing. *Analyst*, 141(14). <https://doi.org/10.1039/c6an00632a>

Bakshi, P. S., Selvakumar, D., Kadirvelu, K., & Kumar, N. S. (2020). Chitosan as an environment friendly biomaterial – a review on recent modifications and applications. *International Journal of Biological Macromolecules*, 150, 1072–1083.  
<https://doi.org/10.1016/j.ijbiomac.2019.10.113>

Banza, M., & Rutto, H. (2023). Modelling of adsorption of nickel (II) by blend hydrogels (cellulose nanocrystals and corn starch) from aqueous solution using adaptive neuro-fuzzy inference systems (ANFIS) and artificial neural networks (ANN). *The Canadian Journal of Chemical Engineering*, 101(4), 1906–1918. <https://doi.org/10.1002/cjce.24603>

Barra, A., Ferreira, N. M., Martins, M. A., Lazar, O., Pantazi, A., Jderu, A. A., Neumayer, S. M., Rodriguez, B. J., Enăchescu, M., Ferreira, P., & Nunes, C. (2019). Eco-friendly preparation of electrically conductive chitosan - reduced graphene oxide flexible bionanocomposites for food packaging and biological applications. *Composites Science and Technology*, 173, 53–60.  
<https://doi.org/10.1016/j.compscitech.2019.01.027>

Beigmohammadi, F., Peighambardoust, S. H., Hesari, J., Azadmard-Damirchi, S., Peighambardoust, S. J., & Khosrowshahi, N. K. (2016). Antibacterial properties of LDPE nanocomposite films in packaging of UF cheese. *LWT - Food Science and Technology*, 65, 106–111.  
<https://doi.org/10.1016/j.lwt.2015.07.059>

Betancourt-Galindo, R., Reyes-Rodriguez, P. Y., Puente-Urbina, B. A., Avila-Orta, C. A., Rodríguez-Fernández, O. S., Cadenas-Pliego, G., Lira-Saldivar, R. H., & García-Cerda, L. A. (2014). Synthesis of copper nanoparticles by thermal decomposition and their antimicrobial properties. *Journal of Nanomaterials*, 2014.  
<https://doi.org/10.1155/2014/980545>

Bharathan, S., Sundaramoorthy, N. S., Chandrasekaran, H., Rangappa, G., ArunKumar, G., Subramaniyan, S. B., Veerappan, A., & Nagarajan, S. (2019). Sub lethal levels of platinum nanoparticle cures plasmid and in combination with carbapenem, curtails carbapenem resistant *Escherichia coli*. *Scientific Reports*, 9(1), 5305.  
<https://doi.org/10.1038/s41598-019-41489-3>

Bijesh, P., Selvaraj, V., & Andal, V. (2022). A review on synthesis and applications of nano metal Oxide/porous carbon composite. *Materials Today: Proceedings*, 55, 212–219.  
<https://doi.org/10.1016/j.matpr.2021.06.163>

Bikiaris, D. N., & Triantafyllidis, K. S. (2013). HDPE/Cu-nanofiber nanocomposites with enhanced antibacterial and oxygen barrier

properties appropriate for food packaging applications. *Materials Letters*, 93, 1–4. <https://doi.org/10.1016/j.matlet.2012.10.128>

Biswas, M. C., Tiimob, B. J., Abdela, W., Jeelani, S., & Rangari, V. K. (2019). Nano silica-carbon-silver ternary hybrid induced antimicrobial composite films for food packaging application. *Food Packaging and Shelf Life*, 19, 104–113. <https://doi.org/10.1016/j.fpsl.2018.12.003>

Bogdanović, U., Vodnik, V., Mitrić, M., Dimitrijević, S., Škapin, S. D., Žunić, V., Budimir, M., & Stoiljković, M. (2015). Nanomaterial with High Antimicrobial Efficacy—Copper/Polyaniline Nanocomposite. *ACS Applied Materials & Interfaces*, 7(3), 1955–1966. <https://doi.org/10.1021/am507746m>

Borkow, G., Zhou, S. S., Page, T., & Gabbay, J. (2010). A Novel Anti-Influenza Copper Oxide Containing Respiratory Face Mask. *PLoS ONE*, 5(6), e11295. <https://doi.org/10.1371/journal.pone.0011295>

Bott, J., Störmer, A., & Franz, R. (2014). A model study into the migration potential of nanoparticles from plastics nanocomposites for food contact. *Food Packaging and Shelf Life*, 2(2), 73–80. <https://doi.org/10.1016/j.fpsl.2014.08.001>

Boulanger, N., Kuzenkova, A. S., Iakunkov, A., Romanchuk, A. Yu., Trigub, A. L., Egorov, A. V., Bauters, S., Amidani, L., Retegan, M., Kvashnina, K. O., Kalmykov, S. N., & Talyzin, A. V. (2020). Enhanced Sorption of Radionuclides by Defect-Rich Graphene Oxide. *ACS Appl. Mater. Interfaces*, 12(40), 45122–45135. <https://doi.org/10.1021/acsami.0c11122>

Brewer, G. J. (2010). Risks of Copper and Iron Toxicity during Aging in Humans. *Chemical Research in Toxicology*, 23(2), 319–326. <https://doi.org/10.1021/tx900338d>

Cabernard, L., Pfister, S., Oberschelp, C., & Hellweg, S. (2022). Growing environmental footprint of plastics driven by coal combustion. *Nature Sustainability*, 5(2), 139–148. <https://doi.org/10.1038/s41893-021-00807-2>

Cabrini, A., Ghalayani Esfahani, A., Petraconi, A., Lavorgna, M., De Nardo, L., Buonocore, G. G., Andrade, R. J. E., & Cerruti, P. (2023). Ultrasonic spray deposition of PEGDE-crosslinked chitosan/graphene oxide coatings for enhancing gas barrier properties of polybutylene succinate films. *Progress in Organic Coatings*, 183, 107760. <https://doi.org/10.1016/j.porgcoat.2023.107760>

Cadogan, E. I., Lee, C. H., Popuri, S. R., & Lin, H. Y. (2014). Efficiencies of chitosan nanoparticles and crab shell particles in europium uptake from aqueous solutions through biosorption: Synthesis and characterization.

*International Biodeterioration and Biodegradation*, 95(PA).  
<https://doi.org/10.1016/j.ibiod.2014.06.003>

Camilleri, M. A., Cricelli, L., Mauriello, R., & Strazzullo, S. (2023). Consumer Perceptions of Sustainable Products: A Systematic Literature Review. *Sustainability*, 15(11), 8923.  
<https://doi.org/10.3390/su15118923>

Cano-Sarmiento, C., Alamilla-Beltrán, L., Azuara-Nieto, E., Hernández-Sánchez, H., Téllez-Medina, D. I., Jiménez-Martínez, C., & Gutiérrez-López, G. F. (2015). High Shear Methods to Produce Nano-sized Food Related to Dispersed Systems. In H. Hernández-Sánchez & G. F. Gutiérrez-López (Eds.), *Food Nanoscience and Nanotechnology* (pp. 145–161). Springer International Publishing.  
[https://doi.org/10.1007/978-3-319-13596-0\\_8](https://doi.org/10.1007/978-3-319-13596-0_8)

Chandrasekaran, S., Hur, S. H., Kim, E. J., Rajagopalan, B., Babu, K. F., Senthilkumar, V., Chung, J. S., Choi, W. M., & Kim, Y. S. (2015). Highly-ordered maghemite/reduced graphene oxide nanocomposites for high-performance photoelectrochemical water splitting. *RSC Advances*, 5(37), 29159–29166. <https://doi.org/10.1039/C5RA02934A>

Chaudhary, P., Fatima, F., & Kumar, A. (2020). Relevance of Nanomaterials in Food Packaging and its Advanced Future Prospects. *Journal of Inorganic and Organometallic Polymers and Materials*, 30(12), 5180–5192. <https://doi.org/10.1007/s10904-020-01674-8>

Chen, C. L., Wang, X. K., & Nagatsu, M. (2009). Europium Adsorption on Multiwall Carbon Nanotube/Iron Oxide Magnetic Composite in the Presence of Polyacrylic Acid. *Environ. Sci. Technol.*, 43(7), 2362–2367. <https://doi.org/10.1021/es803018a>

Cheng, S., & Grest, G. S. (2016). Dispersing Nanoparticles in a Polymer Film via Solvent Evaporation. *ACS Macro Letters*, 5(6), 694–698.  
<https://doi.org/10.1021/acsmacrolett.6b00263>

Choi, G., Kim, E., Park, E., & Lee, J. H. (2017). A cost-effective chemiluminescent biosensor capable of early diagnosing cancer using a combination of magnetic beads and platinum nanoparticles. *Talanta*, 162, 38–45. <https://doi.org/10.1016/j.talanta.2016.09.061>

Chokkareddy, R., Bhajanthri, N. K., Kabane, B., & Redhi, G. G. (2018). Bio-Sensing Performance of Magnetite Nanocomposite for Biomedical Applications. In S. Kanchi, S. Ahmed, M. I. Sabela, & C. M. Hussain (Eds.), *Nanomaterials: Biomedical, Environmental, and Engineering Applications* (1st ed., pp. 165–196). Wiley.  
<https://doi.org/10.1002/9781119370383.ch7>

Cioffi, N., Torsi, L., Ditaranto, N., Tantillo, G., Ghibelli, L., Sabbatini, L., Bleve-Zacheo, T., D'Alessio, M., Zambonin, P. G., & Traversa, E. (2005). Copper Nanoparticle/Polymer Composites with Antifungal and Bacteriostatic Properties. *Chem. Mater.*, 17(21), 5255–5262. <https://doi.org/10.1021/cm0505244>

Cushen, M., Kerry, J., Morris, M., Cruz-Romero, M., & Cummins, E. (2012). Nanotechnologies in the food industry – Recent developments, risks and regulation. *Trends in Food Science & Technology*, 24(1), 30–46. <https://doi.org/10.1016/j.tifs.2011.10.006>

Cushen, M., Kerry, J., Morris, M., Cruz-Romero, M., & Cummins, E. (2014). Evaluation and Simulation of Silver and Copper Nanoparticle Migration from Polyethylene Nanocomposites to Food and an Associated Exposure Assessment. *J. Agric. Food Chem.*, 62(6), 1403–1411. <https://doi.org/10.1021/jf404038y>

Dariane, A. B., & Azimi, Sh. (2016). Forecasting streamflow by combination of a genetic input selection algorithm and wavelet transforms using ANFIS models. *Hydrological Sciences Journal*, 61(3), 585–600. <https://doi.org/10.1080/02626667.2014.988155>

Das, P. E., Abu-Yousef, I. A., Majdalawieh, A. F., Narasimhan, S., & Poltronieri, P. (2020). Green Synthesis of Encapsulated Copper Nanoparticles Using a Hydroalcoholic Extract of *Moringa oleifera* Leaves and Assessment of Their Antioxidant and Antimicrobial Activities. *Molecules*, 25(3). <https://doi.org/10.3390/molecules25030555>

Dehghani, Z., Nguyen, T., Golabi, M., Hosseini, M., Rezayan, A. H., Mohammadnejad, J., Wolff, A., & Vinayaka, A. C. (2021). Magnetic beads modified with Pt/Pd nanoparticle and aptamer as a catalytic nano-bioprobe in combination with loop mediated isothermal amplification for the on-site detection of *Salmonella Typhimurium* in food and fecal samples. *Food Control*, 121, 107664. <https://doi.org/10.1016/j.foodcont.2020.107664>

Devlieghere, F., Vermeulen, A., & Debevere, J. (2004). Chitosan: antimicrobial activity, interactions with food components and applicability as a coating on fruit and vegetables. *Food Microbiology*, 21(6), 703–714. <https://doi.org/10.1016/j.fm.2004.02.008>

Dhillon, G. S., Kaur, S., & Brar, S. K. (2014). Facile fabrication and characterization of chitosan-based zinc oxide nanoparticles and evaluation of their antimicrobial and antibiofilm activity. *Int Nano Lett*, 4(2), 107. <https://doi.org/10.1007/s40089-014-0107-6>

Díaz-Cruz, C. A., Caicedo, C., Jiménez-Regalado, E. J., Díaz De León, R., López-González, R., & Aguirre-Loredo, R. Y. (2022). Evaluation of the Antimicrobial, Thermal, Mechanical, and Barrier Properties of Corn Starch–Chitosan Biodegradable Films Reinforced with Cellulose Nanocrystals. *Polymers*, 14(11), 2166. <https://doi.org/10.3390/polym14112166>

Dickson, D. P. E., & Berry, F. J. (1986). *Mössbauer Spectroscopy*. <https://ui.adsabs.harvard.edu/abs/1986mosp.book.....D>

Dinescu, S., Ionita, M., Pandele, A. M., Galateanu, B., Iovu, H., Ardelean, A., Costache, M., & Hermenean, A. (2014). In vitro cytocompatibility evaluation of chitosan/graphene oxide 3D scaffold composites designed for bone tissue engineering. *Bio-Medical Materials and Engineering*, 24(6), 2249–2256. <https://doi.org/10.3233/BME-141037>

Dobrucka, R., & Ankiel, M. (2019). Possible applications of metal nanoparticles in antimicrobial food packaging. *Journal of Food Safety*, 39(2), e12617. <https://doi.org/10.1111/jfs.12617>

Dolatabadi, M., Mehrabpour, M., Esfandyari, M., Alidadi, H., & Davoudi, M. (2018). Modeling of simultaneous adsorption of dye and metal ion by sawdust from aqueous solution using of ANN and ANFIS. *Chemometrics and Intelligent Laboratory Systems*, 181, 72–78. <https://doi.org/10.1016/j.chemolab.2018.07.012>

dos Santos, C. A., Ingle, A. P., & Rai, M. (2020). The emerging role of metallic nanoparticles in food. *Applied Microbiology and Biotechnology*, 104(6), 2373–2383. <https://doi.org/10.1007/s00253-020-10372-x>

Dreyer, D. R., Park, S., Bielawski, C. W., & Ruoff, R. S. (2009). The chemistry of graphene oxide. *Chemical Society Reviews*, 39(1), 228–240. <https://doi.org/10.1039/B917103G>

Ebrahimiasl, S., & Rajabpour, A. (2015). Synthesis and characterization of novel bactericidal Cu/HPMC BNCs using chemical reduction method for food packaging. *Journal of Food Science and Technology*, 52(9), 5982–5988. <https://doi.org/10.1007/s13197-014-1615-0>

EFSA Scientific Committee, More, S. J., Bampidis, V., Benford, D., Bragard, C., Halldorsson, T. I., Hernández-Jerez, A. F., Hougaard Bennekou, S., Koutsoumanis, K. P., Machera, K., Naegeli, H., Nielsen, S. S., Schlatter, J. R., Schrenk, D., Silano, V., Turck, D., Younes, M., Gundert-Remy, U., Kass, G. E. N., ... Wallace, H. M. (2019). Guidance on the use of the Threshold of Toxicological Concern approach in food safety assessment. *EFSA Journal. European Food*

*Safety Authority*, 17(6), e05708.  
<https://doi.org/10.2903/j.efsa.2019.5708>

El Rouby, W. M. A., Farghali, A. A., Sadek, M. A., & Khalil, W. F. (2018). Fast Removal of Sr(II) From Water by Graphene Oxide and Chitosan Modified Graphene Oxide. *Journal of Inorganic and Organometallic Polymers and Materials*, 28(6), 2336–2349.  
<https://doi.org/10.1007/s10904-018-0885-9>

El-Shazly, E. A. A., Moussa, S. I., & Dakroury, G. A. (2022). Recovery of Some Rare-Earth Elements by Sorption Technique onto Graphene Oxide. *Journal of Sustainable Metallurgy*, 8(2), 715–731.  
<https://doi.org/10.1007/s40831-022-00520-0>

Emadi, F., Amini, A., Gholami, A., & Ghasemi, Y. (2017). Functionalized Graphene Oxide with Chitosan for Protein Nanocarriers to Protect against Enzymatic Cleavage and Retain Collagenase Activity. *Scientific Reports*, 7. <https://doi.org/10.1038/srep42258>

Emiru, T. F., & Ayele, D. W. (2017). Controlled synthesis, characterization and reduction of graphene oxide: A convenient method for large scale production. *Egyptian Journal of Basic and Applied Sciences*, 4(1).  
<https://doi.org/10.1016/j.ejbas.2016.11.002>

Espírito Santo, C., Lam, E. W., Elowsky, C. G., Quaranta, D., Domaille, D. W., Chang, C. J., & Grass, G. (2011). Bacterial killing by dry metallic copper surfaces. *Appl Environ Microbiol*, 77(3), 794–802.  
<https://doi.org/10.1128/AEM.01599-10>

Etale, A., Tutu, H., & Drake, D. C. (2016). Application of maghemite nanoparticles as sorbents for the removal of Cu(II), Mn(II) and U(VI) ions from aqueous solution in acid mine drainage conditions. *Appl Water Sci*, 6(2), 187–197. <https://doi.org/10.1007/s13201-014-0217-3>

Fernandes Queiroz, M., Melo, K. R. T., Sabry, D. A., Sasaki, G. L., & Rocha, H. A. O. (2015). Does the Use of Chitosan Contribute to Oxalate Kidney Stone Formation? *Marine Drugs*, 13(1), 141–158.  
<https://doi.org/10.3390/md13010141>

Fernández, A., Picouet, P., & Lloret, E. (2010). Reduction of the spoilage-related microflora in absorbent pads by silver nanotechnology during modified atmosphere packaging of beef meat. *Journal of Food Protection*, 73(12), 2263–2269. <https://doi.org/10.4315/0362-028x-73.12.2263>

Ferreira, F. N., Benevides, A. P., Cesar, D. V., Luna, A. S., & de Gois, J. S. (2020). Magnetic solid-phase extraction and pre-concentration of 17 $\beta$ -estradiol and 17 $\alpha$ -ethinylestradiol in tap water using maghemite-graphene oxide nanoparticles and determination via HPLC with a

fluorescence detector. *Microchemical Journal*, 157, 104947. <https://doi.org/10.1016/j.microc.2020.104947>

Figiel, M., Wysokowski, M., Galinski, M., Jesionowski, T., & Stepienak, I. (2018). Synthesis and characterization of novel copper oxide-chitosan nanocomposites for non-enzymatic glucose sensing. *Sensors and Actuators, B: Chemical*, 272. <https://doi.org/10.1016/j.snb.2018.05.173>

Foster, R. I., Amphlett, J. T. M., Kim, K.-W., Kerry, T., Lee, K., & Sharrad, C. A. (2020). SOHIO process legacy waste treatment: Uranium recovery using ion exchange. *Journal of Industrial and Engineering Chemistry*, 81, 144–152. <https://doi.org/10.1016/j.jiec.2019.09.001>

Gaim, Tesfamariam, Nigussie, & Ashebir. (2019). Synthesis, Characterization and Photocatalytic Activity of N-doped Cu<sub>2</sub>O/ZnO Nanocomposite on Degradation of Methyl Red. *Journal of Composites Science*, 3(4), 93. <https://doi.org/10.3390/jcs3040093>

Galotto, M. J., Ulloa, P. a, Hernández, D., Fernández-Martín, F., Gavara, R., & Guarda, A. (2008). Mechanical and thermal behaviour of flexible food packaging polymeric films materials under high pressure/temperature treatments. *Packaging Technology and Science*, 21(5), 297–308. <https://doi.org/10.1002/pts.807>

Ganachari, S. V., Hublikar, L., Yaradoddi, J. S., & Math, S. S. (2019). Metal Oxide Nanomaterials for Environmental Applications. In L. M. T. Martínez, O. V. Kharissova, & B. I. Kharisov (Eds.), *Handbook of Ecomaterials* (pp. 2357–2368). Springer International Publishing. [https://doi.org/10.1007/978-3-319-68255-6\\_196](https://doi.org/10.1007/978-3-319-68255-6_196)

Geyer, R., Jambeck, J. R., & Law, K. L. (2017). Production, use, and fate of all plastics ever made. *Science Advances*, 3(7), e1700782. <https://doi.org/10.1126/sciadv.1700782>

Gopinath, K., Sathishkumar, G., & Xu, L. (2024). An Overview of the Copper Oxide Nanofillers Integrated in Food Packaging Systems. In *Coatings* (Vol. 14, Issue 1). <https://doi.org/10.3390/coatings14010081>

Gordon, T., Perlstein, B., Houbara, O., Felner, I., Banin, E., & Margel, S. (2011). Synthesis and characterization of zinc/iron oxide composite nanoparticles and their antibacterial properties. *Colloids and Surfaces A: Physicochemical and Engineering Aspects*, 374(1–3), 1–8. <https://doi.org/10.1016/j.colsurfa.2010.10.015>

Goyal, N., Gao, P., Wang, Z., Cheng, S., Ok, Y. S., Li, G., & Liu, L. (2020). Nanostructured chitosan/molecular sieve-4A an emergent material for the synergistic adsorption of radioactive major pollutants cesium and strontium. *Journal of Hazardous Materials*, 392, 122494. <https://doi.org/10.1016/j.jhazmat.2020.122494>

Grande-Tovar, C. D., Chaves-Lopez, C., Serio, A., Rossi, C., & Paparella, A. (2018). Chitosan coatings enriched with essential oils: Effects on fungi involved in fruit decay and mechanisms of action. *Trends in Food Science & Technology*, 78, 61–71.  
<https://doi.org/10.1016/j.tifs.2018.05.019>

Grass, G., Rensing, C., & Solioz, M. (2011). Metallic Copper as an Antimicrobial Surface. *Applied and Environmental Microbiology*, 77(5), 1541–1547. <https://doi.org/10.1128/AEM.02766-10>

Gumienna, M., & Górná, B. (2021). Antimicrobial Food Packaging with Biodegradable Polymers and Bacteriocins. *Molecules*, 26(12), 3735. <https://doi.org/10.3390/molecules26123735>

Guo, Y., Dai, M., Zhu, Z., Chen, Y., He, H., & Qin, T. (2019). Chitosan modified Cu<sub>2</sub>O nanoparticles with high catalytic activity for p-nitrophenol reduction. *Applied Surface Science*, 480.  
<https://doi.org/10.1016/j.apsusc.2019.02.246>

Gurunathan, S., Han, J. W., Dayem, A. A., Eppakayala, V., & Kim, J.-H. (2012). Oxidative stress-mediated antibacterial activity of graphene oxide and reduced graphene oxide in *Pseudomonas aeruginosa*. *International Journal of Nanomedicine*, 7, 5901–5914.  
<https://doi.org/10.2147/IJN.S37397>

Gvozdenko, A. A., Siddiqui, S. A., Blinov, A. V., Golik, A. B., Nagdalian, A. A., Maglakelidze, D. G., Statsenko, E. N., Pirogov, M. A., Blinova, A. A., Sizonenko, M. N., Simonov, A. N., Zhukov, R. B., Kolesnikov, R. O., & Ibrahim, S. A. (2022). Synthesis of CuO nanoparticles stabilized with gelatin for potential use in food packaging applications. *Scientific Reports*, 12(1), 12843. <https://doi.org/10.1038/s41598-022-16878-w>

Hafsa, J., Smach, M. ali, Ben Khedher, M. R., Charfeddine, B., Limem, K., Majdoub, H., & Rouatbi, S. (2016). Physical, antioxidant and antimicrobial properties of chitosan films containing *Eucalyptus globulus* essential oil. *LWT - Food Science and Technology*, 68, 356–364. <https://doi.org/10.1016/j.lwt.2015.12.050>

Hamza, M. F., Roux, J.-C., & Guibal, E. (2018). Uranium and europium sorption on amidoxime-functionalized magnetic chitosan micro-particles. *Chemical Engineering Journal*, 344, 124–137.  
<https://doi.org/10.1016/j.cej.2018.03.029>

Han Lyn, F., Chin Peng, T., Ruzniza, M. Z., & Nur Hanani, Z. A. (2019). Effect of oxidation degrees of graphene oxide (GO) on the structure and physical properties of chitosan/GO composite films. *Food Packaging and Shelf Life*, 21, 100373.  
<https://doi.org/10.1016/j.fpsl.2019.100373>

Hannon, J. C., Kerry, J. P., Cruz-Romero, M., Azlin-Hasim, S., Morris, M., & Cummins, E. (2016). Human exposure assessment of silver and copper migrating from an antimicrobial nanocoated packaging material into an acidic food simulant. *Food and Chemical Toxicology*, 95, 128–136. <https://doi.org/10.1016/j.fct.2016.07.004>

Hans, M., Erbe, A., Mathews, S., Chen, Y., Solioz, M., & Mücklich, F. (2013). Role of Copper Oxides in Contact Killing of Bacteria. *Langmuir*, 29(52), 16160–16166. <https://doi.org/10.1021/la404091z>

Hans, M., Mathews, S., Mücklich, F., & Solioz, M. (2015). Physicochemical properties of copper important for its antibacterial activity and development of a unified model. *Biointerphases*, 11(1), 18902. <https://doi.org/10.1116/1.4935853>

Hara, M., Kondo, T., Komoda, M., Ikeda, S., Kondo, J. N., Domen, K., Hara, M., Shinohara, K., & Tanaka, A. (1998). Cu<sub>2</sub>O as a photocatalyst for overall water splitting under visible light irradiation. *Chem. Commun.*, 3, 357–358. <https://doi.org/10.1039/A707440I>

Hirose, K. (2016). Fukushima Daiichi Nuclear Plant accident: Atmospheric and oceanic impacts over the five years. *Journal of Environmental Radioactivity*, 157, 113–130. <https://doi.org/10.1016/j.jenvrad.2016.01.011>

Hopewell, J., Dvorak, R., & Kosior, E. (2009). Plastics recycling: challenges and opportunities. *Philosophical Transactions of the Royal Society B: Biological Sciences*, 364(1526), 2115–2126. <https://doi.org/10.1098/rstb.2008.0311>

Hosseini, R., Ahari, H., Mahasti, P., & Paidari, S. (2017). Measuring the migration of silver from silver nanocomposite polyethylene packaging based on (TiO<sub>2</sub>) into Penaeus semisulcatus using titration comparison with migration methods. *Fisheries Science*, 83(4), 649–659. <https://doi.org/10.1007/s12562-017-1090-4>

Hosseini, S. M., Mazinani, S., Abdouss, M., Kalhor, H., Kalantari, K., Amiri, I. S., & Ramezani, Z. (2022). Designing chitosan nanoparticles embedded into graphene oxide as a drug delivery system. *Polymer Bulletin*, 79(1). <https://doi.org/10.1007/s00289-020-03506-8>

Hou, X., Xue, Z., Xia, Y., Qin, Y., Zhang, G., Liu, H., & Li, K. (2019). Effect of SiO<sub>2</sub> nanoparticle on the physical and chemical properties of eco-friendly agar/sodium alginate nanocomposite film. *International Journal of Biological Macromolecules*, 125, 1289–1298. <https://doi.org/10.1016/j.ijbiomac.2018.09.109>

Huang, X., Qi, X., Boey, F., & Zhang, H. (2012). Graphene-based composites. *Chemical Society Reviews*, 41(2), 666–686.  
<https://doi.org/10.1039/C1CS15078B>

Huang, Z.-W., Li, Z.-J., Zheng, L.-R., Wu, W.-S., Chai, Z.-F., & Shi, W.-Q. (2019a). Adsorption of Eu(III) and Th(IV) on three-dimensional graphene-based macrostructure studied by spectroscopic investigation. *Environmental Pollution*, 248, 82–89.  
<https://doi.org/10.1016/j.envpol.2019.01.050>

Huang, Z.-W., Li, Z.-J., Zheng, L.-R., Wu, W.-S., Chai, Z.-F., & Shi, W.-Q. (2019b). Adsorption of Eu(III) and Th(IV) on three-dimensional graphene-based macrostructure studied by spectroscopic investigation. *Environmental Pollution*, 248, 82–89.  
<https://doi.org/10.1016/j.envpol.2019.01.050>

Hwang, S. Y., Yoo, E. S., & Im, S. S. (2012). The synthesis of copolymers, blends and composites based on poly(butylene succinate). *Polymer Journal*, 44(12), 1179–1190. <https://doi.org/10.1038/pj.2012.157>

Ikeda, S., Takata, T., Kondo, T., Hitoki, G., Hara, M., Kondo, J. N., Domen, K., Hosono, H., Kawazoe, H., & Tanaka, A. (1998). Mechano-catalytic overall water splitting. *Chemical Communications*, 20, 2185–2186.  
<https://doi.org/10.1039/A804549F>

Imawan, C., Yunilawati, R., Fauzia, V., Rahmi, D., & Umar, A. (2022). Physical and Mechanical Properties of Antimicrobial Film Form Lemongrass Oil Incorporated with Chitosan/Ascorbic Acid. *Proceedings of the Conference on Broad Exposure to Science and Technology 2021 (BEST 2021)*, 210.  
<https://doi.org/10.2991/aer.k.220131.056>

Ioniță, M., Vlăsceanu, G. M., Watzlawek, A. A., Voicu, S. I., Burns, J. S., & Iovu, H. (2017). Graphene and functionalized graphene: Extraordinary prospects for nanobiocomposite materials. *Composites Part B: Engineering*, 121, 34–57.  
<https://doi.org/10.1016/j.compositesb.2017.03.031>

Jang, J.-S. R. (1993). ANFIS: adaptive-network-based fuzzy inference system. *IEEE Trans. Syst., Man, Cybern.*, 23(3), 665–685.  
<https://doi.org/10.1109/21.256541>

Jaramillo, A. F., Riquelme, S. A., Sánchez-Sanhueza, G., Medina, C., Solís-Pomar, F., Rojas, D., Montalba, C., Melendrez, M. F., & Pérez-Tijerina, E. (2019). Comparative Study of the Antimicrobial Effect of Nanocomposites and Composite Based on Poly(butylene adipate-co-terephthalate) Using Cu and Cu/Cu<sub>2</sub>O Nanoparticles and CuSO<sub>4</sub>.

*Nanoscale Research Letters*, 14(1), 158.  
<https://doi.org/10.1186/s11671-019-2987-x>

Jayaramudu, T., Varaprasad, K., Pyarasani, R. D., Reddy, K. K., Kumar, K. D., Akbari-Fakhrebadi, A., Mangalaraja, R. V., & Amalraj, J. (2019). Chitosan capped copper oxide/copper nanoparticles encapsulated microbial resistant nanocomposite films. *International Journal of Biological Macromolecules*, 128.  
<https://doi.org/10.1016/j.ijbiomac.2019.01.145>

Jia, W., Wang, L., Xu, Y., Wen, X., Ma, X., & Cui, Z. (2022). Study on the actuation characteristics of a graphene oxide-modified biological gel electroactive actuator. *Journal of Applied Polymer Science*, 139(46), e53247. <https://doi.org/10.1002/app.53247>

Jiang, Y., Gong, J.-L., Zeng, G.-M., Ou, X.-M., Chang, Y.-N., Deng, C.-H., Zhang, J., Liu, H.-Y., & Huang, S.-Y. (2016). Magnetic chitosan-graphene oxide composite for anti-microbial and dye removal applications. *International Journal of Biological Macromolecules*, 82, 702–710. <https://doi.org/10.1016/j.ijbiomac.2015.11.021>

Johra, F. T., Lee, J.-W., & Jung, W.-G. (2014). Facile and safe graphene preparation on solution based platform. *Journal of Industrial and Engineering Chemistry*, 20(5), 2883–2887.  
<https://doi.org/10.1016/j.jiec.2013.11.022>

Kalia, A., Kaur, M., Shami, A., Jawandha, S. K., Alghuthaymi, M. A., Thakur, A., & Abd-Elsalam, K. A. (2021). Nettle-Leaf Extract Derived ZnO/CuO Nanoparticle-Biopolymer-Based Antioxidant and Antimicrobial Nanocomposite Packaging Films and Their Impact on Extending the Post-Harvest Shelf Life of Guava Fruit. *Biomolecules*, 11(2), 224. <https://doi.org/10.3390/biom11020224>

Kalubowila, K. D. R. N., Gunewardene, M. S., Jayasingha, J. L. K., Dissanayake, D., Jayathilaka, C., Jayasundara, J. M. D., Gao, Y., & Jayanetti, J. K. D. S. (2021). Reduction-Induced Synthesis of Reduced Graphene Oxide-Wrapped Cu<sub>2</sub>O/Cu Nanoparticles for Photodegradation of Methylene Blue. *ACS Applied Nano Materials*, 4(3). <https://doi.org/10.1021/acsanm.0c03320>

Kanted, D., Soman, V., Sahota, S., & Poddar, M. K. (2023). Development of hybrid chitosan/zinc oxide/graphene oxide nanocomposites for potential food packaging application. *International Journal of Sustainable Building Tech*, 14(1), 96–110.  
<https://doi.org/10.22712/susb.20230008>

Keihan, A. H., Veisi, H., & Veasi, H. (2017). Green synthesis and characterization of spherical copper nanoparticles as organometallic

antibacterial agent. *Applied Organometallic Chemistry*, 31(7), e3642. <https://doi.org/10.1002/aoc.3642>

Khan, A. A. P., Khan, A., Asiri, A. M., Ashraf, G. M., & Alhoggbia, B. G. (2017). Graphene Oxide Based Metallic Nanoparticles and their Some Biological and Environmental Application. *Current Drug Metabolism*, 18(11), 1020–1029. <https://doi.org/10.2174/1389200218666171016100507>

Khan, A., Rashid, A., Younas, R., & Chong, R. (2016). A chemical reduction approach to the synthesis of copper nanoparticles. *International Nano Letters*, 6(1). <https://doi.org/10.1007/s40089-015-0163-6>

Khan, S. B., Ali, F., & Akhtar, K. (2019). Chitosan nanocomposite fibers supported copper nanoparticles based perceptive sensor and active catalyst for nitrophenol in real water. *Carbohydrate Polymers*, 207. <https://doi.org/10.1016/j.carbpol.2018.12.032>

Khashan, K. S., Sulaiman, G. M., & Abdulameer, F. A. (2016). Synthesis and Antibacterial Activity of CuO Nanoparticles Suspension Induced by Laser Ablation in Liquid. *Arabian Journal for Science and Engineering*, 41(1), 301–310. <https://doi.org/10.1007/s13369-015-1733-7>

Khouri, J., Penlidis, A., & Moresoli, C. (2019). Viscoelastic Properties of Crosslinked Chitosan Films. *Processes*, 7(3), 157. <https://doi.org/10.3390/pr7030157>

Kim, D.-W., Shchipunov, Y., Kim, G.-H., Shin, I., & Ha, C.-S. (2020). Effect of graphene oxide content on the tensile properties and swelling ratio of chitosan/xanthan gum/graphene oxide hydrogel films. *Molecular Crystals and Liquid Crystals*, 706(1), 72–78. <https://doi.org/10.1080/15421406.2020.1743440>

Kolwas, K., & Derkachova, A. (2020). Impact of the Interband Transitions in Gold and Silver on the Dynamics of Propagating and Localized Surface Plasmons. *Nanomaterials*, 10(7), 1411. <https://doi.org/10.3390/nano10071411>

Koontz, J. L., Liggans, G. L., & Redan, B. W. (2020). Temperature and pH affect copper release kinetics from copper metal foil and commercial copperware to food simulants. *Food Additives & Contaminants: Part A*, 37(3), 465–477. <https://doi.org/10.1080/19440049.2019.1704447>

Košiček, M., Zavašnik, J., Baranov, O., Šetina Batič, B., & Cvelbar, U. (2022). Understanding the Growth of Copper Oxide Nanowires and Layers by Thermal Oxidation over a Broad Temperature Range at

Atmospheric Pressure. *Crystal Growth & Design*, 22(11), 6656–6666.  
<https://doi.org/10.1021/acs.cgd.2c00863>

Kumar, A. S. K., & Jiang, S. J. (2016). Chitosan-functionalized graphene oxide: A novel adsorbent an efficient adsorption of arsenic from aqueous solution. *Journal of Environmental Chemical Engineering*, 4(2). <https://doi.org/10.1016/j.jece.2016.02.035>

Kumar, S., & Koh, J. (2014). Physicochemical and optical properties of chitosan based graphene oxide bionanocomposite. *International Journal of Biological Macromolecules*, 70.  
<https://doi.org/10.1016/j.ijbiomac.2014.07.019>

Kumar, S., Mukherjee, A., & Dutta, J. (2020). Chitosan based nanocomposite films and coatings: Emerging antimicrobial food packaging alternatives. *Trends in Food Science & Technology*, 97, 196–209. <https://doi.org/10.1016/j.tifs.2020.01.002>

Kuzenkova, A. S., Romanchuk, A. Y., Trigub, A. L., Maslakov, K. I., Egorov, A. V., Amidani, L., Kittrell, C., Kvashnina, K. O., Tour, J. M., Talyzin, A. V., & Kalmykov, S. N. (2020). New insights into the mechanism of graphene oxide and radionuclide interaction. *Carbon*, 158, 291–302. <https://doi.org/10.1016/j.carbon.2019.10.003>

Laurent, S., Forge, D., Port, M., Roch, A., Robic, C., Vander Elst, L., & Muller, R. N. (2008). Magnetic Iron Oxide Nanoparticles: Synthesis, Stabilization, Vectorization, Physicochemical Characterizations, and Biological Applications. *Chemical Reviews*, 108(6), 2064–2110.  
<https://doi.org/10.1021/cr068445e>

Li, Y., Sheng, G., & Sheng, J. (2014). Magnetite decorated graphene oxide for the highly efficient immobilization of Eu(III) from aqueous solution. *Journal of Molecular Liquids*, 199, 474–480.  
<https://doi.org/10.1016/j.molliq.2014.08.009>

Li, Z., Lin, S., An, S., Liu, L., Hu, Y., & Wan, L. (2019). Preparation, characterization and anti-aflatoxigenic activity of chitosan packaging films incorporated with turmeric essential oil. *International Journal of Biological Macromolecules*, 131, 420–434.  
<https://doi.org/10.1016/j.ijbiomac.2019.02.169>

Liang, J., Wang, R., & Chen, R. (2019). The Impact of Cross-linking Mode on the Physical and Antimicrobial Properties of a Chitosan/Bacterial Cellulose Composite. *Polymers*, 11(3), 491.  
<https://doi.org/10.3390/polym11030491>

Lim, J. Y., Mubarak, N. M., Abdullah, E. C., Nizamuddin, S., Khalid, M., & Inamuddin. (2018). Recent trends in the synthesis of graphene and graphene oxide based nanomaterials for removal of heavy metals — A

review. *Journal of Industrial and Engineering Chemistry*, 66, 29–44. <https://doi.org/10.1016/j.jiec.2018.05.028>

Lingamdinne, L. P., Koduru, J. R., & Karri, R. R. (2019). A comprehensive review of applications of magnetic graphene oxide based nanocomposites for sustainable water purification. *Journal of Environmental Management*, 231, 622–634. <https://doi.org/10.1016/j.jenvman.2018.10.063>

Liu, F., Hu, C.-Y., Zhao, Q., Shi, Y.-J., & Zhong, H.-N. (2016a). Migration of copper from nanocopper/LDPE composite films. *Food Additives & Contaminants: Part A*, 33(11), 1741–1749. <https://doi.org/10.1080/19440049.2016.1237779>

Liu, F., Hu, C.-Y., Zhao, Q., Shi, Y.-J., & Zhong, H.-N. (2016b). Migration of copper from nanocopper/LDPE composite films. *Food Additives & Contaminants: Part A*, 33(11), 1741–1749. <https://doi.org/10.1080/19440049.2016.1237779>

Liu, L., Li, C., Bao, C., Jia, Q., Xiao, P., Liu, X., & Zhang, Q. (2012). Preparation and characterization of chitosan/graphene oxide composites for the adsorption of Au(III) and Pd(II). *Talanta*, 93. <https://doi.org/10.1016/j.talanta.2012.02.051>

Liu, S., Li, Y., Yan, J., Zhou, Y., Liu, C., Zuo, Y., & Liu, D. (2021). Effective removal of ruthenium(III) ions from wastewater by xanthate-modified cross-linked chitosan. *Journal of Environmental Chemical Engineering*, 9(2), 104818. <https://doi.org/10.1016/j.jece.2020.104818>

Llorens, A., Lloret, E., Picouet, P., & Fernandez, A. (2012). Study of the antifungal potential of novel cellulose/copper composites as absorbent materials for fruit juices. *International Journal of Food Microbiology*, 158(2), 113–119. <https://doi.org/10.1016/j.ijfoodmicro.2012.07.004>

López-Díaz, D., López Holgado, M., García-Fierro, J. L., & Velázquez, M. M. (2017). Evolution of the Raman Spectrum with the Chemical Composition of Graphene Oxide. *J. Phys. Chem. C*, 121(37), 20489–20497. <https://doi.org/10.1021/acs.jpcc.7b06236>

Luckachan, G. E., & Pillai, C. K. S. (2011). Biodegradable Polymers- A Review on Recent Trends and Emerging Perspectives. *Journal of Polymers and the Environment*, 19(3), 637–676. <https://doi.org/10.1007/s10924-011-0317-1>

Lujanienė, G., Novikau, R., Karalevičiūtė, K., Pakštas, V., Talaikis, M., Levinskaitė, L., Selskienė, A., Selskis, A., Mažeika, J., & Jokšas, K. (2024). Chitosan-minerals-based composites for adsorption of caesium, cobalt and europium. *Journal of Hazardous Materials*, 462, 132747. <https://doi.org/10.1016/j.jhazmat.2023.132747>

Lujanienė, G., Šemčuk, S., Kulakauskaitė, I., Mažeika, K., Valiulis, D., Juškėnas, R., & Tautkus, S. (2016). Sorption of radionuclides and metals to graphene oxide and magnetic graphene oxide. *Journal of Radioanalytical and Nuclear Chemistry*, 307(3), 2267–2275.  
<https://doi.org/10.1007/s10967-015-4461-2>

Lujanienė, G., Šemčuk, S., Lečinskytė, A., Kulakauskaitė, I., Mažeika, K., Valiulis, D., Pakštas, V., Skapas, M., & Tumėnas, S. (2017). Magnetic graphene oxide based nano-composites for removal of radionuclides and metals from contaminated solutions. *Journal of Environmental Radioactivity*, 166, 166–174.  
<https://doi.org/10.1016/j.jenvrad.2016.02.014>

Lupan, O., Postica, V., Cretu, V., Wolff, N., Duppel, V., Kienle, L., & Adelung, R. (2016). Single and networked CuO nanowires for highly sensitive p-type semiconductor gas sensor applications. *Physica Status Solidi (RRL) - Rapid Research Letters*, 10(3), 260–266.  
<https://doi.org/10.1002/pssr.201510414>

Lv, S., Li, M., Wu, X., Zhang, X., Hua, Y., Bi, L., Fang, Q., & Cai, T. (2021). A non-polluting method for rapidly purifying uranium-containing wastewater and efficiently recovering uranium through electrochemical mineralization and oxidative roasting. *Journal of Hazardous Materials*, 416, 125885.  
<https://doi.org/10.1016/j.jhazmat.2021.125885>

Ma, J., Zhao, Q., Zhou, L., Wen, T., & Wang, J. (2019). Mutual effects of U(VI) and Eu(III) immobilization on interpenetrating 3-dimensional MnO<sub>2</sub>/graphene oxide composites. *Science of The Total Environment*, 695, 133696. <https://doi.org/10.1016/j.scitotenv.2019.133696>

Madigan, M. T., Bender, K. S., Buckley, D. H., Sattley, W. M., & Stahl, D. A. (2018). *Brock biology of microorganisms* (Fifteenth edition). Pearson.

Mahmoud, M. E., Khalifa, M. A., El Wakeel, Y. M., Header, M. S., & Abdel-Fattah, T. M. (2017). Engineered nano-magnetic iron oxide-urea-activated carbon nanolayer sorbent for potential removal of uranium (VI) from aqueous solution. *Journal of Nuclear Materials*, 487, 13–22. <https://doi.org/10.1016/j.jnucmat.2017.01.046>

Malka, E., Perelshtain, I., Lipovsky, A., Shalom, Y., Naparstek, L., Perkas, N., Patick, T., Lubart, R., Nitzan, Y., Banin, E., & Gedanken, A. (2013). Eradication of Multi-Drug Resistant Bacteria by a Novel Zn-doped CuO Nanocomposite. *Small*, 9(23), 4069–4076.  
<https://doi.org/10.1002/smll.201301081>

Matthews, C., Moran, F., & Jaiswal, A. K. (2021). A review on European Union's strategy for plastics in a circular economy and its impact on food safety. *Journal of Cleaner Production*, 283, 125263.  
<https://doi.org/10.1016/j.jclepro.2020.125263>

Merino, D., & A. Alvarez, V. (2019). In-soil Biodegradation Behavior of Chitosan-Coated Phosphorylated Starch Films. *Advanced Materials Letters*, 10(12), 907–912. <https://doi.org/10.5185/amlett.2019.0017>

Mesgari, M., Aalami, A. H., Sathyapalan, T., & Sahebkar, A. (2022a). A Comprehensive Review of the Development of Carbohydrate Macromolecules and Copper Oxide Nanocomposite Films in Food Nanopackaging. *Bioinorganic Chemistry and Applications*, 2022, 1–28.  
<https://doi.org/10.1155/2022/7557825>

Mesgari, M., Aalami, A. H., Sathyapalan, T., & Sahebkar, A. (2022b). A Comprehensive Review of the Development of Carbohydrate Macromolecules and Copper Oxide Nanocomposite Films in Food Nanopackaging. *Bioinorganic Chemistry and Applications*, 2022, 1–28.  
<https://doi.org/10.1155/2022/7557825>

Minitha, C. R., Suresh, R., Maity, U. K., Haldorai, Y., Subramaniam, V., Manoravi, P., Joseph, M., & Rajendra Kumar, R. T. (2018). Magnetite Nanoparticle Decorated Reduced Graphene Oxide Composite as an Efficient and Recoverable Adsorbent for the Removal of Cesium and Strontium Ions. *Industrial & Engineering Chemistry Research*, 57(4), 1225–1232. <https://doi.org/10.1021/acs.iecr.7b05340>

Mohamed, E. A. (2020). Green synthesis of copper & copper oxide nanoparticles using the extract of seedless dates. *Helijon*, 6(1).  
<https://doi.org/10.1016/j.heliyon.2019.e03123>

Mohan, C. O., Gunasekaran, S., & Ravishankar, C. N. (2019). Chitosan-capped gold nanoparticles for indicating temperature abuse in frozen stored products. *Npj Sci Food*, 3(1), 2. <https://doi.org/10.1038/s41538-019-0034-z>

Mohanty, B. N., Yuvaraj, R., Jena, H., & Ponraju, D. (2022). Graphene Oxide as an Adsorbent for Ruthenium from Aqueous Solution. *ChemistrySelect*, 7(14), e202200078.  
<https://doi.org/10.1002/slct.202200078>

Morin, G., Ona-Nguema, G., Wang, Y., Menguy, N., Juillot, F., Proux, O., Guyot, F., Calas, G., & Brown Jr., G. E. (2008). Extended X-ray Absorption Fine Structure Analysis of Arsenite and Arsenate Adsorption on Maghemite. *Environ. Sci. Technol.*, 42(7), 2361–2366.  
<https://doi.org/10.1021/es072057s>

Mørup, S., & Tronc, E. (1994). Superparamagnetic relaxation of weakly interacting particles. *Physical Review Letters*, 72(20), 3278–3281. <https://doi.org/10.1103/PhysRevLett.72.3278>

Mrkić, S., Galić, K., Ivanković, M., Hamin, S., & Ciković, N. (2006). Gas transport and thermal characterization of mono- and di-polyethylene films used for food packaging. *Journal of Applied Polymer Science*, 99(4), 1590–1599. <https://doi.org/10.1002/app.22513>

Muncke, J. (2016). Chemical Migration from Food Packaging to Food. In *Reference Module in Food Science*. Elsevier. <https://doi.org/10.1016/B978-0-08-100596-5.03311-4>

Musella, E., Ouazzani, I. C. El, Mendes, A. R., Rovera, C., Farris, S., Mena, C., Teixeira, P., & Poças, F. (2021). Preparation and Characterization of Bioactive Chitosan-Based Films Incorporated with Olive Leaves Extract for Food Packaging Applications. *Coatings*, 11(11), 1339. <https://doi.org/10.3390/coatings11111339>

Nabipour, N., Mosavi, A., Hajnal, E., Nadai, L., Shamshirband, S., & Chau, K.-W. (2020). Modeling climate change impact on wind power resources using adaptive neuro-fuzzy inference system. *Engineering Applications of Computational Fluid Mechanics*, 14(1), 491–506. <https://doi.org/10.1080/19942060.2020.1722241>

Nasrollahzadeh, M., Ghorbannezhad, F., Issaabadi, Z., & Sajadi, S. M. (2019). Recent Developments in the Biosynthesis of Cu-Based Recyclable Nanocatalysts Using Plant Extracts and their Application in the Chemical Reactions. *The Chemical Record*, 19(2–3), 601–643. <https://doi.org/10.1002/tcr.201800069>

Nath, A., Mthethwa, F., & Saha, G. (2019). Runoff estimation using modified adaptive neuro-fuzzy inference system. *Environmental Engineering Research*, 25(4), 545–553. <https://doi.org/10.4491/eer.2019.166>

No, H. K., Meyers, S. P., Prinyawiwatkul, W., & Xu, Z. (2007). Applications of chitosan for improvement of quality and shelf life of foods: A review. In *Journal of Food Science* (Vol. 72, Issue 5). <https://doi.org/10.1111/j.1750-3841.2007.00383.x>

Nouri, A., Yaraki, M. T., Ghorbanpour, M., Agarwal, S., & Gupta, V. K. (2018a). Enhanced Antibacterial effect of chitosan film using Montmorillonite/CuO nanocomposite. *International Journal of Biological Macromolecules*, 109, 1219–1231. <https://doi.org/10.1016/j.ijbiomac.2017.11.119>

Nouri, A., Yaraki, M. T., Ghorbanpour, M., Agarwal, S., & Gupta, V. K. (2018b). Enhanced Antibacterial effect of chitosan film using

Montmorillonite/CuO nanocomposite. *International Journal of Biological Macromolecules*, 109, 1219–1231.  
<https://doi.org/10.1016/j.ijbiomac.2017.11.119>

Novoselov, K. S., Geim, A. K., Morozov, S. V., Jiang, D., Zhang, Y., Dubonos, S. V., Grigorieva, I. V., & Firsov, A. A. (2004). Electric field effect in atomically thin carbon films. *Science (New York, N.Y.)*, 306(5696), 666–669. <https://doi.org/10.1126/science.1102896>

Nupearachchi, C. N., Mahatantila, K., & Vithanage, M. (2017). Application of graphene for decontamination of water; Implications for sorptive removal. *Groundwater for Sustainable Development*, 5, 206–215.  
<https://doi.org/10.1016/j.gsd.2017.06.006>

Oberlintner, A., Bajić, M., Kalčíková, G., Likozar, B., & Novak, U. (2021). Biodegradability study of active chitosan biopolymer films enriched with Quercus polyphenol extract in different soil types. *Environmental Technology & Innovation*, 21, 101318.  
<https://doi.org/10.1016/j.eti.2020.101318>

Oh, S. J., Cook, D. C., & Townsend, H. E. (1998). Characterization of Iron Oxides Commonly Formed as Corrosion Products on Steel. *Hyperfine Interactions*, 112(1), 59–66. <https://doi.org/10.1023/A:1011076308501>

Onu, C. E., Nwabanne, J. T., Ohale, P. E., & Asadu, C. O. (2021a). Comparative analysis of RSM, ANN and ANFIS and the mechanistic modeling in eriochrome black-T dye adsorption using modified clay. *South African Journal of Chemical Engineering*, 36, 24–42.  
<https://doi.org/10.1016/j.sajce.2020.12.003>

Onu, C. E., Nwabanne, J. T., Ohale, P. E., & Asadu, C. O. (2021b). Comparative analysis of RSM, ANN and ANFIS and the mechanistic modeling in eriochrome black-T dye adsorption using modified clay. *South African Journal of Chemical Engineering*, 36, 24–42.  
<https://doi.org/10.1016/j.sajce.2020.12.003>

Osaili, T. M., Albiss, B. A., Al-Nabulsi, A. A., Alromi, R. F., Olaimat, A., Al-Holy, M., Savvaidis, I., & Holley, R. (2019). Effects of metal oxide nanoparticles with plant extract on viability of foodborne pathogens. *Journal of Food Safety*, 39(5), e12681.  
<https://doi.org/10.1111/jfs.12681>

Oun, A. A., & Rhim, J.-W. (2017). Carrageenan-based hydrogels and films: Effect of ZnO and CuO nanoparticles on the physical, mechanical, and antimicrobial properties. *Food Hydrocolloids*, 67, 45–53.  
<https://doi.org/10.1016/j.foodhyd.2016.12.040>

Özdemir, K. S., & Gökmen, V. (2019). Effect of Chitosan-Ascorbic Acid Coatings on the Refrigerated Storage Stability of Fresh-Cut Apples. *Coatings*, 9(8), 503. <https://doi.org/10.3390/coatings9080503>

Ozdokur, K. V., Demir, B., Atman, E., Tatli, A. Y., Yilmaz, B., Demirkol, D. O., Kocak, S., Timur, S., & Ertas, F. N. (2016). A novel ethanol biosensor on pulsed deposited MnO<sub>x</sub>-MoO<sub>x</sub> electrode decorated with Pt nanoparticles. *Sensors and Actuators B: Chemical*, 237, 291–297. <https://doi.org/10.1016/j.snb.2016.06.100>

Padmavathi, A. R., P., S. M., Das, A., Priya, A., Sushmitha, T. J., Pandian, S. K., & Toleti, S. R. (2020). Impediment to growth and yeast-to-hyphae transition in *Candida albicans* by copper oxide nanoparticles. *Biofouling*, 36(1), 56–72. <https://doi.org/10.1080/08927014.2020.1715371>

Pal, K., Bharti, D., Sarkar, P., Anis, A., Kim, D., Chałas, R., Maksymiuk, P., Stachurski, P., & Jarzębski, M. (2021). Selected Applications of Chitosan Composites. *International Journal of Molecular Sciences*, 22(20), 10968. <https://doi.org/10.3390/ijms222010968>

Panda, H., Tiadi, N., Mohanty, M., & Mohanty, C. R. (2017). Studies on adsorption behavior of an industrial waste for removal of chromium from aqueous solution. *South African Journal of Chemical Engineering*, 23, 132–138. <https://doi.org/10.1016/j.sajce.2017.05.002>

Parkar, J., & Rakesh, M. (2014). Leaching of elements from packaging material into canned foods marketed in India. *Food Control*, 40, 177–184. <https://doi.org/10.1016/j.foodcont.2013.11.042>

Pastor, C., Sánchez-González, L., Chiralt, A., Cháfer, M., & González-Martínez, C. (2013). Physical and antioxidant properties of chitosan and methylcellulose based films containing resveratrol. *Food Hydrocolloids*, 30(1), 272–280. <https://doi.org/10.1016/j.foodhyd.2012.05.026>

Perdones, Á., Vargas, M., Atarés, L., & Chiralt, A. (2014). Physical, antioxidant and antimicrobial properties of chitosan–cinnamon leaf oil films as affected by oleic acid. *Food Hydrocolloids*, 36, 256–264. <https://doi.org/10.1016/j.foodhyd.2013.10.003>

Petcharoen, K., & Sirivat, A. (2012). Synthesis and characterization of magnetite nanoparticles via the chemical co-precipitation method. *Materials Science and Engineering: B*, 177(5), 421–427. <https://doi.org/10.1016/j.mseb.2012.01.003>

Pissuwan, D., Gazzana, C., Mongkolsuk, S., & Cortie, M. B. (2020). Single and multiple detections of foodborne pathogens by gold nanoparticle

assays. *WIREs Nanomedicine and Nanobiotechnology*, 12(1), e1584. <https://doi.org/10.1002/wnan.1584>

Plancque, G., Moulin, V., Toulhoat, P., & Moulin, C. (2003). Europium speciation by time-resolved laser-induced fluorescence. *Analytica Chimica Acta*, 478(1), 11–22. [https://doi.org/10.1016/S0003-2670\(02\)01486-1](https://doi.org/10.1016/S0003-2670(02)01486-1)

Priyadarshi, R., & Rhim, J.-W. (2020). Chitosan-based biodegradable functional films for food packaging applications. *Innovative Food Science & Emerging Technologies*, 62, 102346. <https://doi.org/10.1016/j.ifset.2020.102346>

Pujol Pozo, A. A., Monroy-Guzmán, F., Gómora- Herrera, D. R., Navarrete-Bolaños, J., & Bustos Bustos, E. (2022). Radioactive decontamination of metal surfaces using peelable films made from chitosan gels and chitosan/magnetite nanoparticle composites. *Progress in Nuclear Energy*, 144. <https://doi.org/10.1016/j.pnucene.2021.104088>

Qiu, J. D., Wang, G. C., Liang, R. P., Xia, X. H., & Yu, H. W. (2011). Controllable deposition of platinum nanoparticles on graphene as an electrocatalyst for direct methanol fuel cells. *Journal of Physical Chemistry C*, 115(31). <https://doi.org/10.1021/jp200580u>

Raffi, M., Mehrwan, S., Bhatti, T. M., Akhter, J. I., Hameed, A., Yawar, W., & Ul Hasan, M. M. (2010). Investigations into the antibacterial behavior of copper nanoparticles against *Escherichia coli*. *Annals of Microbiology*, 60(1), 75–80. <https://doi.org/10.1007/s13213-010-0015-6>

Rao, D., Sheng, Q., & Zheng, J. (2016). Preparation of flower-like Pt nanoparticles decorated chitosan-grafted graphene oxide and its electrocatalysis of hydrazine. *Sensors and Actuators, B: Chemical*, 236. <https://doi.org/10.1016/j.snb.2016.05.160>

Ren, G., Hu, D., Cheng, E. W. C., Vargas-Reus, M. A., Reip, P., & Allaker, R. P. (2009). Characterisation of copper oxide nanoparticles for antimicrobial applications. *International Journal of Antimicrobial Agents*, 33(6). <https://doi.org/10.1016/j.ijantimicag.2008.12.004>

Romanchuk, A. Y., Slesarev, A. S., Kalmykov, S. N., Kosynkin, D. V., & Tour, J. M. (2013). Graphene oxide for effective radionuclide removal. *Physical Chemistry Chemical Physics*, 15(7), 2321–2327. <https://doi.org/10.1039/C2CP44593J>

Rong, L. Q., Yang, C., Qian, Q. Y., & Xia, X. H. (2007). Study of the nonenzymatic glucose sensor based on highly dispersed Pt nanoparticles supported on carbon nanotubes. *Talanta*, 72(2). <https://doi.org/10.1016/j.talanta.2006.12.037>

Rossa, V., Monteiro Ferreira, L. E., da Costa Vasconcelos, S., Tai Shimabukuro, E. T., da Costa Madriaga, V., Carvalho, A. P., Castellã Pergher, S. B., de Carvalho da Silva, F., Ferreira, V. F., Conte Junior, C. A., & de Melo Lima, T. (2022). Nanocomposites based on the graphene family for food packaging: historical perspective, preparation methods, and properties. *RSC Adv.*, 12(22), 14084–14111.  
<https://doi.org/10.1039/D2RA00912A>

Roy, S., & Rhim, J.-W. (2019). Melanin-Mediated Synthesis of Copper Oxide Nanoparticles and Preparation of Functional Agar/CuO NP Nanocomposite Films. *Journal of Nanomaterials*, 2019, 1–10.  
<https://doi.org/10.1155/2019/2840517>

Sabzevari, M., Cree, D. E., & Wilson, L. D. (2018). Graphene Oxide–Chitosan Composite Material for Treatment of a Model Dye Effluent. *ACS Omega*, 3(10), 13045–13054.  
<https://doi.org/10.1021/acsomega.8b01871>

Saharan, V., Sharma, G., Yadav, M., Choudhary, M. K., Sharma, S. S., Pal, A., Raliya, R., & Biswas, P. (2015). Synthesis and in vitro antifungal efficacy of Cu–chitosan nanoparticles against pathogenic fungi of tomato. *International Journal of Biological Macromolecules*, 75, 346–353. <https://doi.org/10.1016/j.ijbiomac.2015.01.027>

Sahoo, S., Subudhi, B., & Panda, G. (2020). Torque and pitch angle control of a wind turbine using multiple adaptive neuro-fuzzy control. *Wind Engineering*, 44(2), 125–141.  
<https://doi.org/10.1177/0309524X19849825>

Sánchez-González, L., Cháfer, M., Chiralt, A., & González-Martínez, C. (2010). Physical properties of edible chitosan films containing bergamot essential oil and their inhibitory action on *Penicillium italicum*. *Carbohydrate Polymers*, 82(2), 277–283.  
<https://doi.org/10.1016/j.carbpol.2010.04.047>

Santos-Cruz, D., Mayén-Hernández, S. A., de Moure-Flores, F., Campos-Álvarez, J., Pal, M., & Santos-Cruz, J. (2017). CuOX thin films by direct oxidation of Cu films deposited by physical vapour deposition. *Results in Physics*, 7. <https://doi.org/10.1016/j.rinp.2017.10.022>

Shamhari, N. M., Wee, B. S., Chin, S. F., & Kok, K. Y. (2018). Synthesis and Characterization of Zinc Oxide Nanoparticles with Small Particle Size Distribution. *Acta Chimica Slovenica*, 65(3), 578–585.  
<https://doi.org/10.17344/acsi.2018.4213>

Shariatinia, Z., & Fazli, M. (2015). Mechanical properties and antibacterial activities of novel nanobiocomposite films of chitosan and starch. *Food*

*Hydrocolloids*, 46, 112–124.  
<https://doi.org/10.1016/j.foodhyd.2014.12.026>

Sharififard, H., Zokaei Ashtiani, F., & Soleimani, M. (2013). Adsorption of palladium and platinum from aqueous solutions by chitosan and activated carbon coated with chitosan. *Asia-Pacific Journal of Chemical Engineering*, 8(3). <https://doi.org/10.1002/apj.1671>

Sharma, P., Khairnar, V., Madunić, I. V., Singh, Y., Pandya, A., Salker, M. S., Koepsell, H., Sabolić, I., Lang, F., Lang, P. A., & Lang, K. S. (2017). SGLT1 Deficiency Turns Listeria Infection into a Lethal Disease in Mice. *Cellular Physiology and Biochemistry*, 42(4), 1358–1365. <https://doi.org/10.1159/000479197>

Shen, R., Wang, H., Wu, K., Gao, J., & Li, J. (2021). Characterization and antimicrobial properties of ferulic acid grafted self-assembled bacterial cellulose-chitosan membranes. *Journal of Applied Polymer Science*, 138(33), 50824. <https://doi.org/10.1002/app.50824>

Siddiqui, S. A., Bahmid, N. A., Salman, S. H. M., Nawaz, A., Walayat, N., Shekhawat, G. K., Gvozdenko, A. A., Blinov, A. V., & Nagdalian, A. A. (2023). Chapter Eight - Migration of microplastics from plastic packaging into foods and its potential threats on human health. In F. Özogul (Ed.), *Advances in Food and Nutrition Research* (Vol. 103, pp. 313–359). Academic Press. <https://doi.org/10.1016/bs.afnr.2022.07.002>

Sinha, T., Adhikari, P. P., & Bhandari, V. M. (2022). Sustainable Fabrication of Copper Nanoparticles: A Potent and Affordable Candidate for Water Treatment, Water Disinfection, Antioxidant Activity and Theranostic Agent. *ChemistrySelect*, 7(15), e202103552. <https://doi.org/10.1002/slct.202103552>

Siripatrawan, U., & Harte, B. R. (2010). Physical properties and antioxidant activity of an active film from chitosan incorporated with green tea extract. *Food Hydrocolloids*, 24(8), 770–775.  
<https://doi.org/10.1016/j.foodhyd.2010.04.003>

Song, H., Li, B., Lin, Q.-B., Wu, H.-J., & Chen, Y. (2011). Migration of silver from nanosilver–polyethylene composite packaging into food simulants. *Food Additives & Contaminants: Part A*, 1–5.  
<https://doi.org/10.1080/19440049.2011.603705>

Souza, P. R., Dotto, G. L., & Salau, N. P. G. (2018a). Artificial neural network (ANN) and adaptive neuro-fuzzy interference system (ANFIS) modelling for nickel adsorption onto agro-wastes and commercial activated carbon. *Journal of Environmental Chemical Engineering*, 6(6), 7152–7160. <https://doi.org/10.1016/j.jece.2018.11.013>

Souza, P. R., Dotto, G. L., & Salau, N. P. G. (2018b). Artificial neural network (ANN) and adaptive neuro-fuzzy interference system (ANFIS) modelling for nickel adsorption onto agro-wastes and commercial activated carbon. *Journal of Environmental Chemical Engineering*, 6(6), 7152–7160. <https://doi.org/10.1016/j.jece.2018.11.013>

Sun, L., Sun, J., Chen, L., Niu, P., Yang, X., & Guo, Y. (2017). Preparation and characterization of chitosan film incorporated with thinned young apple polyphenols as an active packaging material. *Carbohydrate Polymers*, 163, 81–91. <https://doi.org/10.1016/j.carbpol.2017.01.016>

Sun, Y., Wang, Q., Chen, C., Tan, X., & Wang, X. (2012). Interaction between Eu(III) and Graphene Oxide Nanosheets Investigated by Batch and Extended X-ray Absorption Fine Structure Spectroscopy and by Modeling Techniques. *Environmental Science & Technology*, 46(11), 6020–6027. <https://doi.org/10.1021/es300720f>

Suppakul, P., Miltz, J., Sonneveld, K., & Bigger, S. W. (2003). Active Packaging Technologies with an Emphasis on Antimicrobial Packaging and its Applications. *J Food Science*, 68(2), 408–420. <https://doi.org/10.1111/j.1365-2621.2003.tb05687.x>

Susilowati, E., Maryani, & Ashadi. (2019). Green synthesis of silver-chitosan nanocomposite and their application as antibacterial material. *Journal of Physics: Conference Series*, 1153, 12135. <https://doi.org/10.1088/1742-6596/1153/1/012135>

Sutradhar, P., Saha, M., & Maiti, D. (2014). Microwave synthesis of copper oxide nanoparticles using tea leaf and coffee powder extracts and its antibacterial activity. *Journal of Nanostructure in Chemistry*, 4(1), 86. <https://doi.org/10.1007/s40097-014-0086-1>

Tabassum, Z., Girdhar, M., Kumar, A., Malik, T., & Mohan, A. (2023). ZnO Nanoparticles-Reinforced Chitosan–Xanthan Gum Blend Novel Film with Enhanced Properties and Degradability for Application in Food Packaging. *ACS Omega*, 8(34), 31318–31332. <https://doi.org/10.1021/acsomega.3c03763>

Tang, N., Liang, J., Niu, C., Wang, H., Luo, Y., Xing, W., Ye, S., Liang, C., Guo, H., Guo, J., Zhang, Y., & Zeng, G. (2020). Amidoxime-based materials for uranium recovery and removal. *J. Mater. Chem. A*, 8(16), 7588–7625. <https://doi.org/10.1039/C9TA14082D>

Taylor, R. B., & Sapozhnikova, Y. (2022). Assessing Chemical Migration from Plastic Food Packaging into Food Simulant by Gas and Liquid Chromatography with High-Resolution Mass Spectrometry. *J. Agric. Food Chem.*, 70(16), 4805–4816. <https://doi.org/10.1021/acs.jafc.2c00736>

Terzioglu, P., Altin, Y., Kalemtas, A., & Celik Bedeloglu, A. (2020). Graphene oxide and zinc oxide decorated chitosan nanocomposite biofilms for packaging applications. *Journal of Polymer Engineering*, 40(2), 152–157. <https://doi.org/10.1515/polyeng-2019-0240>

Tiimob, B. J., Mwinyelle, G., Abdela, W., Samuel, T., Jeelani, S., & Rangari, V. K. (2017). Nanoengineered Eggshell–Silver Tailored Copolyester Polymer Blend Film with Antimicrobial Properties. *Journal of Agricultural and Food Chemistry*, 65(9), 1967–1976. <https://doi.org/10.1021/acs.jafc.7b00133>

Tripathi, S., Mehrotra, G. K., & Dutta, P. K. (2009). Physicochemical and bioactivity of cross-linked chitosan–PVA film for food packaging applications. *International Journal of Biological Macromolecules*, 45(4), 372–376. <https://doi.org/10.1016/j.ijbiomac.2009.07.006>

Tuutijärvi, T., Lu, J., Sillanpää, M., & Chen, G. (2009). As(V) adsorption on maghemite nanoparticles. *Journal of Hazardous Materials*, 166(2), 1415–1420. <https://doi.org/10.1016/j.jhazmat.2008.12.069>

Ullah, R., Khan, S. A., Aladresi, A. A. M., Alharbi, S. A., & Chinnathambi, A. (2020). Ovalbumin-mediated synthesis and simultaneous functionalization of graphene with increased protein stability. *Green Chemistry Letters and Reviews*, 13(1), 60–67. <https://doi.org/10.1080/17518253.2020.1725150>

van Lierop, J., & Ryan, D. H. (2001). Mössbauer Spectra of Single-Domain Fine Particle Systems Described Using a Multiple-Level Relaxation Model for Superparamagnets. *Physical Review B*, 63(6), 64406. <https://doi.org/10.1103/PhysRevB.63.064406>

Vasi, S., Ceccio, G., Cannavò, A., Pleskunov, P., & Vacík, J. (2022). Study of Wettability of Polyethylene Membranes for Food Packaging. *Sustainability*, 14(10), 5863. <https://doi.org/10.3390/su14105863>

Vasile, C., Pamfil, D., Râpă, M., Darie-Niță, R. N., Mitelut, A. C., Popa, E. E., Popescu, P. A., Draghici, M. C., & Popa, M. E. (2018). Study of the soil burial degradation of some PLA/CS biocomposites. *Composites Part B: Engineering*, 142, 251–262. <https://doi.org/10.1016/j.compositesb.2018.01.026>

Vidic, J., Stankic, S., Haque, F., Ciric, D., Le Goffic, R., Vidy, A., Jupille, J., & Delmas, B. (2013). Selective antibacterial effects of mixed ZnMgO nanoparticles. *Journal of Nanoparticle Research*, 15(5), 1595. <https://doi.org/10.1007/s11051-013-1595-4>

Vishnuvarthan, M., & Rajeswari, N. (2019). Food packaging: pectin–laponite–Ag nanoparticle bionanocomposite coated on polypropylene shows low O<sub>2</sub> transmission, low Ag migration and high antimicrobial

activity. *Environmental Chemistry Letters*, 17(1), 439–445.  
<https://doi.org/10.1007/s10311-018-0770-3>

Vo, T. S., Vo, T. T. B. C., Suk, J. W., & Kim, K. (2020). Recycling performance of graphene oxide-chitosan hybrid hydrogels for removal of cationic and anionic dyes. *Nano Convergence*, 7(1), 4.  
<https://doi.org/10.1186/s40580-019-0215-0>

Wang, H., Qian, J., & Ding, F. (2018). Emerging Chitosan-Based Films for Food Packaging Applications. *Journal of Agricultural and Food Chemistry*, 66(2), 395–413. <https://doi.org/10.1021/acs.jafc.7b04528>

Wang, L., Liu, F., Jiang, Y., Chai, Z., Li, P., Cheng, Y., Jing, H., & Leng, X. (2011). Synergistic Antimicrobial Activities of Natural Essential Oils with Chitosan Films. *Journal of Agricultural and Food Chemistry*, 59(23), 12411–12419. <https://doi.org/10.1021/jf203165k>

Wang, M.-Q., Du, X.-Y., Liu, Li-Y., Sun, Q., & Jiang, X.-C. (2008). DNA Biosensor Prepared by Electrodeposited Pt-nanoparticles for the Detection of Specific Deoxyribonucleic Acid Sequence in Genetically Modified Soybean. *Chinese Journal of Analytical Chemistry*, 36(7), 890–894. [https://doi.org/10.1016/S1872-2040\(08\)60048-1](https://doi.org/10.1016/S1872-2040(08)60048-1)

Wang, X., Bai, H., Yao, Z., Liu, A., & Shi, G. (2010). Electrically conductive and mechanically strong biomimetic chitosan/reduced graphene oxide composite films. *Journal of Materials Chemistry*, 20(41), 9032. <https://doi.org/10.1039/c0jm01852j>

Wu, B., Huang, R., Sahu, M., Feng, X., Biswas, P., & Tang, Y. J. (2010). Bacterial responses to Cu-doped TiO<sub>2</sub> nanoparticles. *Science of The Total Environment*, 408(7), 1755–1758.  
<https://doi.org/10.1016/j.scitotenv.2009.11.004>

Wu, G., Liu, Y., Zheng, Q., Yu, Z., & Luo, F. (2020). Ultrahigh uranium extraction performance of COFs/SPES mixed matrix membranes at acidic medium. *Journal of Solid State Chemistry*, 288, 121364.  
<https://doi.org/10.1016/j.jssc.2020.121364>

Wu, X., Yang, Q., Xu, D., Zhong, Y., Luo, K., Li, X., Chen, H., & Zeng, G. (2013). Simultaneous Adsorption/Reduction of Bromate by Nanoscale Zerovalent Iron Supported on Modified Activated Carbon. *Industrial & Engineering Chemistry Research*, 52(35), 12574–12581.  
<https://doi.org/10.1021/ie4009524>

Xie, Y., Chen, C., Ren, X., Wang, X., Wang, H., & Wang, X. (2019). Emerging natural and tailored materials for uranium-contaminated water treatment and environmental remediation. *Progress in Materials Science*, 103, 180–234. <https://doi.org/10.1016/j.pmatsci.2019.01.005>

Xiu, T., Liu, Z., Wang, Y., Wu, P., Du, Y., & Cai, Z. (2019). Thorium adsorption on graphene oxide nanoribbons/manganese dioxide composite material. *Journal of Radioanalytical and Nuclear Chemistry*, 319(3), 1059–1067. <https://doi.org/10.1007/s10967-019-06417-9>

Xu, B., Zhu, Y., Liu, H., Jin, Z., & Chen, T. (2016a). The kinetic and thermodynamic adsorption of Eu(III) on synthetic maghemite. *Journal of Molecular Liquids*, 221, 171–178. <https://doi.org/10.1016/j.molliq.2016.05.055>

Xu, B., Zhu, Y., Liu, H., Jin, Z., & Chen, T. (2016b). The kinetic and thermodynamic adsorption of Eu(III) on synthetic maghemite. *Journal of Molecular Liquids*, 221, 171–178. <https://doi.org/10.1016/j.molliq.2016.05.055>

Xu, J., Liu, K., Chang, W., Chiou, B.-S., Chen, M., & Liu, F. (2022). Regulating the Physicochemical Properties of Chitosan Films through Concentration and Neutralization. *Foods*, 11(11), 1657. <https://doi.org/10.3390/foods11111657>

Yadav, B., Sen, Singh, R., Vishwakarma, A. K., & Kumar, N. (2020a). Facile Synthesis of Substantially Magnetic Hollow Nanospheres of Maghemite ( $\gamma$ -Fe<sub>2</sub>O<sub>3</sub>) Originated from Magnetite (Fe<sub>3</sub>O<sub>4</sub>) via Solvothermal Method. *Journal of Superconductivity and Novel Magnetism*, 33(7), 2199–2208. <https://doi.org/10.1007/s10948-020-05481-7>

Yadav, B., Sen, Singh, R., Vishwakarma, A. K., & Kumar, N. (2020b). Facile Synthesis of Substantially Magnetic Hollow Nanospheres of Maghemite ( $\gamma$ -Fe<sub>2</sub>O<sub>3</sub>) Originated from Magnetite (Fe<sub>3</sub>O<sub>4</sub>) via Solvothermal Method. *Journal of Superconductivity and Novel Magnetism*, 33(7), 2199–2208. <https://doi.org/10.1007/s10948-020-05481-7>

Yan, J., Li, M., Wang, H., Lian, X., Fan, Y., Xie, Z., Niu, B., & Li, W. (2021a). Preparation and property studies of chitosan-PVA biodegradable antibacterial multilayer films doped with Cu<sub>2</sub>O and nano-chitosan composites. *Food Control*, 126, 108049. <https://doi.org/10.1016/j.foodcont.2021.108049>

Yan, J., Li, M., Wang, H., Lian, X., Fan, Y., Xie, Z., Niu, B., & Li, W. (2021b). Preparation and property studies of chitosan-PVA biodegradable antibacterial multilayer films doped with Cu<sub>2</sub>O and nano-chitosan composites. *Food Control*, 126, 108049. <https://doi.org/10.1016/j.foodcont.2021.108049>

Yang, X., Tu, Y., Li, L., Shang, S., & Tao, X. (2010). Well-Dispersed Chitosan/Graphene Oxide Nanocomposites. *ACS Applied Materials & Interfaces*, 2(6), 1707–1713. <https://doi.org/10.1021/am100222m>

Yang, Z., Ma, C., Wang, W., Zhang, M., Hao, X., & Chen, S. (2019). Fabrication of Cu<sub>2</sub>O-Ag nanocomposites with enhanced durability and bactericidal activity. *Journal of Colloid and Interface Science*, 557, 156–167. <https://doi.org/10.1016/j.jcis.2019.09.015>

Yilmaz Dogan, H., Altin, Y., & Bedeloglu, A. Ç. (2022). Fabrication and properties of graphene oxide and reduced graphene oxide reinforced Poly(Vinyl alcohol) nanocomposite films for packaging applications. *Polymers and Polymer Composites*, 30, 09673911221113328. <https://doi.org/10.1177/09673911221113328>

Yin, K., Zhang, Y.-Y., Zhou, Y., Sun, L., Chisholm, M. F., Pantelides, S. T., & Zhou, W. (2016). Unsupported single-atom-thick copper oxide monolayers. *2D Materials*, 4(1), 11001. <https://doi.org/10.1088/2053-1583/4/1/011001>

Yin, P. T., Shah, S., Chhowalla, M., & Lee, K. B. (2015). Design, synthesis, and characterization of graphene-nanoparticle hybrid materials for bioapplications. In *Chemical Reviews* (Vol. 115, Issue 7). <https://doi.org/10.1021/cr500537t>

Yong, H., Liu, Y., Yun, D., Zong, S., Jin, C., & Liu, J. (2021). Chitosan films functionalized with different hydroxycinnamic acids: Preparation, characterization and application for pork preservation. *Foods*, 10(3). <https://doi.org/10.3390/foods10030536>

Young, W., Hwang, K., McDonald, S., & Oates, C. J. (2010). Sustainable consumption: green consumer behaviour when purchasing products. *Sustainable Development*, 18(1), 20–31. <https://doi.org/10.1002/sd.394>

Yousefi, A., Babaei, A., & Delavar, M. (2018). Application of modified screen-printed carbon electrode with MWCNTs-Pt-doped CdS nanocomposite as a sensitive sensor for determination of natamycin in yoghurt drink and cheese. *Journal of Electroanalytical Chemistry*, 822, 1–9. <https://doi.org/10.1016/j.jelechem.2018.05.008>

Yuan, G., Lv, H., Yang, B., Chen, X., & Sun, H. (2015). Physical Properties, Antioxidant and Antimicrobial Activity of Chitosan Films Containing Carvacrol and Pomegranate Peel Extract. *Molecules*, 20(6), 11034–11045. <https://doi.org/10.3390/molecules200611034>

Zawadzka, K., Kisielewska, A., Piwoński, I., Kądzioła, K., Felczak, A., Różalska, S., Wrońska, N., & Lisowska, K. (2016). Mechanisms of antibacterial activity and stability of silver nanoparticles grown on

magnetron sputtered TiO<sub>2</sub> coatings. *Bulletin of Materials Science*, 39(1), 57–68. <https://doi.org/10.1007/s12034-015-1137-z>

Zhang, B., Hu, R., Sun, D., Wu, T., & Li, Y. (2018). Fabrication of chitosan/magnetite-graphene oxide composites as a novel bioadsorbent for adsorption and detoxification of Cr(VI) from aqueous solution. *Sci Rep*, 8(1), 15397. <https://doi.org/10.1038/s41598-018-33925-7>

Zhang, H., Zhao, F.-J., Sun, B., Davison, W., & McGrath, S. P. (2001). A New Method to Measure Effective Soil Solution Concentration Predicts Copper Availability to Plants. *Environ. Sci. Technol.*, 35(12), 2602–2607. <https://doi.org/10.1021/es000268q>

Zhang, Q., Zhuang, S., & Wang, J. (2020). Biosorptive removal of cobalt(II) from aqueous solutions using magnetic cyanoethyl chitosan beads. *Journal of Environmental Chemical Engineering*, 8(6), 104531. <https://doi.org/10.1016/j.jece.2020.104531>

Zhang, W., Roy, S., & Rhim, J.-W. (2023). Copper-based nanoparticles for biopolymer-based functional films in food packaging applications. *Comprehensive Reviews in Food Science and Food Safety*, 22(3), 1933–1952. <https://doi.org/10.1111/1541-4337.13136>

Zhang, X., He, M., Zhan, Y., Yang, W., & Wu, K. (2022). Microstructure, Mechanical and Electrical Properties of Hybrid Copper Matrix Composites with Fe Microspheres and rGO Nanosheets. *Molecules*, 27(19), 6518. <https://doi.org/10.3390/molecules27196518>

Zhao, G., Ren, X., Gao, X., Tan, X., Li, J., Chen, C., Huang, Y., & Wang, X. (2011). Removal of Pb(II) ions from aqueous solutions on few-layered graphene oxide nanosheets. *Dalton Transactions (Cambridge, England: 2003)*, 40(41), 10945–10952. <https://doi.org/10.1039/c1dt11005e>

Zhao, W., Ren, B., Hursthouse, A., & Wang, Z. (2021). Facile synthesis of nanosheet-assembled  $\gamma$ -Fe<sub>2</sub>O<sub>3</sub> magnetic microspheres and enhanced Sb(III) removal. *Environ Sci Pollut Res*, 28(16), 19822–19837. <https://doi.org/10.1007/s11356-020-11727-7>

Zhong, T., Oporto, G. S., & Jaczynski, J. (2017). Antimicrobial food packaging with cellulose-copper nanoparticles embedded in thermoplastic resins. In *Food Preservation* (pp. 671–702). Elsevier. <https://doi.org/10.1016/B978-0-12-804303-5.00019-5>

Zhu, L., Pearson, D. W., Benoit, S. L., Xie, J., Pant, J., Yang, Y., Mondal, A., Handa, H., Howe, J. Y., Hung, Y.-C., Vidal, J. E., Maier, R. J., & Zhao, Y. (2020). Highly Efficient Antimicrobial Activity of Cu<sub>x</sub>FeyO<sub>z</sub> Nanoparticles against Important Human Pathogens. *Nanomaterials*, 10(11), 2294. <https://doi.org/10.3390/nano10112294>

Zhu, Y., Murali, S., Cai, W., Li, X., Suk, J. W., Potts, J. R., & Ruoff, R. S. (2010). Graphene and Graphene Oxide: Synthesis, Properties, and Applications. *Advanced Materials*, 22(35), 3906–3924.  
<https://doi.org/10.1002/adma.201001068>

Zhuang, S., & Wang, J. (2019). Removal of cobalt ion from aqueous solution using magnetic graphene oxide/chitosan composite. *Environmental Progress & Sustainable Energy*, 38(s1).  
<https://doi.org/10.1002/ep.12912>

Zhuang, S., Zhu, K., Hu, J., & Wang, J. (2022). Selective and effective adsorption of cesium ions by metal hexacyanoferrates (MHCF, M = Cu, Co, Ni) modified chitosan fibrous biosorbent. *Science of The Total Environment*, 835, 155575.  
<https://doi.org/10.1016/j.scitotenv.2022.155575>

Zimoch-Korzycka, A., & Jarmoluk, A. (2015). The use of chitosan, lysozyme, and the nano-silver as antimicrobial ingredients of edible protective hydrosols applied into the surface of meat. *Journal of Food Science and Technology*, 52(9), 5996–6002.  
<https://doi.org/10.1007/s13197-014-1645-7>

Zuo, P.-P., Feng, H.-F., Xu, Z.-Z., Zhang, L.-F., Zhang, Y.-L., Xia, W., & Zhang, W.-Q. (2013). Fabrication of biocompatible and mechanically reinforced graphene oxide-chitosan nanocomposite films. *Chemistry Central Journal*, 7(1), 39. <https://doi.org/10.1186/1752-153X-7-39>

CURRICULUM VITAE  
Edith Flora Joel  
1995-04-25, Vilnius, Lithuania

## EDUCATION

Centre for Physical Sciences and Technology	2019–2023
<i>PhD studies</i>	
Amrita Medical College, India	2016-2018
<i>Master of nanomedical sciences</i>	
Noorul Islam University, India	2012-2016
<i>Bachelor of Biomedical Engineering</i>	
<b>PROFESSIONAL CAREER</b>	
Sostie Inc., Lithuania	2022-Present
<i>Strategy Consultant</i>	
Syno International, Lithuania	2021-2022
<i>Client Operation Specialist</i>	

## ACKNOWLEDGEMENTS

I would like to express my sincere gratitude to Dr. Galina Lujanienė for her invaluable expertise, guidance, patience and unwavering support during my doctoral research. I am deeply indebted to Dr. Sergej Šemčuk for his expert advice and guidance which helped me a lot in my research. My special thanks go to Dr. Raman Novikau for his crucial contributions to the synthesis and characterization of graphene oxide-maghemite composites and for being a great colleague.

I would like to express my appreciation to Michael Hanzl for his mentorship. Finally, I would like to sincerely thank my husband, my parents and in-laws, and my sisters for their endless patience, understanding, and encouragement throughout this endeavor.

FOR NOTES

FOR NOTES

FOR NOTES

Vilnius University Press  
9 Saulėtekio Ave., Building III, LT-10222 Vilnius Email:  
[info@leidykla.vu.lt](mailto:info@leidykla.vu.lt), [www.leidykla.vu.lt](http://www.leidykla.vu.lt)  
[bookshop.vu.lt](http://bookshop.vu.lt), [journals.vu.lt](http://journals.vu.lt)  
Print run copies 22